This is to certify that the

dissertation entitled

VISUALIZATION OF TWO-PHASE FLUID DISTRIBUTIONS
USING LASER-INDUCED EXCIPLEX FLUORESCENCE

presented by

JongUk Kim

has been accepted towards fulfillment
of the requirements for

Ph.D. degree in Physics

Major professor

Date August 21, 1997

VISUALIZATION OF TWO-PHASE FLUID DISTRIBUTIONS USING LASER-INDUCED EXCIPLEX FLUORESCENCE

By

JongUk Kim

A DISSERTATION

Submitted to
Michigan State University
in partial fulfillment of the requirements
for the degree of

DOCTOR OF PHILOSOPHY

Department of Physics

1997

ABSTRACT

VISUALIZATION OF TWO-PHASE FLUID DISTRIBUTIONS USING LASER-INDUCED EXCIPLEX FLUORESCENCE

By

JongUk Kim

Experimental optical methods have been developed for the purpose of visualizing two-phase fluid distributions. Laser-induced exciplex (excited state complex) fluorescence has been used to generate two-dimensional images of dispersed liquid and vapor phases with spectrally well resolved two-color emissions. In this method, the vapor phase is tagged by the monomer fluorescence while the liquid phase is tracked by the exciplex fluorescence. For the purpose of observing the highly turbulent dynamic behavior of injected liquid through a small orifice, exciplex visualization provides a non-intrusive diagnostic with good spectral and spatial resolution. A new exciplex visualization system consisting of DMA (N,N-dimethylaniline) and 1,4,6-TMN (trimethylnaphthalene) in an isooctane (2,2,4-trimethylpentane) solvent was developed. Among the many formulations tested, a 5%DMA•5%1,4,6-TMN exciplex system, in 90% isooctane solvent, showed outstanding optical characteristics. The kinetics of exciplex formation and decay have been examined as a function of temperature and pressure in detail and related to the photophysics of the system. The direct calibration of the fluorescence intensity as a function of the fluorescing dopant concentrations then permitted the determination of quantitative concentration maps of liquid and vapor phases in the flow-field. The exciplex visualization methods developed have been applied to examine a liquid-vapor spray which evolves rapidly in time and space. The results have a direct bearing on the fuel injection process in the direct-injection spark-ignition engine and will lead to improved understanding of engine efficiency and the formation of pollutants.

To my parents & my wife
for
their encouragement, faith and support throughout my difficult days.

ACKNOWLEDGMENTS

Firstly, I would like to thank my advisors, Professor Brage Golding and Professor Harold Schock, for their inspiring guidance, countless patience, and generous support. Their suggestions and insights have greatly enriched this research.

I would like to thank Dr. Nocera for his valuable suggestions. He greatly helped me to understand the basis of Chemistry in my research. I would like to also thank to my guidance committee members, Dr. Mahanti, Dr. Birge, and Dr. Koochesfahani for their helpful suggestions. Drs. Giles Brereton and Keunchul Lee for their generous effort in listening to my questions and providing me with enriched materials during this research. Thanks goes to Jon Darrow for his help in designing and building the test engine assembly and countless hours in the night for taking data. A special thanks goes to Tom Stuecken for his encouragement in this research. "Dr. Kim" or "Professor Kim" - his joke held a great power whenever I had hard times; My friend, Sangil Hyun, for his friendship especially during hard times; and my lab friends, Lowell McCann, Amy Engebretson, Wenhao Wu, Mark Novak, Eric Bertrand, Larry Dalimonte, Mikhail Ejakov, and Hans Hascher, for their efforts and friendship in helping my research and bearing my unskilled English. A great thanks goes to Bobbie Slider for her time in correcting English and helping me get things done quickly, easily, and with a smile.

My greatest appreciation goes to my parents, especially the late Yun-Bae Kim, my farther, who gave me love and really wanted my success. My brothers and sister, for their support and encouragement throughout this research. My love and special thanks go to my wife Gyongran Han, for her endless love, countless hard times, and great sacrifice. My lovely daughter and son, for their understanding and forgiving of the "busy dad."

I thank the MSU Center for Fundamental Materials Research, the NSF Center for Sensor Materials at MSU, and the Chrysler company for financial support.

TABLE OF CONTENTS

LIST OF TABLES

LIST OF FIGURES

Chapter I. Introduction

1.1. Background and Motivation

Over the last decade or so, the scope of condensed matter physics has expanded into a number of non-traditional areas. As the electronic and structural properties of solids have become well understood, interest has developed, for example, in the behavior of "soft" condensed matter, as well as complex and dissipative dynamical systems. Furthermore, phenomena once considered the domain of chemists, material scientists, and engineers have been probed at different levels of understanding by physicists. For example, the discovery and development of high-T_c superconductivity, carbon buckyballs and tubes, and even crystal growth, have engaged an increasingly multidisciplinary mix of investigators. Concurrent with the increasing breadth of condensed matter research has been an increasing involvement with engineering applications.

In the present research, methods of experimental optical physics have been directed toward addressing a highly complex problem: the dynamical behavior of a polydisperse, two-phase system. When a liquid is injected under high pressure through an orifice, it breaks up into a field of small liquid droplets. The field is not static but, as evaporation occurs, the liquid and vapor rapidly evolve in time and space. The goal of the present research is to develop methods for visualizing and interpreting, using laser-induced fluorescence, the dynamics of the fluid injection and vaporization processes. The methodology draws upon the fields of optical physics, excited-state chemistry, and mechanical engineering. There is an important reason for studying this highly complex system. It is well known that the distribution of fuel vapor and liquid within the combustion chamber of an engine significantly affects its performance and the formation of pollutants.[1] A lean-burn Spark-Ignition (SI) engine is an attractive concept in engine design because it fulfills both environmental and legislative emission requirements by improving engine efficiency and fuel economy.[2] Therefore, it is very important to control the mixture formation for the lean-burn SI engine because the air-fuel mixing process in the combustion chamber has a dominant effect on the subsequent processes of ignition, flame propagation, and pollutant formation under lean (low fuel to air ratio) operating conditions. The aim of the mixture-injected SI engine is to provide better control over the mixing process and to improve stratification of the injected mixture in the combustion chamber. Understanding the mixing process in the combustion chamber is, therefore, one of the key factors in the development of stratified charge engines. Hence, some means of quantitatively analyzing the air-fuel mixture formation is necessary.

As the understanding and governing of these processes is a central necessity in the field of combustion systems, there is a growing demand for practical tools and techniques to actually see the filling of the combustion chamber and the mixing of fuel and air. Therefore, visualization and imaging techniques inside a combustion chamber have been suggested as a diagnostic tool because the technique should be very effective in revealing the distribution of fuel-air mixtures and combustion characteristics. The aim of this study is to develop new, viable diagnostic chemical systems for vapor-liquid phase visualization based on an exciplex (excited state complex) formed between dimethyl- or diethyl-substituted aniline (DMA or DEA) and trimethyl-substituted naphthalenes (TMN) in a fuel, such as isooctane.[3,4] The Laser Induced Exciplex Fluorescence (LIEF) visualization system allows two-dimensional fluorescence images of the liquid and vapor-phase fuel with two different color fluorescence emissions from the vapor and liquid. The calibration of the fluorescence intensity then permits the determination of concentration maps of liquid and vapor phase fuel. Applying this visualization approach to internal combustion engines for understanding of liquid and vapor-phase fuel distributions has yielded detailed information on spray structure, evaporation, and the evolution of the resulting vapor concentration field.

1.2. Application of Exciplex System

The exciplex visualization method is the imaging technique based on laser induced fluorescence (LIF). Currently, most successful applications of exciplex visualization system as an in-situ, noble diagnostic optical technique are typically based on its 2-color fluorescence emissions from the monomer (vapor phase) and exciplex (liquid phase) with properly different emission bands. Fluorescence methods offer the possibility of minimally perturbing, real-time, two-dimensional measurements of liquid and vapor flow motion. The exciplex visualization technique is expected to find application in observing mixture formation in diesel or spark ignition engines with spectrally well-separated fluorescence images obtained from the monomer and exciplex constituents dissolved in the fuel. Additionally, there are three areas of relevance to spray combustion in which exciplex fluorescence have been used as a potential thermometer [5] to measure temperature profiles in isolated droplets,[6-13] sprays,[14] and impinging sprays.[15] Thus, direct measurements of the temperature of the liquid, either in an isolated droplet or in full sprays, provides important information about the thermal transport processes within sprays. Such understanding can lead to more effective design of spray injectors and combustion chambers. Although there is a shortcoming in exciplex visualization systems due to fluorescence quenching in an oxygen environment[16-17] for properly conditioned atmospheres e.g. nitrogen,[18-19] inert gases, or alkanes (which are very ineffective quenchers), its application seems promising.

1.3. Overview of Present Research

This thesis is outlined as follows. After concluding this introductory chapter, the background and theory relevant to this study is reviewed in Chapter II. The development of a new exciplex visualization system which is appropriate for imaging the gasoline-based fuel distribution in a combustion chamber is the primary contribution of this study. Therefore, its photo-physical characteristics, such as steady-state and time-resolved fluorescence spectroscopy, are described in Chapter III. Chapter IV consists of the calibration methods of the monomer and exciplex fluorescence intensity with respect to the concentration of fuel vapor and liquid. A section is devoted to describing the two different procedures between direct- and indirect-pressure measurement (via absorption) in the vapor phase calibration. Chapter V describes vapor phase calibration, particularly in a motored engine condition, and in applying the LIEF technique to direct injection gasoline engines to observe the fuel distributions. Conclusions with recommendations are followed in Chapter VI. Appendices are included to provide detailed information of instrument calibration.

Chapter II. Background and Theory

2.1. Review of flow visualization methods

2.1.1. Fuel spray visualization using fluorescence and other optical methods

Recently, several studies described methods of analyzing the two-dimensional fuel distribution in internal combustion engines.[20-21] There has been considerable progress in the modeling of fuel sprays for internal combustion engines[22] and in the application of experimental techniques to spray measurements inside the engine cylinder.[23-24] Nevertheless, the understanding of the evaporation and mixing processes in engines is still incomplete. Most measurements have concentrated on the structure and development of the liquid spray. Photography has been the principal technique used,[25-33] including such modern developments as endoscopy. [34] In addition, Laser Doppler Velocimetry (LDV)[23,35] and holography [36] have been used. The major limitation of most photographic methods used in engine studies is that they give space integrated, instead of spatially resolved information. An alternative approach which is capable of yielding 3-D information is to use laser sheet illumination to obtain a series of 2-D sections. Two-dimensional pictures have been reported of premixed flames in engines,[37-39] sprays in engines,[40] unconfined sprays [41] and gas jets.[42] A second limitation of the measurements carried out on sprays is that the techniques are either not sensitive to fuel in the vapor phase, as in the case of photography, shadowgraphy etc., or are equally sensitive to the liquid and vapor phases, as in the case of fluorescence. Thus the separate measurement of the liquid and vapor phases of a fuel spray using optical techniques is very difficult because of the lack of spectroscopic characteristics which differ significantly for fuel molecules in each phase.

Johnston [43] investigated spontaneous Raman scattering but concluded that in the C-H stretching region near 3000 cm^{-1} there were insufficient differences between the spectra of the vapor and liquid to allow their discrimination. (With the same technique, but with the gaseous propane injection, he was able to make gas phase air/fuel ratio measurements.[23,44]) Using a combination of visible light scattering and infra-red light scattering and absorption, Chraplyvy [45] and Tishkoff et al.[46] were able to separate the signal from each phase for an unconfined spray.

More recently, a laser-induced fluorescence (LIF) technique has been used to visualize in-cylinder air/fuel mixture distribution.[47-58] With this technique, spectrally separated fluorescence images of liquid and vapor phase fuel distributions can be obtained. The technique is, therefore, effective and helpful in analyzing the mixing process in the combustion chamber of engines. Melton has shown that spectrally separated fluorescence emissions from liquid and vapor fuel can be obtained by adding an exciplex forming dopant to the fuel [59-62] ; the vapor is mapped by fluorescence from a monomer whereas the liquid is tagged by the red-shifted fluorescence of the exciplex. The fuel, which is a hydrocarbon solvent, has no significant fluorescent emission of its own, and thus its evaporation is tracked by the exciplex-forming dopants. Quantitative fuel vapor concentration or even semiquantitative estimation requires that the fluorescent marker evaporates at nearly same rate as the bulk fuel. The initial implementation of the technique by Melton to visualize a spray from a hollow cone injector,[60] and subsequently by Bardsley et al.[21,63] in an internal combustion engine relied on naphthalene (NP) and N,N,N'N'-tetramethyl-p-phenylene-diamine (TMPD) as the exciplex forming constituents in decane-based fuel. More efforts have focused on developing quantitative calibrations for the exciplex method relating fluorescence intensity to mass concentration of fuel. Such a quantitative interpretation of the fluorescent images is possible because fluorescence intensity is directly proportional to the mass concentration of the fluorescing compound. Initial quantitative application of an exciplex system was done by Felton et al..[64] Melton [65] developed calibration procedures based on the calibration of light absorption, quantum yields, and other photophysical parameters. However, those procedures required that each parameter be correctly determined, and therefore the overall accuracy depended on the accuracy of a series of separate procedures. Rotunno et al.[62] developed direct calibration procedures for the liquid and vapor phase. These procedures involved the direct measurement of the fluorescence intensity of a known amount of liquid or vapor. However, in their vapor phase calibration, they measured absorbance of TMPD as a function of temperature and then used the molar absorption coefficient (ε) of TMPD from Berlman [66] to calculate the vapor phase molar concentration. Their vapor phase concentration of TMPD exhibited a significant discrepancy, by a factor 4, when compared with the direct-pressure measurement conducted by Felton.[64]

While the TMPD/naphthalene system is appropriate for diesel and gas turbine fuels, it is not appropriate for the 20 to 215° C boiling range of gasoline fuels, inasmuch as the normal boiling points for naphthalene and TMPD are in the range of 200 to 300° C. Specifically, a low-volatility marker in a high-volatility solvent will cause a significant underestimation of the initial fuel evaporation rate, a key parameter in engine ignition and performance. For this reason, current efforts has been focused on the development and calibration of exciplex systems that are appropriate to automotive gasoline fuels. Melton[67] has developed an exciplex system using fluorobenzene (FBZ) and triethylamine (TEA) in isooctane fuel. This exciplex system is expected to be virtually coevaporative with solvent (fuel) which is boiling in the temperature range 70° C to 110° C. However, it may not be useful for practical use as an exciplex system because the fluorescence emission from the monomer and exciplex overlap. Thus, it is difficult to spectrally resolve the vapor phase fluorescence from that of the liquid. On the other hand, Shimizu et al.[68] developed an exciplex system using a naphthalene (NP) and N,N-dimethylaniline (DMA) in gasoline fuel. In developing their calibration, they took a unique approach. Instead of presenting their vapor phase calibration as a special map of concentrations, they presented it in the form of a special map of equivalence ratios. However, they did not calibrate the liquid phase, but used its fluorescence to show whether or not liquid fuel was present.

The main drawback of the exciplex techniques is the fluorescence quenching by oxygen.[16-17] Therefore, in most engine applications a nitrogen environment is required. Nevertheless, applying this technique to the internal combustion engine is quite helpful in understanding liquid and vapor phase fuel distributions. Detailed information on spray structure, evaporation, and the evolution of the resulting vapor concentration field would help both to enhance fundamental understanding and to improve engine performance.

2.1.2. Flow velocity field visualization (PTV, PIV and MTV)

Optical methods are central to quantitatively measuring the motion of fluids, especially those that are turbulent. The ability to measure two-dimensional velocities over an extended planar region has become available with the advent of particle tracking velocimetry (PTV) [69] and the particle image velocimetry (PIV).[70] Both PTV and PIV require that photographs be made of particle-seeded flow illuminated by a sheet of light. The photographs must be interrogated posteriorly and automatically if the method is to be practical. For the case of PTV, the light source is multiply pulsed, resulting in encoded particle tracks (i.e., multiple images). Because individual particle tracks must be identified and their displacements measured, the particle seeding density must be low enough to identify individual tracks unambiguously. In practice, this results in the velocity data density being both low and random. With PIV only two short light pulses are used, resulting in a recorded image pair for each particle. In contrast to PTV, the seeding density of PIV can be increased sufficiently that the velocity can be measured on a closely spaced regular grid.

In the PIV application, a fluid is seeded with millions, sometimes billions, of particles depending on the volume of interest (10,000 particles per cc of fluid).[71] A sheet of laser light illuminates a section of the flow and the reflection of light from the particles identifies their positions. A subsequent laser sheet of light records the particles' positions at a later interval. By comparing the photographs, the particles' positions are correlated with highly sophisticated computer algorithms thereby reflecting the velocity of the fluid for defined groups of particles. The PIV technique is powerful because it instantaneously measures the velocity of a fluid at many points - a key measurement to any fluid physicist or engineer. Nevertheless, the technique has many drawbacks, all of which arise from the need to measure the flow velocity with particles. First, particles are illuminated by a plane of light and subsequent illumination relies on the particles staying within the layer so that they may be illuminated at some later time. Second, the particles have their own inertia and they therefore may not track the flow, especially when it changes suddenly. Third, particles may not go into areas of interest. For instance, particles do not go into areas of high turbulence or in areas near surfaces.

The recent development of MTV (Molecular Tagging Velocimetry) by a group at Michigan State University [72] has eliminated the problems of PIV when the particle markers were replaced with luminescent supramolecules. In MTV,[73] a flow is seeded with supramolecules. A grid of laser lines is imposed upon the flow to produce a glowing supramolecular grid; the intersecting lines of the grid define points that follow the flow for a brief time (from microseconds to milliseconds depending on flow speed). The glowing grid by the supramolecules is imaged with CCD cameras as it convects with the flow. It is therefore easy to record how the grid deforms in time and, by measuring the distance and direction each grid intersection travels and knowing the time delay between each image, the two velocity components in the grid plane can be calculated, and the corresponding turbulence intensities, the Reynolds stress, and the vorticity calculated. A second camera allows one to record the third velocity component. As with PIV, MTV is an instantaneous velocity measurement, but it is non-intrusive. Since the supramolecules are part of the flow, all the problems associated with particles in the PIV technique are eliminated by the MTV technique. The trick in implementing MTV comes in the supramolecular design - the grid must exist long enough to follow the flow. Since fluid flows are slow, luminescent tracers with high emission quantum yields and a long excited state lifetimes (> milliseconds) that are not quenched by water or oxygen are necessary.

The MTV technique has allowed one to probe many problems that were previously elusive to the fluid physicist or mechanical engineer. These include the independent velocity fields of liquid, and solid, in two phase liquid/solid flows,[70] the leading edge problem at airfoils,[75-76] and a quantitative measure of complex flow of swirl and tumble (rotational flow about the cylinder axis and perpendicular to the cylinder axis, respectively) within the cylinder of an engine[77-78] and other flow issues in internal combustion engines.[3]

2.2. Photochemistry

2.2.1. Spectroscopy

Spectroscopy is the general term for all the techniques that involve the exchange of energy between electromagnetic radiation and matter. The two most familiar subcategories of spectroscopy are absorption spectroscopy, in which energy is transferred from the radiation to the sample, and emission spectroscopy, in which the sample loses energy, and this energy appears as radiation. In general, excited molecules may lose their excitation energy very rapidly by undergoing a radiationless transition to a lower electronic state of the same multiplicity.[79] This process is referred to as an internal conversion (IC). Figure 1 shows that internal conversion is followed by vibrational relaxation (VR) to the ground vibrational state. The excited singlet molecule (S_1) may also return to the ground state (S_0) with the emission of fluorescence (F) or it may undergo inter-system crossing (ISC) to the triplet state T_1. Inter-system crossing refers to a radiationless transition between the state of different multiplicity. Because of the spin interchange involved in intersystem crossing, the rate constant for this process is 10^{-2} to

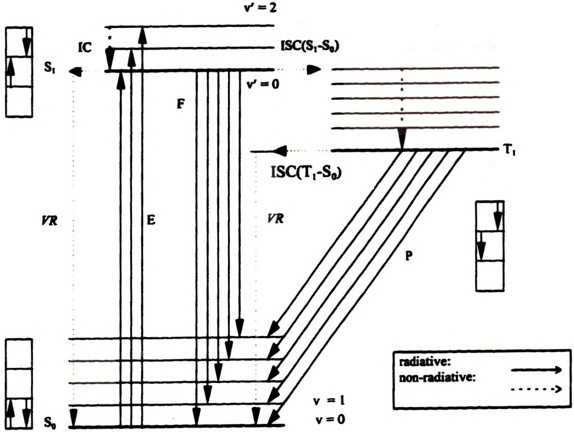

Figure 1. State diagram for a molecule showing the various intermolecular processes resulting from the absorption of radiation.[79]

10^{-6} (sec^{-1}) as fast as for internal conversion. The triplet molecules can phosphoresce (P), or undergo an inter-system crossing to the S_0 state. The radiation emitted in a transition between the states of the same multiplicity (i.e., singlet-singlet or triplet-triplet transitions) is called fluorescence, and the radiation emitted in a transition between states of different multiplicity is called phosphorescence.[79] Phosphorescence lifetimes are generally considerably longer than the fluorescence lifetimes because radiative transitions between states of different multiplicities are quantum mechanically forbidden to a first approximation.[79] Figure 2 is a simplified representation of the intermolecular processes that may occur.

2.2.2. Quenching Mechanism

A. Steady-state (intensity) quenching

The intensity of fluorophore fluorescence can be quenched by ground-state quencher-fluorophore reactions (static quenching), and by excited state quencher-fluorophore reactions (dynamic quenching). Static quenching is assumed to result from the formation of a non-fluorescent quencher-fluorophore complex in the ground state. Shifts of the fluorophore absorption spectrum with added quencher provide evidence of such a complex formation. Another type of static quenching is often observed at high quencher concentrations due to the existence of increasing numbers of quencher-fluorophore pairs in which the quencher is close enough to the fluorophore to instantaneously quench its excited state.[80] Treatment of this type of quenching is less straightforward. However, it can be distinguished from quenching due to true ground-

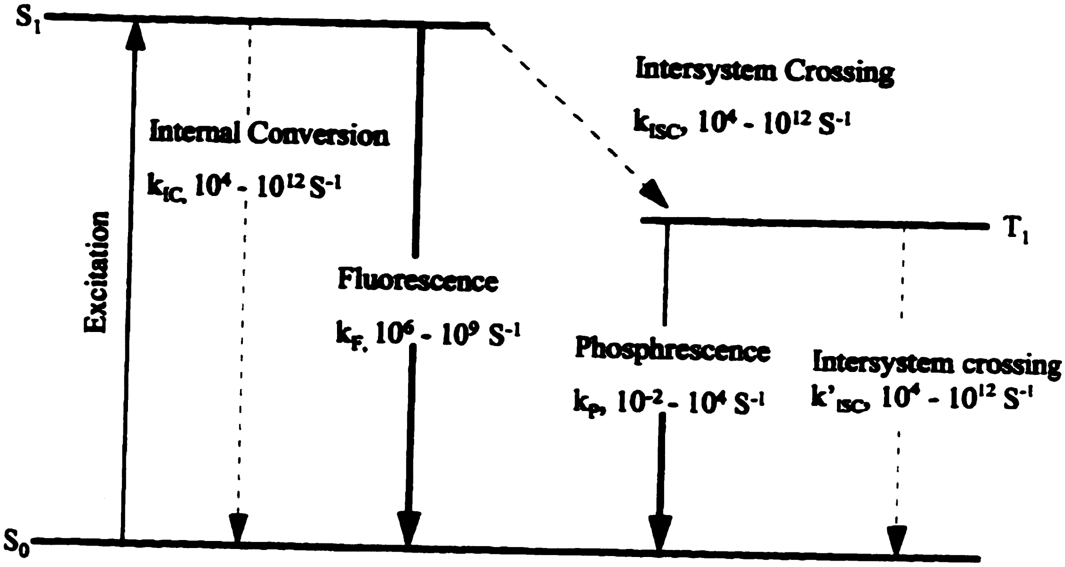

Figure 2. Abbreviated version [79] of the preceding Fig.1.

state complex formation because it does not produce changes in the fluorophore absorption spectrum. The steady-state parameter which responds to the added quencher is the fluorescence quantum yield (ϕ_f), which is defined as the ratio of the rate of fluorescence emission to the rate of absorption (photons out/ photons in). The fluorescence quantum yield in the absence of a quencher (ϕ_f^0) is defined by the mechanism as shown below. A and A* are the fluorophore ground-state and emitting-state (lowest excited singlet), respectively. k_A and k_f are the rate constants for photon absorption and fluorescence emission, respectively, and k_{nr} is the sum of first-order rate constants for non-radiative decay modes, such as internal conversion and intersystem crossing. n_A and n_{A^*} are the number of fluorophores in the ground and excited state, respectively. The rate mechanism of this process is given by

$$A + h\nu \rightarrow A^*, \qquad Rate = k_A n_A$$

$$A^* \rightarrow A + h\nu, \qquad Rate = k_f n_{A^*}$$

$$A^* \rightarrow A \qquad Rate = k_{nr} n_{A^*}$$

Since steady-state conditions exist, we can assume:

$$k_A n_A = (k_f + k_{nr})\, n_{A^*}, \quad (dn_{A^*} / dt) = 0 \tag{1}$$

Rearranging Eq. (1) gives:

$$n_{A^*} = k_A n_A / (k_f + k_{nr}) \tag{2}$$

The ϕ_f is formally defined as:

$$\phi_f = (fluorescence\ rate) \,/\, (absorption\ rate) = k_f n_{A^*} / k_A n_A \tag{3}$$

Combining Eqs. (2) and (3) gives the familiar form for the fluorescence quantum yield in the absence of quencher (ϕ_f^0):

$$\phi_f^0 = k_f / (k_f + k_{nr}) \qquad (4)$$

When quencher [Q] is added, another A* decay mechanism is now possible, where k_q is the second-order rate constant for quenching and the product $k_q[Q]$ is pseudo first-order.

$$A^* + Q \rightarrow A + Q, \qquad Rate = k_q[Q]n_{A^*} \qquad (5)$$

Now Eq. (2) becomes:

$$n_{A^*} = k_A n_A / (k_f + k_{nr} + k_q[Q]) \qquad (6)$$

Combining Eqs. (3) and (6) gives an expression for the fluorescence quantum yield in the presence of a quencher, providing dynamic quenching (Eq. 5) is the only quenching mechanism.

$$\phi_f = k_f / (k_f + k_{nr} + k_q[Q]) \qquad (7)$$

Dividing Eq. (4) by Eq. (7) produces the familiar Stern-Volmer equation;[75]

$$\phi_f^0 / \phi_f = 1 + k_q[Q] / (k_f + k_{nr})$$

In the more familiar form of this equation ϕ_f^0 and ϕ_f are replaced by F^0 and F, the intensities of fluorescence at a given wavelength, in the absence and presence of Q, respectively, and the term $[k_q / (k_f + k_{nr})]$ is set equal to K_{SV}, the Stern-Volmer quenching constant.[80]

$$F^0 / F = 1 + K_{SV}[Q] \qquad (8)$$

If this quenching mechanism alone obtains, a plot of F^0/F versus [Q] is linear with an intercept of 1 and a slope equal to K_{SV}. When quenching can also occur by ground-state complex formation (static quenching), another reaction must be considered in the overall quenching mechanism:[81]

$$A + Q \rightleftarrows AQ \rightarrow AQ^{*} \rightarrow AQ + heat$$

Where K is defined as,

$$K = [AQ]_{\text{con.}} / ([A]_{\text{con.}}\ [Q]_{\text{con.}}) \qquad (9)$$

K is the equilibrium constant for the formation of the "dark" complex, AQ. If both static and dynamic quenching are occurring, the intensity ratio (F / F^0) can be expressed as the fractional reduction due to quenching of A* (dynamic) times the fractional reduction due to complexation of A (f, static).[80]

$$F / F^0 = (1 + K_{SV}[\mathrm{Q}])^{-1} f$$

The reaction f can be expressed in the following way, given the definition of K in Eq. (9):

$$f = [\mathrm{A}] / ([\mathrm{A}] + [\mathrm{AQ}]) = (1 + K[\mathrm{Q}])^{-1}$$

Thus, it follows that

$$F / F^0 = (1 + K_{SV}[\mathrm{Q}])^{-1}\ (1 + K[\mathrm{Q}])^{-1}$$

This, in turn, can be rearranged to give a modified form of the Stern-Volmer equation:

$$F^0 / F = (1 + K_{SV}[\mathrm{Q}])\ (1 + K[\mathrm{Q}]) \qquad (10)$$

Eq. (10) predicts an upward curvature of the plot of F^0 / F versus [Q] in the event that both static and dynamic quenching are occurring. If quenching only occurs by the static mechanism (k_q, $K_{SV} = 0$), Eq. (10) simplifies to:

$$F^0 / F = 1 + K[Q] \qquad (11)$$

Eq. (11) also predicts a linear relation between F^0 / F and [Q] with an intercept of 1, as does Eq. (8) derived for the case where dynamic quenching alone is occurring. In the former case the slope equals K, while in the latter equals K_{SV}. Thus, one can not determine whether quenching is static or dynamic on the basis of a single linear Stern-Volmer plot. If such plots are obtained as a function of temperature, a determination might be made from the change in slope. Increased temperature often causes the slope (K_{SV}) to increase if quenching is dynamic (k_q increases with temperature), while the slope (K) should decrease with increasing temperature if the quenching is static.[80]

B. Time-resolved (dynamic) quenching

When fluorescence is excited by a pulsed, rather than a continuous source, the decrease of fluorophore fluorescence after the pulse normally follows a single exponential decay in solution. The lifetime of fluorescence, defined as the time for the fluorescence signal to decay to 1/*e* of its original value, is given by Eq. (12) in the absence of a quencher and Eq. (13) in the presence of a quencher.

$$\tau^0 = (k_f + k_{nr})^{-1} \qquad (12)$$

$$\tau = (k_f + k_{nr} + k_q[Q])^{-1} \qquad (13)$$

Dividing Eq. (12) by Eq. (13) gives another form of the Stern-Volmer equation, which applies only if quenching is dynamic.

$$\tau^0 / \tau = 1 + k_q[Q] / (k_f + k_{nr}) = 1 + k_q \tau^0 [Q] \qquad (14)$$

The Stern-Volmer constant (K_{SV}) obtained from steady-state measurements is equal to $k_q\tau^0$. Thus, if lifetime measurements are possible, the value of k_q can be extracted from plots of Eq. (14) or Eq. (8) and the value of the lifetime in the absence of quencher (τ^0). It is important to note that lifetime measurements are not affected by the formation of a ground-state "dark" complex (AQ). Consequently, lifetime measurements can be used to separate dynamic quenching from static.

2.2.3. Excitation and emission dynamics

For a quantitative calibration of in-cylinder fuel mixture formation, the measured fluorescence intensity must be correlated to the concentration of the seeded molecules. The relationship between fluorescence intensity and the concentration of the fluorescence medium can be determined by means of the Lambert-Beer law. The transmitted laser intensity I_t which results from propagation in a uniform fluorescent medium of thickness b (*cm*) is defined by the following equation;

$$I_0 / I_t = \exp(\varepsilon c b)$$

where I_0 is the incident laser intensity, ε is the absorption coefficient ($cm^{-1}\ mol^{-1}$) of the medium and c is the concentration (*mol*) of the fluorescent medium. The relaxation phase of the excited fluorescent medium is characterized by radiative and non-radiative processes. Representing the rate constants (s^{-1}) of the radiative process and non-radiative process by k_f and k_{nr} respectively, the time-dependent number density of the molecules in the excited states, $n_{A^*}(t)$ is given by:

$$n_{A^*}(t) = n_{A^*}\, exp(-[k_f+k_{nr}]t)$$

where n_{A^*} is the number of the excited molecules formed in the medium per excitation pulse. The fluorescence intensity at time t is given by;

$$I_f(t) = k_f\, n_{A^*}\, exp(-[k_f+k_{nr}]t) \qquad (15)$$

The fluorescence intensity per pulse and per unit volume is thus obtained by integrating Eq. (15) :

$$I = \int I_f(t)dt = (k_f/[k_f+k_{nr}])\, I_0 b^{-1}\, (1-\exp[-\varepsilon cb]) \qquad (16)$$

The first parenthetical term in Eq. (16) is the fluorescence quantum yield in the absence of quencher (ϕ_f^0) defined in the previous section as the ratio of fluorescence emission to the rate of absorption (photons out/photons in). Thus Eq. (16) can be rewritten ;

$$I = \phi_f^0\, I_0 b^{-1}\, (1-\exp[-\varepsilon cb]) \qquad (17)$$

The fluorescence signal per laser pulse and per unit volume collected by each pixel of the detector array can be expressed as

$$S_f = [\eta\beta\Omega/4\pi][\phi_f^0][I_0 b^{-1}\, (1-\exp[-\varepsilon cb])] \qquad (18)$$

where η is the collection efficiency of the optics, β is the detector efficiency, Ω is the solid angle of light collection. The first parenthetical term describes the overall efficiency of the optics and detector, second and third terms describe the quantum yield and the total number of species molecules per unit volume.

2.3. Laser induced fluorescence (LIF)

Fluorescence is the emission of light (photons) from an electronically excited state of an atom or molecule. In LIF, the target species absorbs energy from a laser that is tuned so that the photon's energy, hv, is exactly equal to the energy difference, ΔE, in electronic states. The photon energy is then in resonance with ΔE. The lowest state is the ground electronic state. Once excited, the species has several ways to return to the ground state (de-excited). Firstly, if the molecules are already in a resonantly excited state, the laser energy can stimulate de-excitation. Secondly, it may spontaneously release energy (fluorescence) back to the ground electronic state. Thirdly, the excited molecule may transfer energy in a non-radiative fashion through collisions with other atoms or molecules. These transfers are reflected through changes in the vibrational or rotational energy levels (or a combination thereof) represented by V(J) and R(J), respectively, where J is the total angular momentum quantum number. Additionally, energy may be absorbed by the molecule, resulting in elevation to a higher electronic dissociative state. A thorough analysis of molecular spectroscopy is provided by Banwell.[82]

The mathematical and physical description of LIF can be described by a two level model, as shown in Fig. 3. The rate of stimulated absorption is denoted as W_{12}. Stimulated and spontaneous emission from the upper level is represented by W_{21} and A_{21}. The collisional quenching terms are grouped together and denoted as Q_{21}. All rates are in s^{-1}. The population [molecules] in the lower level, before excitation, is N_1^0. After

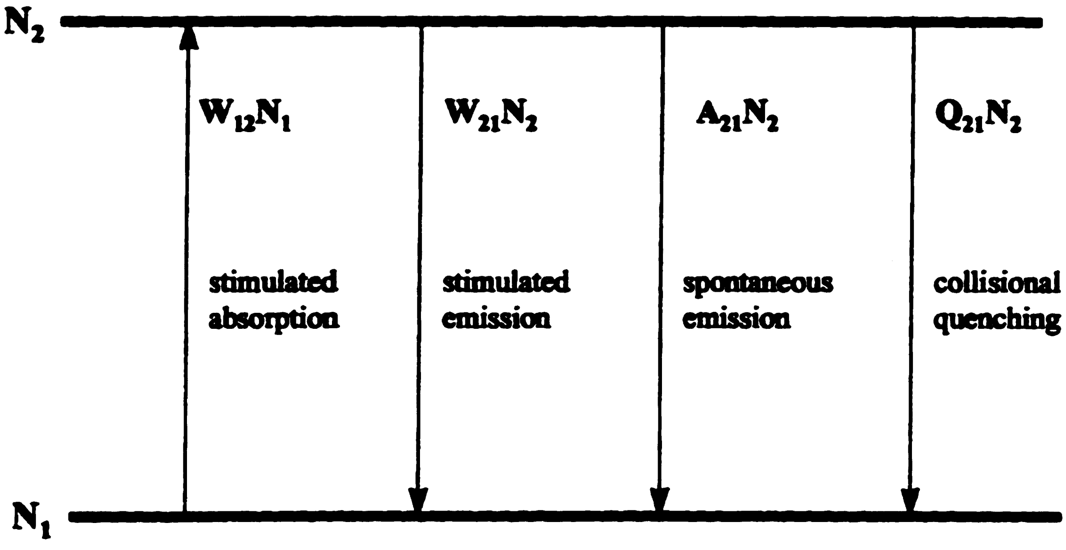

Figure 3. Two-level model for laser-induced fluorescence. W_{12} and W_{21} represent the rates (s^{-1}) of stimulated absorption and emission. A_{21} is the rate of spontaneous emission, and Q_{21} is the rate of non-radiative quenching.

resonant excitation, $N_1 + N_2 = N_1^0$. The rate equations for the population in each level are given by

$$\frac{dN_2}{dt} = W_{12}N_1 - (W_{21} + A_{21} + Q_{21})N_2$$

$$\frac{dN_1}{dt} = -W_{12}N_1 + (W_{21} + A_{21} + Q_{21})N_2$$

At the peak of the laser pulse, the populations are at steady state, and the population of the upper level is given by

$$N_2 = \frac{W_{12}}{W_{21} + A_{21} + Q_{21}} N_1$$

Under conditions of a weakly perturbing laser (low irradiance), the lower level population can be assumed to be approximately constant; and both W_{12} and W_{21} are small. Then the upper state population can be expressed as

$$N_2 = \frac{W_{12}}{A_{21} + Q_{21}} N_1^0 \qquad (19)$$

The fluorescence signal, seen by a detector, S_f (photon), is proportional to the fraction of the upper state population that spontaneously de-excites $S_f \propto A_{21} \cdot N_2$, or, using Eq. (19) and rearranging

$$S_f \propto W_{12} N_1^0 \cdot \left(\frac{A_{21}}{A_{21} + Q_{21}} \right)$$

where the parenthetical term $A_{21}/(A_{21}+Q_{21})$ is the fluorescence yield, F_y, which is the fraction of the total excited state population that de-excites via fluorescence.

The rate of stimulated absorption can be written to reflect the coupling of the laser with the absorbing molecules

$$W_{12}N_1^0 = B_{12}I_\nu n_1 V,$$

where B_{12} is the Einstein B coefficient for absorption ($cm^2 \bullet cm^{-1} \bullet J^{-1}$), I_ν is the laser spectral irradiance ($W/cm^2 \bullet cm^{-1}$), n_1 is the number density of the absorbing species (cm^{-3}), and V is the volume (cm^3) of gas illuminated by the laser. The Einstein B coefficient describes the strength of coupling between the upper and lower levels, so that the term $I_\nu B_{12}$ expresses the probability for absorption of a photon by the coupled molecules during the time duration of the laser pulse.

The fluorescence signal per laser pulse collected by each pixel of the detector array from a volume of fluid, V_c, intersected by the laser can be expressed as[83]

$$S_f = \left(\eta\varepsilon\frac{\Omega}{4\pi}\right)\cdot\left(f_B N_T V_C\right)\cdot F_y \cdot\left(I_\nu B_{12}\right)$$

where η is the collection efficiency of the optics, ε is the detector efficiency, Ω is the solid angle of light collection, f_B is the Boltzmann population fraction, and N_T is the total number of excited species. The first parenthetical term describes the overall efficiency of the optics and the detector. The second parenthetical term describes the total number of species molecules within the volume V_c.

The absorption linewidth is typically described by a Voigt profile, which consists of both Lorentzian and Doppler (Gaussian) profiles. The Lorentzian profile is the result of the radiative decay rate of the excited state, which consists of the spontaneous decay rate plus the rate due to molecular collisions (which are a function of gas density). The Lorentzian portion of the lineshape, therefore, is dependent on the temperature, pressure and collision partners. The spectral coupling of the laser lineshape with the absorption lineshape is reflected by the overlap integral, g(v),[84-85] and $I_v = Ig(v)$, where I is the laser irradiance (W/cm^2), independent of frequency. The overlap integral is given by

$$g(v) = \int_V \phi_l(v)\phi_{abs}(v,T,P)dv$$

where φ_l and φ_{abs} are the lineshape functions of the laser and the absorption, respectively. The fluorescence signal is then

$$S_f = \eta\varepsilon\frac{\Omega}{4\pi}\cdot f_B N_T V_c \cdot F_y \cdot IB_{12}\int_V \varphi_l(v)\cdot\varphi_{abs}(v,T,P)dv\,.$$

At atmospheric pressure, the laser linewidth is typically much greater than the absorption linewidth, resulting in an overlap integral that approximates the absorption linewidth. Thus, at atmospheric pressure, the entire absorption spectral band couples to some portion of the laser spectral band, and there is little dependence of the strength of the fluorescence signal on the surrounding environment. However, as pressure increases, the absorption linewidth broadens due to the increased number of collisions. In this case, the absorption linewidth can exceed the laser linewidth. The coupling of the laser spectral distribution with the absorption spectral band is inefficient, resulting in the excitation of fewer molecules (therefore, a decreased fluorescence signal compared to the signal at atmospheric pressure), and the coupling becomes a function of the combustion environment in temperature, pressure, and collision partners.

Laser diagnostics improves understanding of combustion phenomena because they provide remote, space-, time-, and species-resolved measurements of combustion parameters.[86] Laser induced fluorescence techniques are well suited to the detection of reactive species.[87-89] They are widely applied as diagnostic tools for investigations of fuel distributions in internal combustion engines, atmospheric chemistry, combustion and plasma process, where a detailed understanding of certain chemical reaction pathways is desired. Eckbreth [90] summarizes the development of different LIF methods and their application to the measurement of species concentrations and temperature in combustion environment. Using two-dimensional LIF schemes, a wealth of unique information has been acquired;[91] it may often be sufficient to measure the approximate concentration and relative spatial distribution of the molecule under investigation. There are situations where concentrations of reactive intermediates should be measured quantitatively with the best attainable accuracy. This is required, for example, for a meaningful comparison of experimental data with the predictions of combustion models, including detailed chemical reaction schemes, e.g. a flame model which simulates the formation of pollutants.

LIF is often the only diagnostic technique which can provide the desired information without perturbing the combustion process. To obtain absolute concentration of important intermediates from the measured fluorescence signals, suitable strategies for calibration must be developed and tested, often in rather simple combustion environments, before they can be applied to measure the data of the desired accuracy.

2.4. Thermodynamics

The vapor pressure of all liquids vary with saturation temperature in essentially the same manner. The dependence of the saturation pressure on the temperature will now be developed from theoretical considerations. The generalized relationship that results is also valid for solid-gas and solid-liquid phase changes. One begins by calculating the entropy change of a sample substance during a phase change. This entropy change in terms of the variables v (molar volume (V/n), where n is the number of moles and s is the entropy) and T can be represented as

$$ds = \left(\frac{\partial s}{\partial v}\right)_T dv + \left(\frac{\partial s}{\partial T}\right)_v dT$$

However, for any first order process involving a change in phase, the temperature is constant during the phase change. Therefore the above equation reduces to

$$ds = \left(\frac{\partial s}{\partial v}\right)_T dv$$

The quantity $(\partial s / \partial v)_T$ can be replaced using the Maxwell relation $(\partial s / \partial v)_T = (\partial P / \partial T)_v$. Hence

$$ds = \left(\frac{\partial P}{\partial T}\right)_v dv$$

The term $(\partial P / \partial T)_v$ is the slope of the saturation curve at a given saturation state, and this quantity is independent of the volume during a change of phase. Consequently, the partial derivative may be written as a total derivative *dP/dT*, and it may be moved outside the integral sign during the integration of the above equation. Integration leads to

$$s_2 - s_1 = \frac{dP}{dT}\left(v_2 - v_1\right)$$

or

$$\frac{dP}{dT} = \left(\frac{s_2 - s_1}{v_2 - v_1}\right) \tag{20}$$

where the subscripts "1" and "2" represent the two phases in the process. For example, they may represent the saturated-vapor and saturated-liquid phase during a vaporization process.

The entropy change during a phase change may be evaluated from the first and second laws. From the second law $ds = \delta q / T$, and for a constant-pressure process (such as a phase change) the first law for a closed system is $\delta q = \delta h$. Thus $ds = dh / T$ and $s_2 - s_1 = \left(h_2 - h_1\right) / T$. Eq. (20) then becomes

$$\left(\frac{dP}{dT}\right) = \frac{h_2 - h_1}{T(v_2 - v_1)} = \frac{\Delta h}{T \Delta v} \tag{21}$$

This equation is called *Clapeyron equation*. It is generally valid for any phase change which occurs at constant pressure and temperature. For a liquid-vapor phase change this equation may be written as

$$\frac{dP}{dT} = \frac{h_{fg}}{T v_{fg}} \tag{22}$$

In general, Δh and Δv are the enthalpy and volume changes between any two saturation states at the same pressure and temperature. Note that the Clapeyron equation permits the evaluation of enthalpy changes for phase changes from a knowledge of only PvT data. For liquid-vapor and solid-vapor phase changes, Eq. (21) can be further modified by introducing several approximations. One considers only the liquid-vapor phase change, but the results are equally applicable to solid-vapor phase changes (sublimation). For liquid-vapor phase changes at relatively low pressure, the value of v_g (gas phase volume) is many times the size of v_f (liquid phase volume). Thus a good approximation is to replace v_{fg} by v_g in the above equations. Also, at these low pressures, the PvT relation for the vapor closely follows that for an ideal gas, v_g = RT/P. By making these two successive approximations in Eq. (22), we find that

$$\frac{dP}{dT} = \frac{Ph_{fg}}{RT^2}$$

$$\frac{dP}{P} = \frac{h_{fg}dT}{RT^2} \qquad (23)$$

Eq. (23) is frequently called the *Clausius-Clapeyron equation*. Integration of this equation depends on the variation of h_{fg} with temperature. If a small variation of pressure (or temperature) is chosen so that the change in h_{fg} over the interval of integration is small, then integration yields

$$\ln P = -\frac{h_{fg}}{R}\left(\frac{1}{T}\right) + C \qquad (24)$$

where C is a constant of integration. This indicates that the vapor pressure of a liquid is very closely an exponential function of the saturation temperature. The general form of the equation is also valid for saturation data below the triple point in the sublimation region.

2.5. Droplet vaporization

2.5.1. General characteristics

Vaporization of liquid hydrocarbon fuel is a prerequisite to combustion. Any fuel unvaporized at the combustor exit is wasted. In addition, it may have the detrimental effects of eroding metal surfaces. Fuel barely vaporized at the combustor exit may have insufficient time to burn. Again there is wastage, plus possible deposition or endothermic decomposition. Direct fuel injection into a combustion chamber is encountered in a wide range of applications such as industrial heaters, diesel and direct injection gasoline engines, jet engines, gas turbines, etc. The liquid fuel injection results in the formation of droplets through atomization mechanisms that depend on the system operating conditions. The individual droplet processes are of primary importance in spray combustion, since in many instances the droplets are well separated from each other. Droplet vaporization is therefore an important parameter in the modeling of the above systems and can be the controlling factor for energy conversion rates, mixture ratio distributions, and overall combustor behavior. Present understanding of droplet vaporization and spray combustion is summarized well in review articles by Law,[92] Sirignano,[93] and Faeth.[94]

A sketch of the droplet evaporation process is provided in Fig. 4, for the hypothetical case in which a pure fuel drop is instantly introduced into a gas at elevated temperatures. At typical injection temperatures, the fuel concentration at the liquid surface is low, and there is little mass diffusion from the drop early in the process. Under

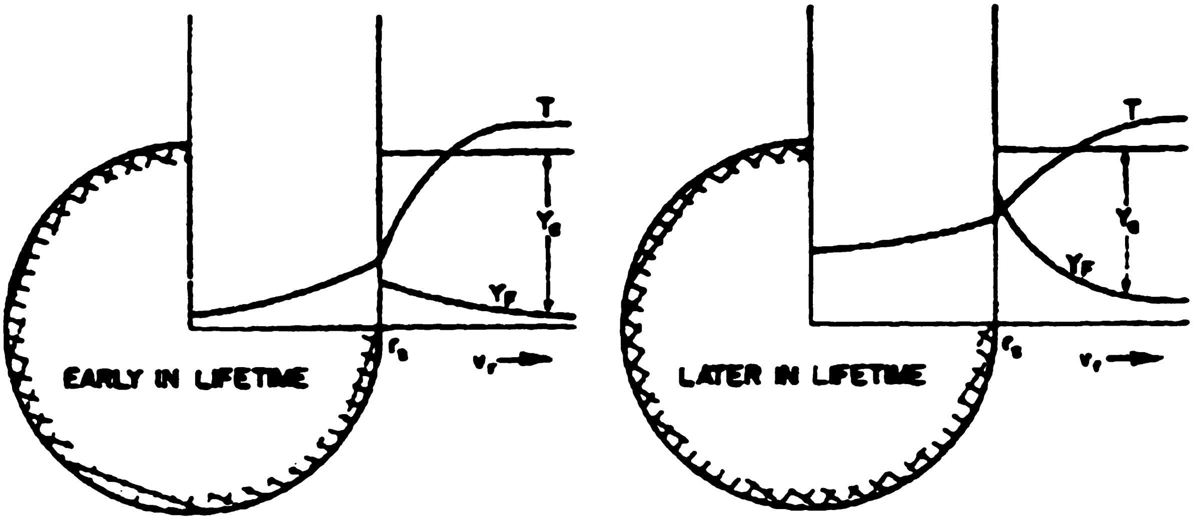

Figure 4. Sketch of the drop vaporization process.[94] Where T is the temperature, r_s is the droplet radius, v_r is the radial velocity, and Y_a and Y_F are mass fraction of ambient gas and fuel, respectively.

these conditions, the droplet heats up, much like any other cold body placed in a heated environment. In general, temperatures are not uniform within the droplet, with the maximum liquid temperature located at the surface. As the liquid temperature rises, the rate of mass transfer increases as a result of higher fuel vapor concentration at the drop's surface. This has two effects: (1) an increasing portion of the energy reaching the drop surface must supply the heat of vaporization of the evaporating fuel, and (2) the outward flow of fuel vapor in the boundary layer reduces the rate of heat transfer to the droplet. This slows the rate of increase of the liquid surface temperature and later in the process temperatures become more uniform in the liquid phase. Eventually, a stage is reached where all the heat reaching the surface is utilized for the heat of vaporization and the droplet stabilizes at a temperature called the "wet bulb temperature".[94]

2.5.2. Simple model of droplet vaporization

A. Simple model of droplet

The simplest analysis of droplet evaporation has been reviewed by Faeth[94] and can be understood with the following assumptions:

(1) The droplet is assumed to be spherically symmetric.

(2) The gas phase is assumed to be a quasi-steady continuum, which always adjusts to the steady-state structure for the imposed boundary conditions at each instant of time.

(3) Fluid properties are assumed to be constant, with property values determined at an appropriate reference condition. The liquid fuel is assumed to be a single pure component.

(4) The relationship between gas phase fuel concentration and liquid temperature is given by the vapor pressure correlation for the pure liquid, e.g., the Clausius-Clapeyron equation. Surface tension corrections are omitted.

(5) The ambient gases have negligible solubility in the liquid phase and only fuel is diffusing from the surface.

(6) The radial motion of the liquid surface is assumed to be small.

(7) The pressure is everywhere equal to the ambient pressure.

(8) Radiation is neglected.

(9) Mass diffusion is represented by an effective binary diffusion law and the Dufour effect is neglected in the heat flux.

(10) Reaction effects, such as fuel decomposition, are neglected. For convenience here, the Lewis number will be assumed to be unity.

It must be expected that these assumptions become invalid at very low pressure (below 1 atm), for small drops (on the order of 1 μm or less), at pressures approaching the thermodynamic critical point of the fuel, and in the presence of very luminous flames.[94]

B. Droplet vaporization

a. Heat-transfer controlled vaporization

During vaporization, relatively volatile solutes are probably rapidly heated to their boiling points, after which vaporization of the material occurs. If the boiling point of the material is appreciably lower than the ambient temperature, conduction of heat from the ambient gases to the surface of the solute will likely be the rate-limiting process for vaporization. Given this condition, the vaporization rate will be influenced by ambient temperature and the thermal conductivities of the ambient gases and solute vapor, just as for desolvation. The vaporization rate equation can be represented by[95]

$$D_0^2 - D^2 = k_1 t \qquad (25)$$

where D is the droplet diameter at any time t after its entry into a test-section, D_0 is the initial droplet diameter, and k_1 is the vaporization rate. Because this process is heat-transfer controlled, the vaporization rate k_1 depends on the thermal conductivity of the gases surrounding the droplet, the ambient temperature, and several other parameters. As the temperature difference between the boiling point of the solute and the ambient gases become less, mass-transfer control could become the rate-limiting mechanism.[96]

b. Mass-transfer controlled vaporization

Mass-transfer controlled vaporization of a droplet would be limited by the diffusion of gaseous solute away from the droplet; the vaporization rate would then depend upon the diffusion coefficient of the solute vapor, the solute volatility, and the ambient temperature. For the large droplets, the vaporization rate equation would be described by a relation similar in form to Eq. (25).[95]

In the case of very small droplets, mass-transfer controlled vaporization would follow Eq. 26 and 27 below:[95]

$$-dm/dt = k_2 D^2 \qquad (26)$$

$$D_0 - D = k_3 t \qquad (27)$$

where m is the mass of solute lost during vaporization, the k's are constants, and D refers to droplet diameter. Eq. (27) follows from Eq. (26) because the mass of the droplet is proportional to D^3. Eqs. (26) and (27) apply only to droplets whose diameters are small (less than 0.1 μm) compared to the diffusion layer surrounding the droplet. The diffusion layer is on the order of one mean free path length.[95]

2.5.3. Kinetics of droplet vaporization

A. Gas phase equations

The basic conservation equations for the gas are given in Refs.[97-99] Under the previous assumptions for the droplet in Section 2.5.2. they become:

Conservation of mass:

$$\frac{d}{dr}\left(\rho r^2 v_r\right) = 0 \qquad (28)$$

Conservation of species:

$$\frac{d}{dr}\left[r^2\left(\rho v_r Y_i - \rho D'\frac{dY_i}{dr}\right)\right] = 0 \qquad (29)$$

Conservation of energy:

$$\frac{d}{dr}\left[r^2\left(\rho v_r C_p\left(T - T_\infty\right) - k\frac{dT}{dr}\right)\right] = 0 \qquad (30)$$

where Y_i is the mass fraction of ambient gas or fuel. Since only the fuel has net mass transfer, D′ should represent binary diffusivity of the fuel with respect to other gas phase species; similarly, the fuel specific heat should appear in Eq. (30). By definition

$$\Sigma Y_i = 1 \qquad (31)$$

The analysis only considers two species, fuel and ambient gas. Therefore, through Eq. (31) only one conservation of species equation must be solved. Integration of Eq. (28) yields

$$r^2 \rho v_r = \dot{m}_f / 4\pi = const.$$

where $\dot{m}_f$ is the total fuel vaporization rate of the drop. The boundary conditions are

$$r = r_s; \qquad T = T_s, \quad Y_F = Y_{F_s}$$

$$r = \infty; \qquad T = T_\infty, \quad Y_F = Y_{F_\infty}$$

The fuel concentration and temperature at the liquid surface are related through the vapor pressure characteristics of the fuel

$$Y_{F_s} = f(T_s, p) \tag{32}$$

A final boundary condition is supplied by the insolubility assumption, which implies that the mass flux of ambient gas is zero at the liquid surface

$$r = r_s; \qquad \rho v_r Y_a - \rho D' \frac{dY_a}{dr} = 0$$

With the problem posed in this manner, knowledge of p, Y_{F_∞}, T_∞ and T_s provides Y_{F_s}, $\dot{m}_f$ and the heat transfer rate to the droplet. A heat transfer coefficient, which includes mass transfer effects, can be defined as follows

$$h = k\left(\frac{dT}{dr}\right) / \left(T_\infty - T_s\right)$$

Solution of the equations then yields the following

$$\frac{\dot{m}_f}{4\pi\rho D' r_s} = \ln\left(1 + B_y\right) \tag{33}$$

$$Nu = \frac{2hr_s}{k} = 2\ln\left(1 + B_y\right) / B_y \tag{34}$$

where B_y is Spalding's mass transfer number

$$\mathrm{B_y = (Y_{a\infty} - Y_{as})/Y_{as} = (Y_{Fs} - Y_{F\infty})/(1 - Y_{Fs})} \tag{35}$$

For high transfer rates where $Y_{F_s} \to 1$, B_y is a convenient driving potential for the definition of a mass transfer coefficient for the diffusion of one gas through a stagnant gas.

$$\dot{m}_f = 4\pi r_s^2 K'\left(Y_{F_s} - Y_{F_\infty}\right) / \left(1 - Y_{F_s}\right)$$

Substitution from Eq. (33) then yields the Sherwood number

$$Sh = \frac{2K' r_s}{\rho D'} = 2\ln\left(1 + B_y\right) / B_y \tag{36}$$

At low mass transfer rates, $B_y \to 0$, Eqs. (34) and (36) yield $Nu = Sh = 2$, which are the familiar values for a sphere at low mass transfer rates.

B. Liquid phase equations

In tests with suspended large drops, D >1000 μm, a number of investigators have observed circulation currents within the drop as it evaporated.[100-101] If the rate of circulation is rapid, the droplet temperature will be relatively uniform at each instant of time, in spite of the low thermal diffusivity of most liquids.[101] However, others have made measurements which indicate that circulation is stabilized for small drops and appreciable temperature gradients are present within the drop throughout its lifetimes.[102-103] The conservation of mass of the droplet liquid yields

$$\frac{d}{dt}\left(\frac{4}{3}\pi r_s^3 \rho_f\right) = -\dot{m}_f \tag{37}$$

Employing Eqs. (33) and (37) one finds an expression for the evaporation rate constant as follows

$$K = \frac{8k}{C_p \rho_f} \ln\left(1 + B_y\right) \tag{38}$$

For the case of a rapidly mixing drop, the liquid temperature is uniform and we have

$$mC_{p_f} \frac{dT_s}{dt} = 4\pi r_s^2 h\left(T_\infty - T_s\right) - \dot{m}_f h_{f_g} \tag{39}$$

The last term in Eq. (39) represents the energy required to evaporate the fuel. The initial conditions for Eqs. (37) and (39) are

$$t = 0; \qquad r_s = r_{s0}, \qquad T_s = T_{s0}$$

Eq. (39) can be rearranged so that the wet bulb state can be interpreted as follows

$$\frac{dT_s}{dt} = \frac{\dot{m}_f h_{f_g}}{mC_{p_f}}\left[\frac{B_T}{B_y} - 1\right] \tag{40}$$

where $B_T = C_p\left(T_\infty - T_s\right)/h_{f_g}$

By definition, the droplet temperature no longer changes with time at the wet bulb state and from Eq. (40)

$$B_{T_{WB}} = B_{Y_{WB}}$$

providing a relationship between concentration and temperature. A second relation is provided by the vapor pressure relation, Eq. (32) allowing solutions for $Y_{F_{WB}}$ and $T_{S_{WB}}$.[97] If the ambient temperature is high,

$$T_\infty - T_{S_{WB}} \doteq T_\infty - T_b$$

and if $Y_{F_\infty} = 0$, we have

$$Y_{F_{WB}} = B_T / \left(1 + B_T\right)$$

Since B_y is a constant at the wet bulb state, Eq. (38) indicates that K is a constant under these conditions, aside from variations due to convection. For the noncirculating drop, the energy equation for the liquid is

$$\frac{\partial T}{\partial t} = \frac{\alpha_f}{r^2} \frac{\partial}{\partial r}\left(r^2 \frac{\partial T}{\partial r}\right) \qquad (41)$$

The boundary conditions at the center and surface of the drop are

$$r = 0, \qquad \frac{\partial T}{\partial r} = 0$$

$$r = r_s(t), \quad k_f r^2 \frac{\partial T}{\partial r} = 4\pi r^2 h\left(T_\infty - T_s\right) - \dot{m}_f h_{fg}$$

The conservation of drop mass relationship, Eq. (37), is unchanged. Given the surface temperature, Eq. (32) provides Y_{F_s}, and Eqs. (32-35) yield the heat and mass transfer rates. The solution proceeds by integration of Eqs. (37) and (40) or (41). Analytical solutions are not known for these equations for realistic vapor pressure relations and numerical integration is normally employed for drop life time calculations.

2.6. Exciplex (excited state complex) fluorescence

A class of extremely important coupled reactions involve excimers and exciplexes. Many molecules will not associate or react with each other in the ground state. However, once one of them is in an excited state, it will undergo reactions with other normally non-reacting ground state species to form new transient excited state species. This is not a permanent chemical reaction, and when the new excited species decays, the original ground state species are formed. If the reactant is a ground state molecule of the same type, the new species is an excimer (excited state dimer). If the two species are different, they are called exciplex (excited state complex), although if the two species are similar, the term "mixed excimer" is sometimes used.[104]

The absorption and fluorescence spectra of organic molecules dissolved in nonpolar solvents, such as typical fuels, are virtually identical to the spectra of the same molecules in the vapor phase. However, in some cases it is possible to react the fluorescing excited state molecule, M*, with an appropriate ground-state partner, G, to form a second fluorescing species, M–G*, known as exciplex (E*). The fluorescence of this excited state complex E* is always red-shifted with respect to that of the excited monomer emission M* because the exciplex has a lower energy than unbound M*. The basic chemical mechanism is the same for all exciplex-based systems,[59,62,105] since they all contain three basic components; a monomer (M), a ground state reactant (G), and a solvent which serves as fuel. The exciplex is formed in the reversible equilibrium[106]

$$M^* + G \longleftrightarrow E^*$$

where M* is the first excited singlet state of the monomer, and E* is the exciplex. The equilibrium of equation, which governs the formation of the exciplex in the liquid but not the vapor, is controlled by adjusting the concentration of the ground state reactant (G). The wavelength of excitation source determines which excited electronic state is reached during the absorption transition. Figure 5 illustrates the individual steps of the exciplex mechanism. In the liquid phase, the equilibrium may be shifted far to the right by increasing the concentration of M and G. Upon vaporization, the concentration of the M and G will be reduced so that M* emission will dominate. Moreover, the equilibrium is temperature dependent, shifting to the left with increasing temperatures. Accordingly, the exciplex is less stable at elevated temperatures and the exciplex fluorescence emissions attenuated with respect to that for the monomer. The energy of an emitted photon from the fluorescence is given by

$$E = \frac{hc}{\lambda}$$

where h is Planck's constant, c is the velocity of light, and λ is the wavelength of the emission fluorescence. Since the exciplex emission has a lower energy its emission occurs at a longer wavelength than that of the excited monomer. Figure 6 shows the exciplex energy diagram. For this reason, in the laser induced exciplex fluorescence (LIEF) technique, the vapor phase fluorescence is dominated by M* and the liquid phase emission is characterized by the red-shifted emission of the exciplex.[59,105,107]

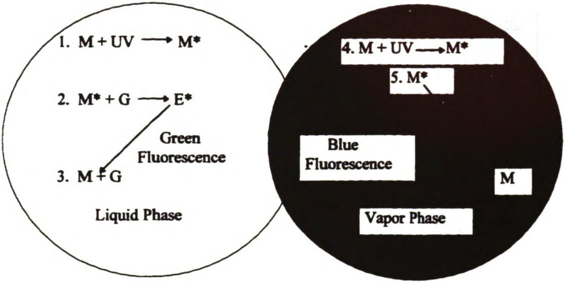

CONCEPT

1, 4 : Laser excitation of monomer in liquid or vapor
2 : Exciplex (excited state complex) formation, liquid phase only
3 : Exciplex emission fluorescence occurs in green
5 : Monomer emission fluorescence occurs in blue

Figure 5. The mechanism of exciplex liquid and vapor visualization systems.[67]

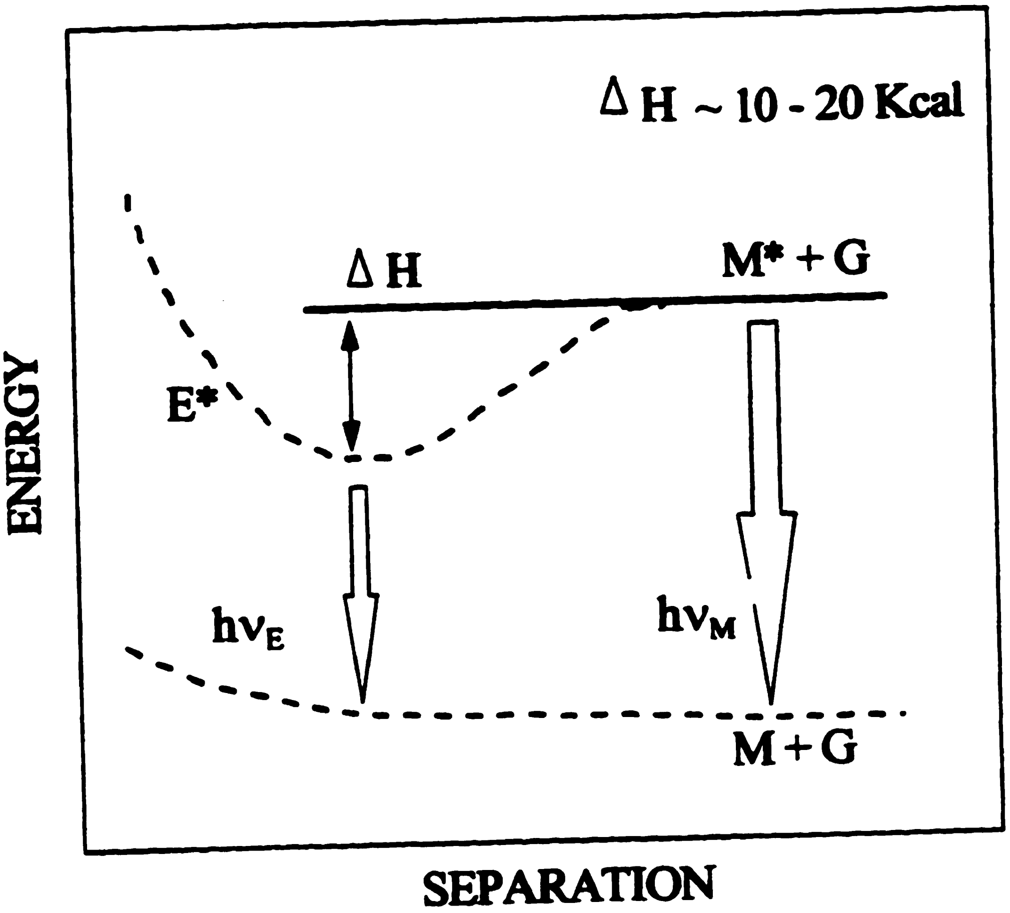

Figure 6. Exciplex energy diagram[67]

Chapter III. Experimental Methods (I): Development of New Exciplex Systems

3.1. Chapter overview

In a survey of potential exciplex-based vapor/liquid visualization systems, main selection criteria focused on the strong room temperature exciplex emission with a reasonable separation from the monomer emission and retention of substantial exciplex emission at temperatures as high as 200°C. Many existing possible exciplex systems [107] were investigated. However, none of them completely satisfied our criteria. Some yielded strong emission efficiencies but spectral separation between monomer and exciplex was not sufficient, or vice versa.

This chapter describes new vapor/liquid visualization systems based on an exciplex formed between dimethyl- or diethyl- substituted aniline and trimethyl-substituted naphthalenes in an isooctane solvent. Characterization methods employed steady-state and time-resolved fluorescence emission spectroscopy. Among the many systems and formulations investigated in this study, an exciplex consisting of 7% 1,4,6-trimethylnaphthalene (1,4,6-TMN) and 5% N,N-dimethylaniline (DMA) in 88% isooctane was found to be the best system for laser-induced exciplex fluorescence (LIEF) visualization used to observe mixture formation in diesel or spark ignition engines. Observation of spectrally well separated fluorescence from a monomer in the gaseous phase and from exciplex in the gasoline fuel requires that the exciplex forming dopants have boiling points within the distillation range of gasoline (20°C to 210°C). Temperature-dependent measurements of the exciplex fluorescence have shown that the quenching mechanism leading to exciplex formation is sufficiently favorable to permit the exciplex to exist at temperatures approaching 150°C. These results suggest that the DMA•TMN exciplex system should be useful as a diagnostic for the visualization of gas and liquid distributions in flows.

3.2. Development & Characterization of new exciplex systems

3.2.1 Optical characterization

A. Sample preparation and apparatus

The TMN isomers were obtained in pure form and used as received. 1,4,5-TMN, 1,4,6-TMN were purchased from Carnegie-Mellon University. 2,3,6-TMN was purchased from Aldrich Chemical Company, as was DMA, DEA, and isooctane (2,2,4-trimethylpentane) of spectrophotometric grade. All chemicals are reported here on a weight basis. The normal boiling points[109] of 1,4,5-TMN, 1,4,6-TMN are 140-142°C and 145°C, respectively at low pressure, and the melting point of 2,3,6-TMN is 100-102°C, those of DMA and DEA are 193-194°C and 217°C, respectively.

Absorption spectra were measured on a Olis-modified Cary 17-spectrophotometer. Emission spectra were measured by a F-4500 Hitachi spectrofluorimeter or a high-resolution instrument in the Department of Chemistry.[110] The excitation wavelength was 308 nm and emission was recorded 300 nm to 550 nm at scan speeds of 240 nm/min. The excitation and emission bandpass were 5 or 10 nm. The PMT was a Hamamatsu R1104 or comparable tube with applied voltages ranging from 400 to 700 V.

B. Spectroscopy of the sample

The exciplexes employed in this study are formed from the complexes between dimethyl- or diethyl-substituted aniline (N,N-dimethylaniline (DMA) and N,N-diethylaniline (DEA)) with 1,4,5-, 1,4,6- or 2,3,6-trimethylnaphthalene (1,4,5-TMN, 1,4,6-TMN or 2,3,6-TMN, respectively). Figure 7 shows the absorption and emission spectra of the anilines. The absorption spectra of DMA and DEA are similar and characterized by a broad band with $\lambda_{abs,max}$ = 298 and 303 nm, respectively. Excitation in this absorption manifold (λ_{exc} = 308 nm) produces the intense fluorescence reproduced in Fig. 7. The absorption spectra of the TMNs, shown in Fig. 8, are typical of napthalenes. The broad bands feature progressions in the vibrations of the napthyl ring;[111] this vibrational progression is revealed by the sharp fine structure overlaid on the absorption profile. Many of the photophysical properties of the TMN isomers are not well known. Notwithstanding, the energy of the intense fluorescence is relatively invariant for the three isomers with $\lambda_{em,max}$ = 343, 342, and 339 nm for 1,4,5-TMN, 1,4,6-TMN and 2,3,6-TMN, respectively, upon excitation with wavelengths λ_{exc} < 330 nm. The 308-nm excitation line of a XeCl excimer laser is capable of producing either aniline or TMN excited states. Thus, the exciplex formed in the experiments results from the interaction of electronically excited TMN monomer with ground state aniline, or vice versa. The hydrocarbon fuel, isooctane, does not absorb at the XeCl excitation frequency as shown in Fig. 9, therefore, it is photophysically inert in these studies.

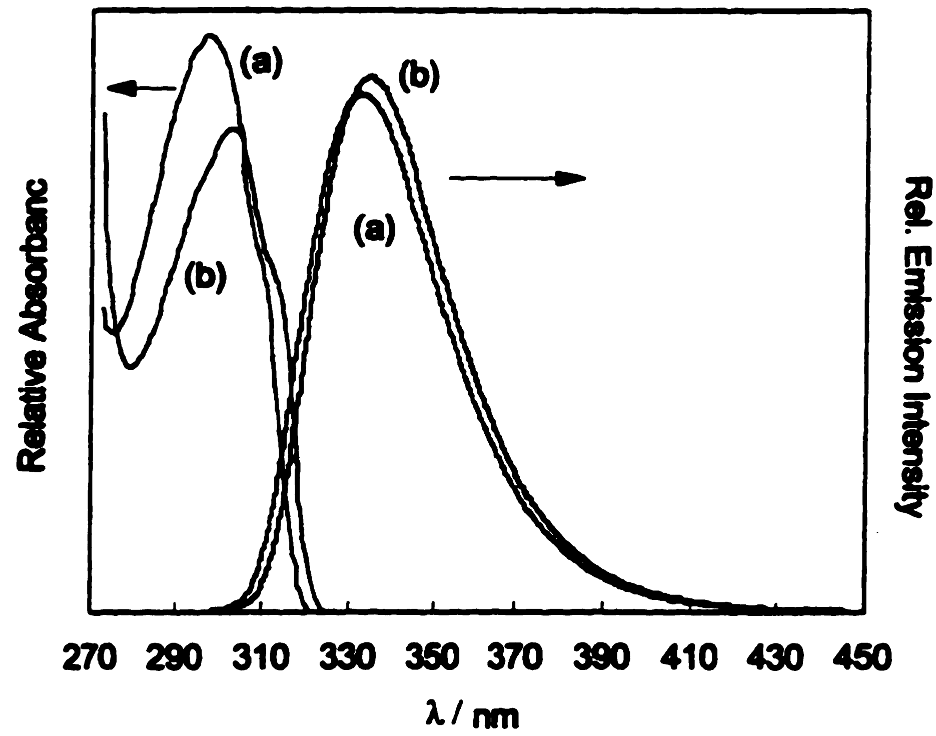

Figure 7. Absorption and emission spectra for (a) DMA and (b) DEA monomers in isooctane at room temperatures.

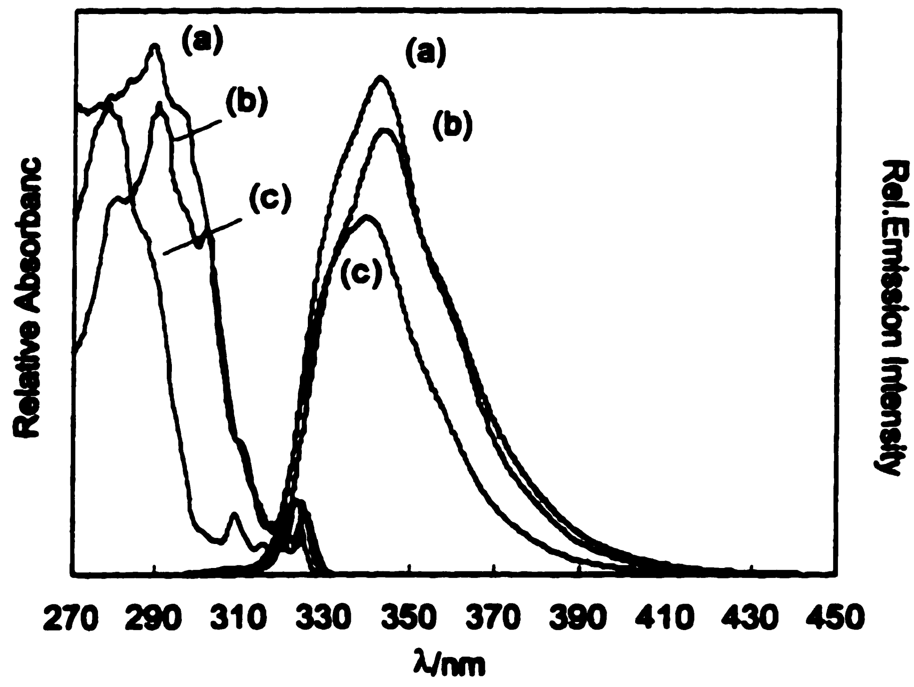

Figure 8. Absorption and emission spectra for trimethyl-naphthalenes (a) 1,4,6-TMN, (b) 1,4,5-TMN, and (c) 2,3,6-TMN in isooctane at room temperature.

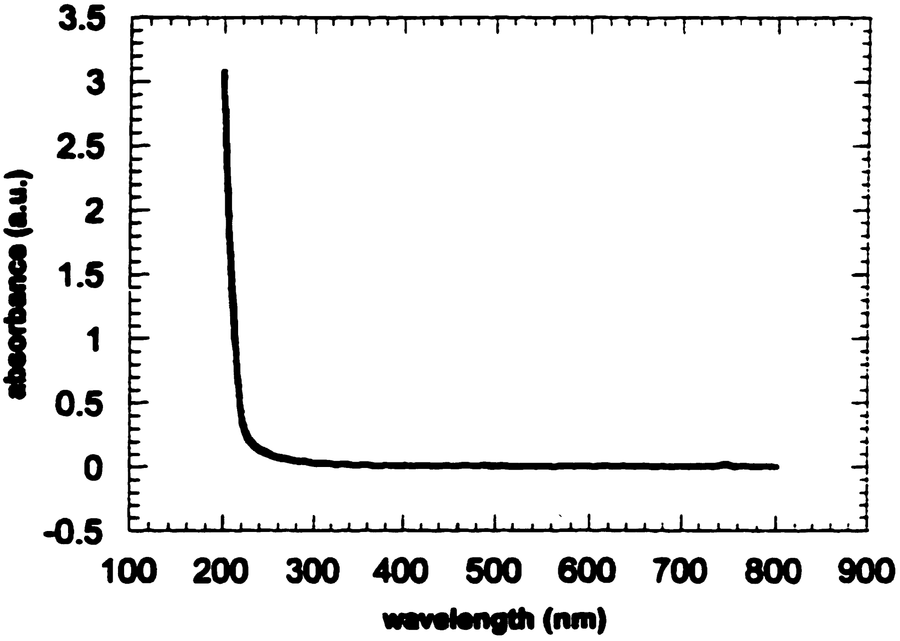

Figure 9. Absorption spectrum of the isooctane (2,2,4-trimethylpentane) solvent at room temperature.

C. Quantum yield of sample

In order to measure quantum yields of the DEA and TMN-isomers, such as 1,4,5-TMN, 1,4,6-TMN and 2,3,6-TMN, the absorption and emission spectra of these molecules were used. Figures 7 and 8 show those spectral results. All samples were prepared in an isooctane solvent. In this experiment all emission spectra were recorded from 300 nm to 550 nm with a F-4500 Hitachi spectro-fluorimeter. The excitation and emission bandpass was 10 nm.

The absolute fluorescence quantum yield (ϕ_{fl}) as a function of excitation wavelength (λ) is the ratio of the number of emitted fluorescence photons to the number of absorbed photons,[110]

$$\phi_{fl}(\lambda) = I_{fl}(\lambda) / I_{abs}(\lambda) \qquad (42)$$

where $I_{fl}(\lambda)$ is the photon intensity of fluorescence and $I_{abs}(\lambda)$ is the intensity of radiation absorbed. The absorbed photon intensity can be calculated from the Beer-Lambert law,

$$I_{abs}(\lambda) = I_0(\lambda)[1-10^{-\varepsilon cl}]$$

where $I_0(\lambda)$ is the incident photon intensity, $\varepsilon(\lambda)$ is the molar extinction coefficient ($M^{-1}cm^{-1}$), c is the molar concentration (M), and l is the optical path length of the sample (cm). Because numerous factors govern emission intensity the measurement of absolute quantum yield is difficult. These include variations in source intensity as a function of time, variations in the spectral response of the detector system as a function of wavelength, bandpass error, differences in collection efficiency of the collecting optics as a function of absorbance, and inner filter effects (reflections, polarization, and reabsoption-reemission effects).[107] Accordingly, relative intensity measurements are preferred and the quantum yield is typically obtained relative to the emission intensity of a known sample at a given excitation wavelength. The integrated area under the fluorescence emission spectrum is proportional to the total intensity of fluorescent light emitted by the solution, and this in turn is proportional to $I_0(\lambda)\varepsilon cl$. If the fluorescence emission spectra of two solutions are measured with the same apparatus under identical conditions, the ratio of the integrated fluorescence intensities[110] is given by,

$$\int f_S(\lambda)d\lambda \,/\, \int f_r(\lambda)d\lambda = D_S \,/\, D_r = A_S\phi_S \,/\, A_r\phi_r \tag{43}$$

where ϕ_S and ϕ_r are the quantum yields of the sample of interest and reference, respectively, and A_S and A_r are the respective optical densities defined by $\varepsilon_i c_i x_i$. The integrated intensities should be corrected for the spectral response of the detector system. However, when the emission wavelengths of the reference and sample are similar, as is the case here (the investigated monomer emission maxima are between 333 and 343 *nm*), this term can be neglected. In the measurements, quantum yields were referenced to DMA,[66] which has a known fluorescence quantum yield of 0.11 in cyclohexane. Because we wished to measure the quantum yields of our monomers in the isooctane hydrocarbon solvent, Eq. (43) needs to be corrected with a factor of $(n_r/n_s)^2$ to account for the different refractive indices of the sample and reference solvents.[66] Rearranging in terms of the sample quantum yield gives

$$\phi_s = \phi_r[A_r D_s n_s^2 / A_s D_r n_r^2] \qquad (44)$$

Since the absolute quantum yield of DMA in cyclohexane is known, the values of the other DEA and the TMNs are simply obtained from Eq. (44) (*n_r=1.426* for cyclohexane and *n_s=1.391* for isooctane). The fluorescence quantum yields of the monomers, measured for 308 nm excitation, are shown in Table 1. These high fluorescence yields are a direct quantitative measure of the intense fluorescence that characterizes these species.

Table 1. Relative Fluorescence Quantum Yield of Investigated Monomers

Monomer	$\lambda_{em,max}$/ nm	Quantum Yield (φ_{fl})
1,4,6-TMN[a]	342	0.065
1,4,5-TMN[a]	343	0.069
2,3,6-TMN[b]	339	0.071
DEA[a]	334	0.095
DMA[r]	333	0.11

The solute concentration used is; [a] 0.789μM, [b] 8.2×10^{-4} M and [r] referenced.[66]

3.2.2. Optical properties of exciplex formers

A. Room temperature measurements

A-1. Photophysics of DMA•TMN exciplex system

Molecules in an electronically excited state M* may be highly polarizable and can interact with other polar or polarizable species. An exciplex is produced when M* associates with a reacting partner Q to yield a complex (MQ)* more stable than the individual constituents M* or Q. If the excited state's reacting partner is a different molecule Q, then the excited state complex (MQ*) is called an exciplex.[106,112] A typical scheme for the overall exciplex process is depicted below.

$$\begin{tikzcd}
M^* + Q \arrow[rr, shift left, "K"] \arrow[dr] & & (MQ)^* \equiv E^* \arrow[ll, shift left] \arrow[dl] \\
& M + Q &
\end{tikzcd}$$

From an electronic structure perspective, the HOMOs of M and Q are filled and thus, there is no appreciable ground state interaction. Accordingly, the absence of an appreciable interaction between ground state M and Q excludes static quenching mechanisms of M*. However, excitation of one M* permits a bonding interaction to result from the interaction of the partially filled bonding and anti-bonding frontier orbitals of M* with the HOMO and LUMO, respectively, of Q as shown in Fig. 10. The consequences of these energetics are several-fold. The exciplex complex (MQ)* is stabilized with respect to M* and hence the fluorescence of the exciplex is red-shifted from that of M*. Moreover, (MQ) is unstable and therefore, the decay of the exciplex excited state returns the system to a dissociative ground state M + Q. Finally, the exciplex is formed at the expense of monomer by the direct reaction of the electronic

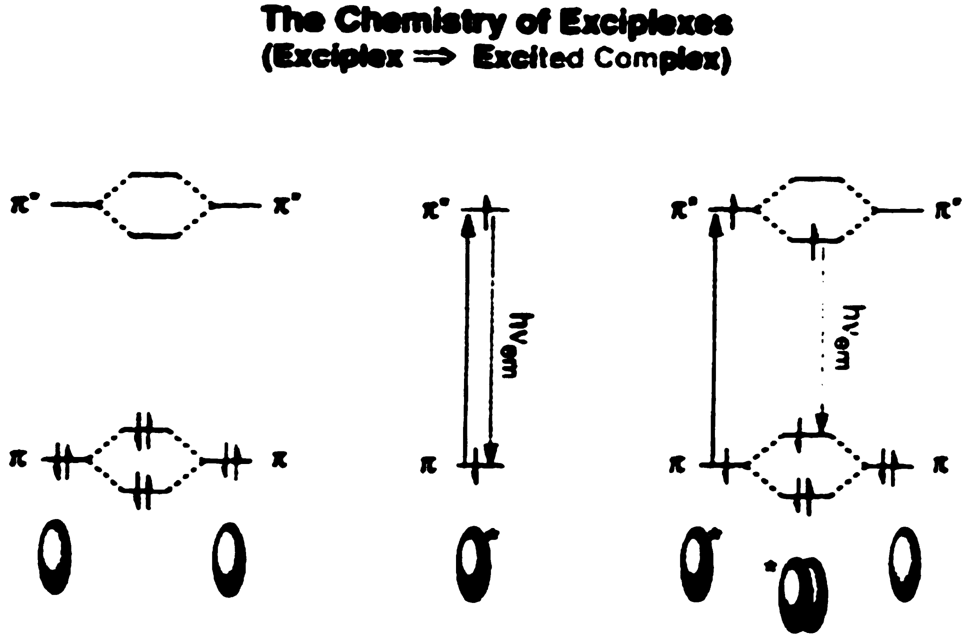

Figure 10. The photo-chemistry of DMA•1,4,6-TMN exciplex system.

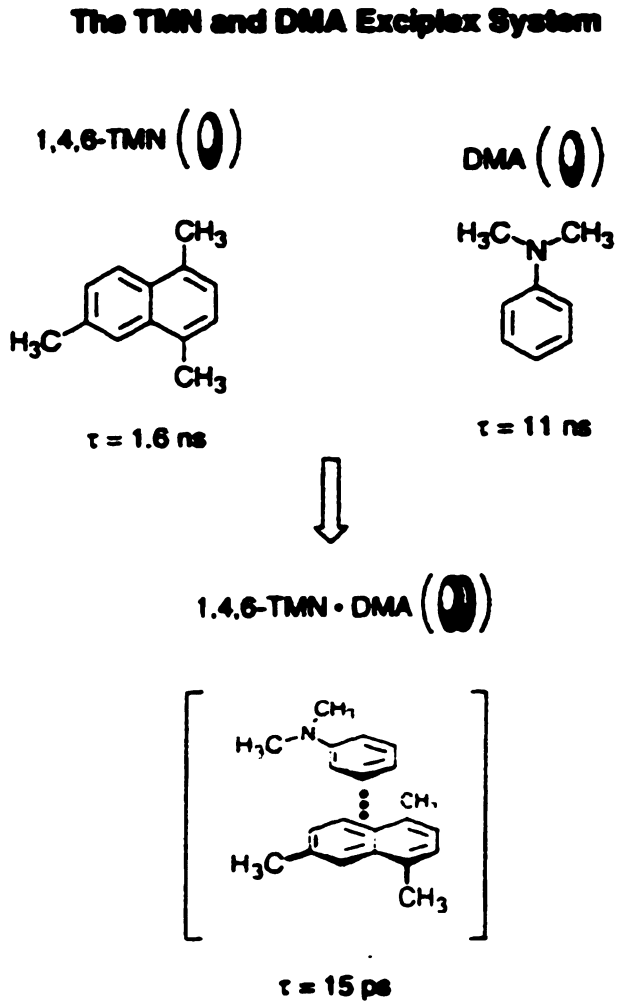

Figure 11. The ground-state configuration of the DMA•1,4,6-TMN exciplex system in isooctane solvent, at room temperature.

excited state with Q and quenching is thus a dynamic process depending directly on the concentration of Q. The chemical structures, as well as the photophysics of the ground state configuration of the exciplex formation of DMA and 1,4,6-TMN, are shown in Fig.11.

a. DMA•(2,3,6-TMN) exciplex system

In a series of experiments, either DMA or 2,3,6-TMN was used as a monomer or ground state reactant (quencher) to find out which configuration yields a better exciplex. In the DMA-(2,3,6-TMN) exciplex system, monomer (either DMA or 2,3,6-TMN) weight percentage was fixed at 5% and quencher molar concentration was increased from 0% to 10%. Figure 12 shows the fluorescence spectrum of 5% DMA monomer and its change upon adding 2,3,6-TMN in isooctane with 308 nm excitation. DMA monomer solution exhibits fluorescence quenching as the concentration of 2,3,6-TMN increases. Without a quencher, the wavelength corresponding to peak emission intensity of 5% DMA is 343 nm. As the molar concentration of the quencher increases, the DMA monomer fluorescence intensity at 343 nm was decreases greatly and a new, broad emission band was develops gradually with the maximum emission intensity around 401 nm. This new emission feature is due to exciplex formation between DMA and 2,3,6-TMN. Further increase above 10%(w) 2,3,6-TMN did not improve the exciplex emission. Figure 13 represents how the monomer and exciplex fluorescence intensity change with respect to 2,3,6-TMN concentration. The 5% monomer intensity at 343 nm

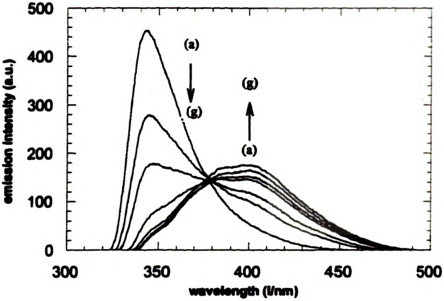

Figure 12. The fluorescence spectrum of 5% DMA and the fluorescence spectra upon the addition of 2,3,6-TMN in isooctane at weight ratios of (a) 0.1 %, (b) 0.5 %, (c) 1.0 %, (d) 3.0 %, (e) 5.0 %, (f) 7.0 % and (g) 10.0 %. The fluorescence intensities of monomer and exciplex are relative to each other.

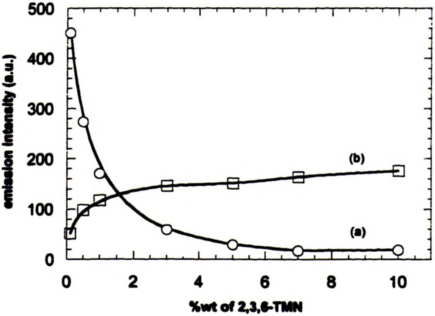

Figure 13. Fluorescence intensity changes of the 5% DMA (a) and the resulting exciplex upon the addition of 2,3,6-TMN in isooctane (b). (a): monomer intensity change at 343 (nm), (b): exciplex intensity change at 401 (nm), respectively.

decreases exponentially and new emission at 401 nm due to the exciplex increases logarithmically. The exciplex intensity dominates at values of 2,3,6-TMN concentration greater than 1.6%. Exciplex emission seems to be fully developed at 7% 2,3,6-TMN.

The experiment of Fig. 12 was then reversed. DMA was added as a quencher to an isooctane solution of a fixed weight percentage (5%) of 2,3,6-TMN monomer. Figure 14 shows the emission intensity of a 5% 2,3,6-TMN with respect to the concentration of DMA. Without a quencher, the wavelength at peak emission intensity of 5% 2,3,6-TMN was 347 nm. Similar to the 5% DMA•(x)%2,3,6-TMN exciplex system, the 2,3,6-TMN monomer fluorescence intensity decreases and a new broad emission band gradually develops around 400 nm when the DMA quencher molar concentration increases. This new emission feature is also due to exciplex formation between 2,3,6-TMN•DMA. Further increase above 7%(w) of the DMA concentration does not improve the exciplex emission. The intensity change of both the monomer and exciplex fluorescence at fixed wavelength is shown in Fig. 15.

There are two distinct differences between 5% DMA•(x)% 2,3,6-TMN and 5% 2,3,6-TMN•(x)% DMA exciplex systems. One is the difference in emission intensity, and the other is "cross-talk", the spectral wavelength separation (Δλ) between monomer and exciplex emission. At fixed concentration, the DMA•2,3,6-TMN exciplex system has higher emission intensities, for both monomer and exciplex relative to 2,3,6-TMN•DMA. The former exciplex system had a slightly larger spectral separation Δλ than the latter; 58 nm for the former, and 53 nm for the latter. These results are evidence that the DMA•2,3,6-TMN system has better exciplex formation than the 2,3,6-TMN•DMA system.

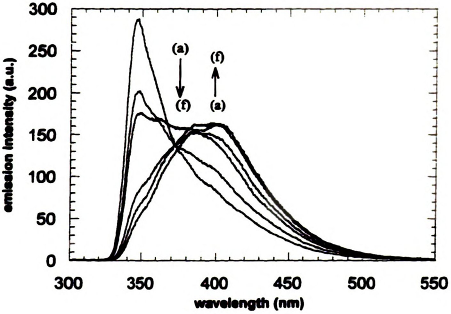

Figure 14. The fluorescence spectrum of 5% 2,3,6-TMN and the fluorescence spectra upon the addition of DMA in isooctane at weight ratios of (a) 0.1 %, (b) 0.5 %, (c) 1.0 %, (d) 3.0 %, (e) 5.0 % and (f) 7.0 %. The fluorescence intensities of monomer and exciplex are relative to each other.

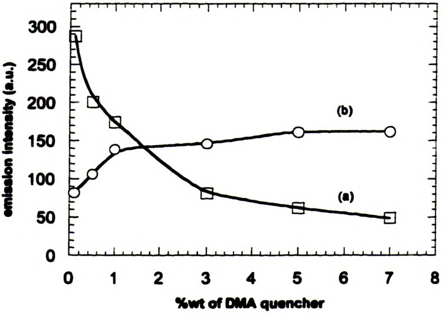

Figure 15. Fluorescence intensity changes of the 5% 2,3,6-TMN (a) and the resulting exciplex upon the addition of DMA in isooctane (b). (a): monomer intensity change at 347 (nm), (b): exciplex intensity change at 400 (nm), respectively.

b. DMA•(1,4,6-TMN) exciplex system

This section only concerns the 5% DMA•(x)% 1,4,6-TMN exciplex system since it is known that, at fixed concentration, the DMA•TMN system is a better exciplex former than TMN•DMA as explained above in Sec. a. Figure 16 shows the absorption and emission spectra of DMA and 1,4,6-TMN in isooctane. The absortion spectrum of the TMN is typical of naphthalene. Excitation in this absorption manifold ($\lambda_{exc} < 330$ nm) produces intense fluorescence ($\phi_e^{308} \sim 0.065$) with $\lambda_{em,max} \sim 342$ nm. The absorption spectrum of the exciplex forming counterpart, DMA, is characterized by a broad band with $\lambda_{abs,max} \sim 298$ nm; the compound fluoresces at a maximum of 334 nm with a quantum efficiency of 0.11. Figure 17 shows the evolution of the exciplex emission with the addition of 1,4,6-TMN to 5% DMA in isooctane at room temperature. The intense fluorescence of the DMA monomer is markedly affected by the addition of 1,4,6-TMN. The monomer emission is significantly reduced with the addition of its congener and a new, intense emission appears at lower energy, consistent with formation of a DMA•(1,4,6-TMN) exciplex. It was found that solutions with molar compositions of 5% DMA and 5% (to 7%) 1,4,6-TMN give the highest fluorescence yields of the exciplex. As the 1,4,6-TMN concentration increases, the 5% DMA monomer intensity at 343 nm is reduced greatly and a new exciplex emission at 405 nm develops. It is observed that the exciplex intensity is dominant at 1,4,6-TMN concentrations greater than 3%. By 7% 1,4,6-TMN, the exciplex emission seems to be fully developed. The intensity change of both of the monomer and exciplex fluorescence at fixed wavelength is shown in Fig. 18.

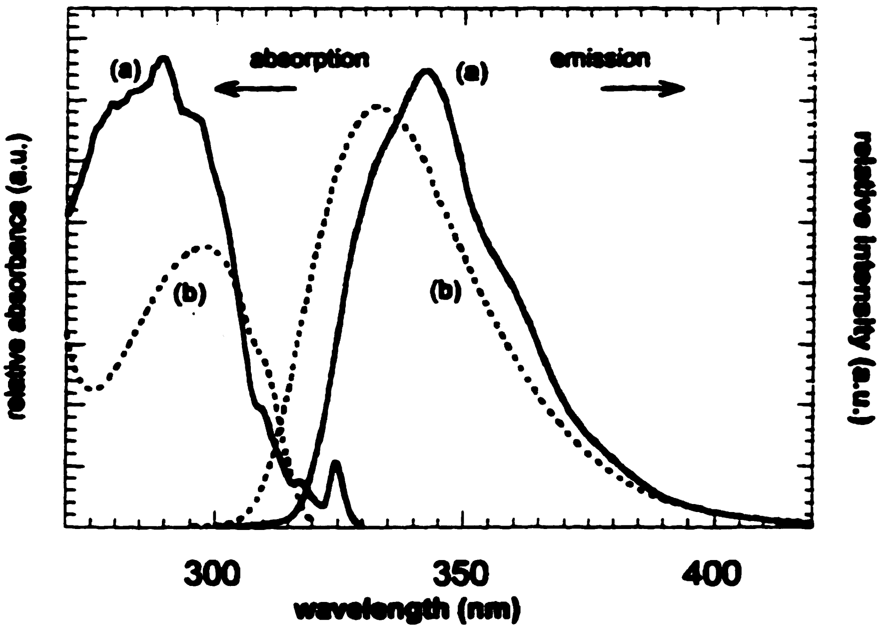

Figure 16. Absorption and emission spectra for (a) 1,4,6-TMN and (b) DMA monomers in isooctane (0.8 μM) at room temperature.

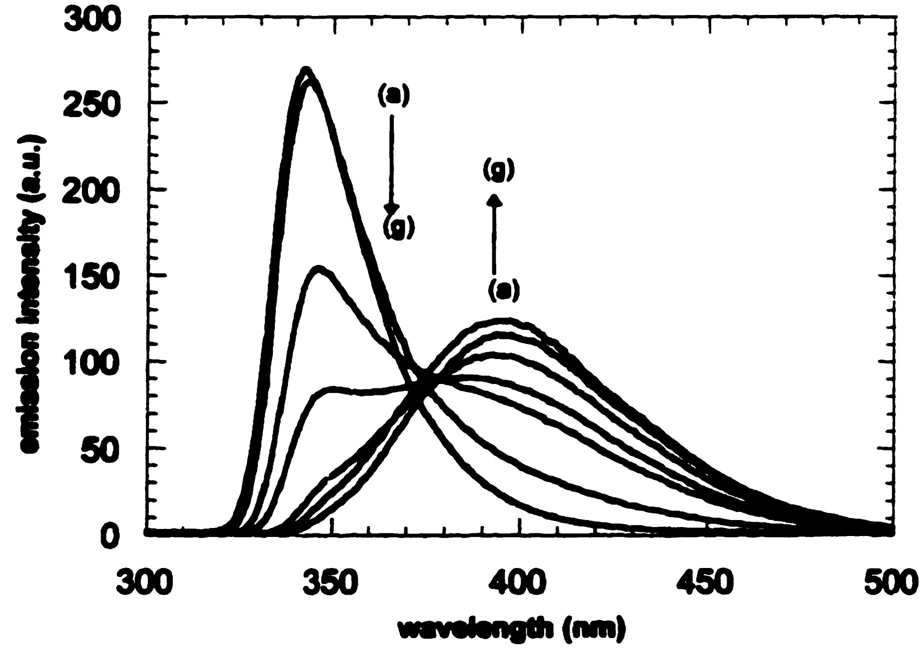

Figure 17. The fluorescence spectrum of 5% DMA and the fluorescence spectra upon the addition of 1,4,6-TMN in isooctane at weight ratios of (a) 0.1 %, (b) 0.5 %, (c) 1.0 %, (d) 3.0 %, (e) 5.0 %, (f) 7.0 % and (g) 10.0 %. The fluorescence intensities of monomer and exciplex are relative to each other.

Since ultraviolet excitation is capable of producing either DMA or TMN excited states, the fluorescence was monitored at 400 nm as the excitation wavelength was scanned to assess the dominant absorbing species that leads to exciplex formation. The excitation profile of the exciplex matches that of the TMN: $\lambda_{max,exc}$(1,4,6-TMN•DMA) = 340 nm; $\lambda_{max,exc}$(TMN) = 330 nm for isooctane solutions containing 5% DMA and 5% TMN. Exciplex emission is observed at wavelengths well into the near ultraviolet due to pronounced absorption at these high concentrations. It is probable that excitation of the DMA will also lead to exciplex formation. However, TMN is the stronger absorbing species in the UV at the high concentrations needed for exciplex formation (absorbance (A) = 4.12 at 388 nm for 5% TMN, whereas A = 1.41 at 388 nm for 5% DMA) thereby obscuring absorption by DMA. Finally, the attenuation of the excitation profile at higher wavelengths, well below the absorption maximum of TMN, is also due to the high absorptivities of solutions at λ_{exc} > 388 nm. For these wavelengths, all the absorption occurs at the front face of the cell, out of the line of sight of the detection optics of the instrument.

c. General discussion of exciplex results

The intense fluorescence of the TMN monomers is markedly affected by the addition of the substituted anilines; similarly, DMA or DEA fluorescence is altered significantly in the presence of the TMNs. For either situation, the monomer emission is significantly reduced with the addition of its congener and a new, intense emission appears at lower energy, consistent with the formation of a DMA•TMN exciplex. It is found that solutions at compositions of 5% DMA and 7% TMN give the highest

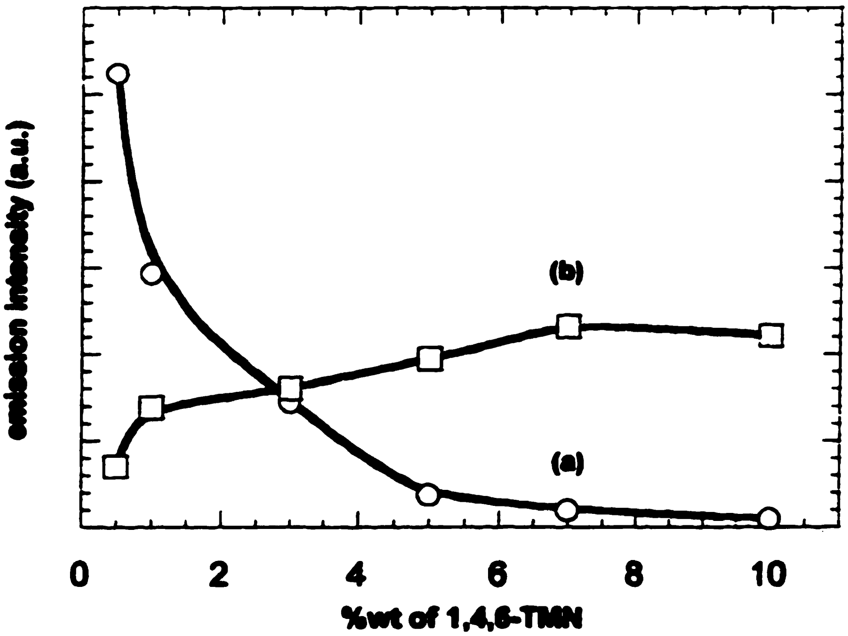

Figure 18. Fluorescence intensity changes of the 5% DMA (a) and the resulting exciplex upon the addition of 1,4,6-TMN in isooctane (b). (a): monomer intensity change at 343 (nm), (b): exciplex intensity change at 405 (nm), respectively.

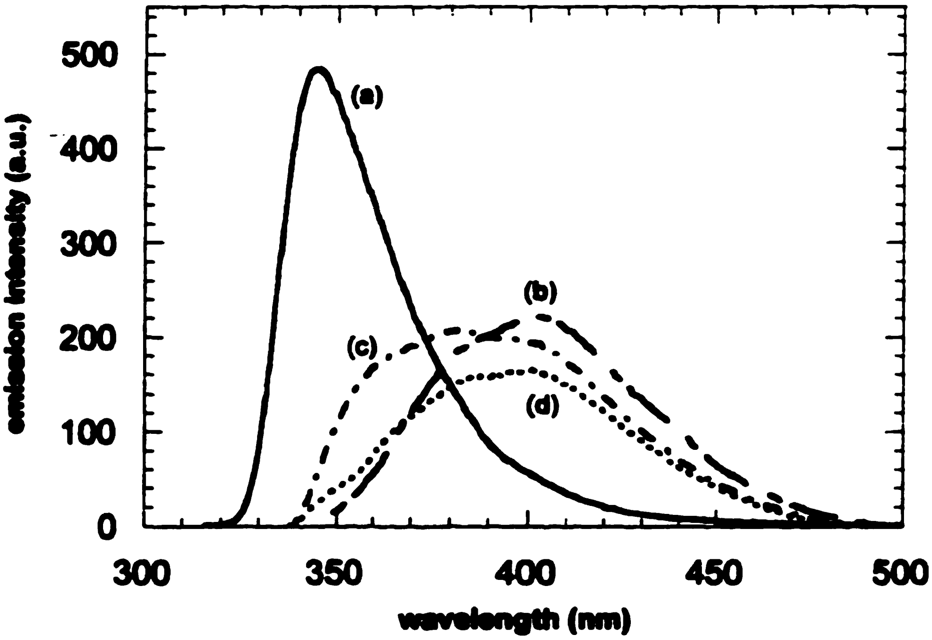

Figure 19. Fluorescence spectra of (a) 5% DMA and the resulting exciplex fluorescence spectra upon the addition of (b) 7% 1,4,6-TMN, (c) 7% 1,4,5-TMN and (d) 7% 2,3,6-TMN in isooctane. Relative spectral intensities are presented.

fluorescence yields of the exciplex. Moreover, as observed from the relative spectral profiles of Fig. 19, the DMA•1,4,6-TMN exciplex system has the higher fluorescence peak emission intensity and larger spectral separation (Δλ) between monomer and exciplex. The wavelength at the peak exciplex emission intensity is 405 nm for 7% 1,4,6-TMN, 401 nm for 7% 2,3,6-TMN and 382 nm for 7% 1,4,5-TMN, respectively. In order to assess whether DMA or DEA is the better exciplex forming constituent with the TMN system, the experiment of Fig. 19 was reversed and aniline added to an isooctane solution of a fixed concentration of 1,4,6-TMN. Figure 20 shows the results for the addition of 5% DMA and DEA to 5% solutions of 1,4,6-TMN. As observed in the complementary experiment described above, the intense fluorescence of the monomer, in this case TMN (λ_{max} = 350 nm), is attenuated efficiently in the presence of the aniline with the concomitant growth of a low energy exciplex fluorescence (λ_{max} = 402, 400 nm for DMA and DEA, respectively). As is evident from the relative exciplex fluorescence intensities, DMA forms a slightly more stable exciplex (higher intensity) and better spectral resolution (Δλ) is observed with regard to the monomer emission. The same result was obtained for the 2,3,6-TMN and its exciplex congeners (i.e., 5% DMA or DEA) shown at Fig. 21. These results are consistent with exciplex formation as a result of the donor (DMA)-acceptor (TMN) interaction between proximately disposed constituents. Because the DEA has more carbons on the aniline (diethyl versus dimethyl of DMA), it is sterically more bulky than DMA, and thus it more weakly associates with the TMN monomer, thereby accounting for the slightly weaker and blue-shifted emission

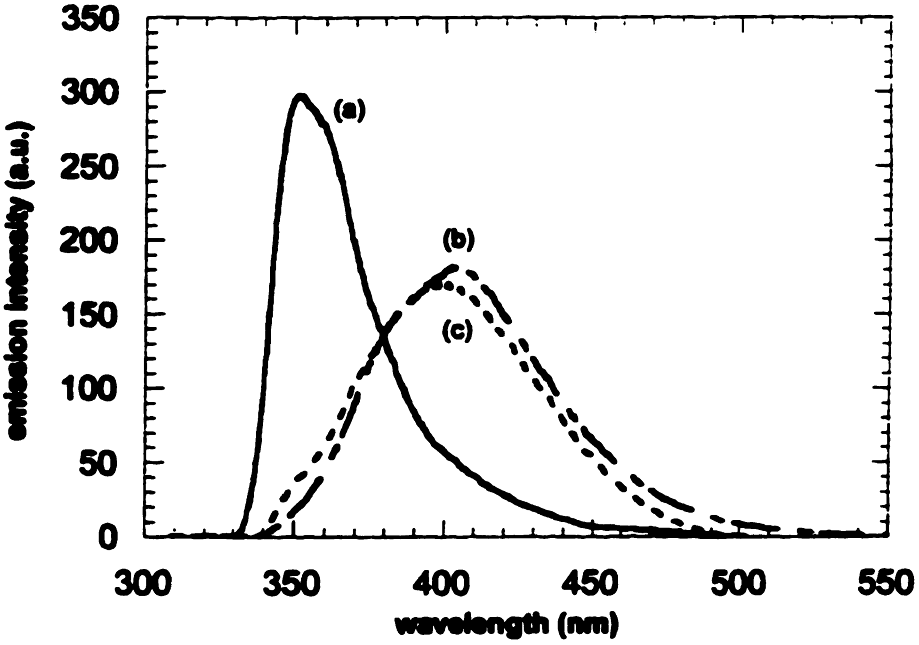

Figure 20. Fluorescence spectra of (a) 5% 1,4,6-TMN and the resulting exciplex fluorescence spectra upon the addition of (b) 5% DMA, (c) 5% DEA in isooctane. Relative spectral intensities are presented.

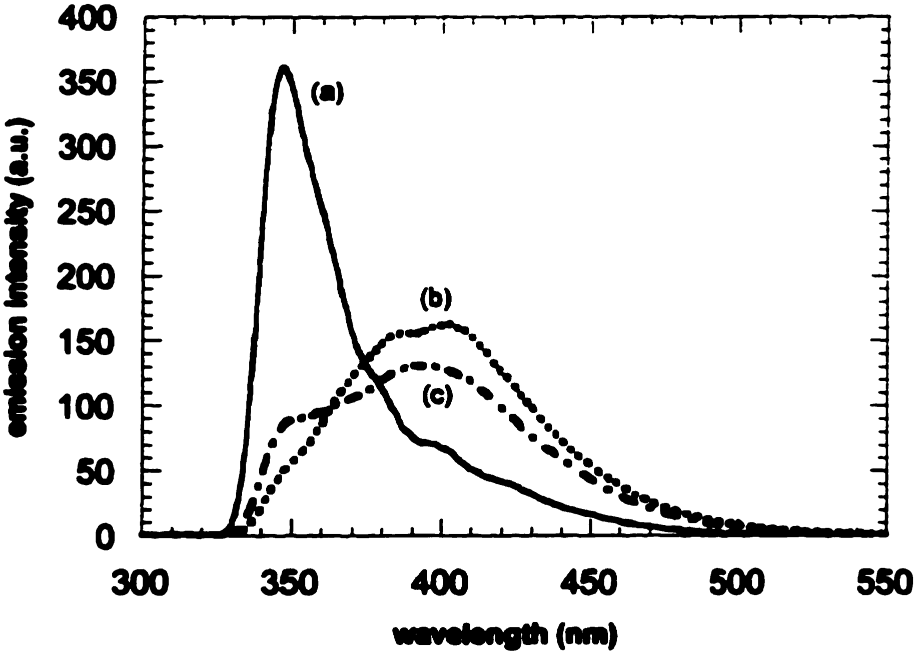

Figure 21. Fluorescence spectra of (a) 5% 2,3,6-TMN and the resulting exciplex fluorescence spectra upon the addition of (b) 5% DMA, (c) 5% DEA in isooctane. Relative spectral intensities are presented.

Table 2. Monomer and Exciplex Emission Wavelength of the Investigated Exciplex Systems.

Exciplex Systems (% wt)	Monomer Peak Emission Wavelength ($\lambda_{max,m}$)	Exciplex Peak Emission Wavelength ($\lambda_{max,e}$)
5% DMA•7% 1,4,5-TMN[a]	343	382
5% DMA•7% 1,4,6-TMN[a]	343	405
5% DMA•7% 2,3,6-TMN[a]	343	401
5% 1,4,6-TMN•5% DMA[b]	350	402
5% 1,4,6-TMN•5% DEA[b]	350	400

DMA: N,N-Dimethylaniline, DEA: N,N-Diethylaniline, TMN: Trimethylnaphthalene. The % wt for the isooctane solvent is [a] 88% and [b] 90%, respectively.

of the TMN•DEA exciplex complex. The emission wavelengths of monomers and exciplexes investigated are shown in Table 2.

A-2. Exciplex quenching analysis

The excited state monomer reacts with its exciplex forming partner in one of two possible ways. In terms of a DMA excited state, the two reaction pathways are

$$DMA^* + TMN \rightarrow DMA + TMN \quad \text{(dynamic quenching)} \qquad (45)$$

$$DMA^* + TMN \overset{K}{\rightleftharpoons} [DMA + TMN]^* \quad \text{(static quenching)} \qquad (46)$$

For Eq. (45), the excited state monomer reacts with its partner in a bimolecular reaction, and the excited state is said to be quenched dynamically.[113] Alternatively, as described by Eq. (46), the excited state monomer may react by its association to form an exciplex (called static quenching). For both the dynamic and static quenching pathways, the excited state concentration of monomer is diminished, therefore, the monomer fluorescence is effectively attenuated or quenched with increasing concentration of its exciplex-forming partner. The quenching processes are quantitatively described by a modified Stern-Volmer treatment[113]

$$I_0/I = (1 + K_{sv}[TMN])(1 + K[TMN]) \qquad (47)$$

where the ratio of the intensities of DMA fluorescence in the absence and presence of TMN, (I_0/I), is related to the concentration of a quencher via the Stern-Volmer constant, K_{sv}, and an equilibrium constant K. The Stern-Volmer constant is the product of the quenching rate constant and the natural lifetime ($K_{sv} = k_q\tau_o$). It therefore describes the dynamic quenching of DMA* by TMN (i.e. Eq. 45). The overall quenching reaction is augmented by the association of DMA* and TMN as described by the equilibrium constant K for Eq. (46). If both static and dynamic quenching processes are operative, Eq. (47) predicts an upward curvature of the plot of I_0/I versus [TMN]. Conversely, if quenching occurs by only one mechanism ($K_{sv} = 0$ in the case of static quenching and K= 0 for dynamic quenching), then Eq. (47) reduces to the form

$$I_0/I = 1 + K'[TMN] \qquad (48)$$

to give a linear relation between I_0/I and [TMN] with an intercept of unity and a slope of K'; for the dynamic quenching $K' = K_{sv}$ and for the static quenching case K' = K.

a. DMA•(2,3,6-TMN) exciplex system

Figure 22(a) plots I_0/I ratios obtained from the various DMA emission bands of Fig. 12 versus 2,3,6-TMN concentration. The plot follows a square law and the upward curvature is a clear indication that the exciplex quenching mechanism contains both static and dynamic contributions. A fit of Eq. (47) to these data yields coefficients $k_1 = 37.6 M^{-1}$ and $k_2 = 2.7 M^{-1}$. The natural lifetime of DMA in nonpolar solvents such as isooctane is 2.4 ns.[114] If it is assumed that the dynamic quenching rate constant is diffusionally controlled ($k_q \approx 10^9 M^{-1} s^{-1}$), which is reasonable for an exciplex system, then K_{SV} is calculated to be 2.4 M^{-1}, which is in good agreement with the smaller constant k_2 obtained from the fit of Eq. (47), and thus identifies it as the dynamic component of the quenching process. Accordingly, the equilibrium constant for exciplex formation was $K = 37.6 M^{-1}$, therefore, the DMA quenching mechanism was dominated by exciplex formation. This result is entirely consistent with the appearance of bright exciplex fluorescence with increasing quenching of monomer fluorescence in these systems. If this were not the case, then the DMA fluorescence would be quenched with no observation of a red-shifted emission. Figure 22(b) shows a 5% (2,3,6-TMN) monomer quenching feature with the addition of DMA in isooctane. In contrast to the results above, a plot of the intensity ratio (I_0/I) is linear in the DMA concentration. This clearly means that only one of the static or dynamic quenching processes is operative in this system. A fit of Eq. (48) to these data yields a value for $K' = 22 M^{-1}$. It is believed that this system can be explained with the static quenching process only, otherwise 2,3,6-TMN fluorescence would be quenched with no observation of a bright red-shifted emission.

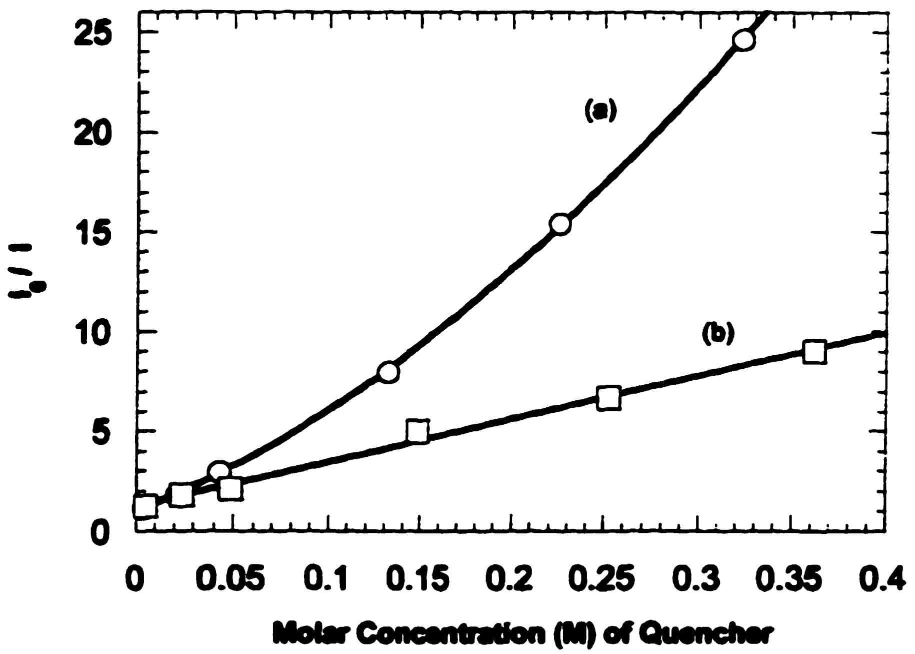

Figure 22. A modified Stern-Volmer plot with respect to the molar concentration of the quencher; (a) 2,3,6-TMN, (b) DMA quencher, respectively. The solid line is a fit of Eq. (47) and (48) to these data.

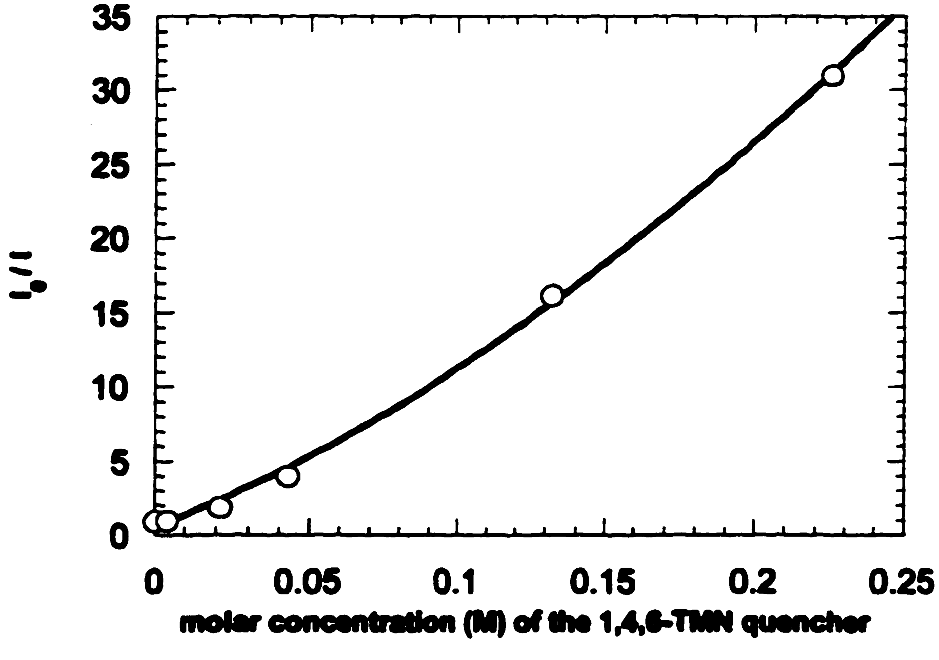

Figure 23. A plot of the I_0/I data of Fig. 17 versus the concentration of 1,4,6-TMN in isooctane solvent. The solid line is a fit of the modified Stern-Volmer Eq. (47) to these data.

b. DMA•(1,4,6-TMN) Exciplex System

Figure 23 plots I_0/I ratios obtained from the various DMA emission bands of Fig.17 versus 1,4,6-TMN quencher concentrations [1,4,6-TMN]. The plot follows a square law and the upward curvature indicates static and dynamic quenching. A fit of Eq. (47) to these data yields constants of 70.1 M^{-1} and 3.8 M^{-1}. The natural lifetime of DMA in nonpolar solvent, such as isooctane, is 2.4 ns. Again, if it is assumed that the dynamic quenching rate constant is diffusionally controlled ($k_q \approx 10^9$ $M^{-1}s^{-1}$) which is reasonable for an exciplex system, then K_{sv} is calculated to be 2.4 M^{-1}, which is in good agreement with the smaller constant obtained from the fit of Eq. (47). An equilibrium constant of K = 70.1 M^{-1} suggests that the DMA quenching mechanism is dominated by exciplex formation. This result is also entirely consistent with the appearance of bright exciplex fluorescence with increasing quenching of monomer fluorescence in these systems. If this were not the case, then DMA fluorescence would be quenched with no observation of a red-shifted emission. Among the investigated DMA•TMN exciplex systems, the DMA•1,4,6-TMN system has the highest equilibrium constant (K), meaning that it is a stable and produces better exciplex formation as indicated by previous results.

A-3. Fluorescence lifetime measurements

Lifetimes of DMA and the DMA•1,4,6-TMN exciplex were determined by time-correlated single photon counting with an instrument in the LASER Laboratory. The time-correlated photon counting set-up was modified from a previous configuration[115] in order to decrease the transit time spread of monochromator, and consequently improve the overall instrument response function. The SPEX 1681 monochromator was replaced with a subtractive double monochromator from CVI Laser, thereby eliminating the use of a 10 mm mask on the diffraction grating. The 220 ps risetime of the detector was improved to 156 ps by replacing the 12 μm R1564U/11 MPC-PMT (Hamamatsu) with a 6 μm R3809U MPC-PMT (Hamamatsu). The shortening of the detector's risetime necessitated a concomitant shortening of the 9 cm internal delay loop of the fluorescence channel of the CFD (Tennelec CFD 454). Finally, a TAC biased amplifier (Oxford Instruments Model TC 864) replaced the TC 862, changing the range of the smallest temporal window from 25 to 5 ns. The excitation wavelength used to measure the lifetime of DMA monomer and DMA•(1,4,6-TMN) exciplex was 308 nm, obtained by doubling the R6G dye output of a Coherent Model 702 Dye laser pumped by a mode-locked Nd:YAG (Coherent Model 76S). The emission was monitored at 390 nm. For highly absorbing samples (> 5% DMA•1.4.6-TMN concentrations), emission was collected at the front face of the cuvette with a microscope objective (Ealing, 25-0522) directed through a polarization scrambler (CVI DPL-10-450.0-700.00), and focused onto the monochromator slit.

Lifetime measurements of isooctane solutions of DMA and 1,4,6-TMN parallel the results of the steady-state fluorescence experiments. Figure 24 shows a typical plot of the lifetimes of monomer fluorescence of 5% DMA and the exciplex emissions as the concentration of 1,4,6-TMN is increased to a 5% molar concentration. Throughout the lifetime measurement, DMA monomer concentration was held constant at 5% in the isooctane solutions. The emission decay (λ_{det} = 390 nm) exhibited an exponential decrease in the absence of TMN with the value of τ = 1.59 ns. With increasing concentrations of 1,4,6-TMN, a biexponential decay was observed, with the DMA component of the lifetime shortening as would be expected for a dynamic quenching process. The temporal decay of the long lifetime component remains almost invariant (τ = 11.0 ± 1.5 ns) with increasing 1,4,6-TMN molar concentration, but its relative contribution to the overall decay process increases. These results are consistent with the formation of an exciplex. Since the exciplex decays by unimolecular dissociation as described on p. 52 (summarized in Table 3), its lifetime should be invariant with 1,4,6-TMN concentration.

B. High temperature measurements

The main interest in developing these exciplex systems is to visualize gas-liquid distributions in flow vaporization applications. Since we are especially interested in automotive gasoline engines, this has led us to begin investigating the fluorescence quenching process of exciplex systems at elevated temperatures. A "good" exciplex system at room-temperature does not guarantee that it will be "good" at elevated temperature environments, e.g., under operating engine conditions. Most exciplex emissions are quenched at high temperature due to the thermally activated process called "thermal quenching".[116] For the DMA•TMN system to be useful for visualizing gas-liquid distributions in engines, it must produce a favorable exciplex emission at high temperatures.

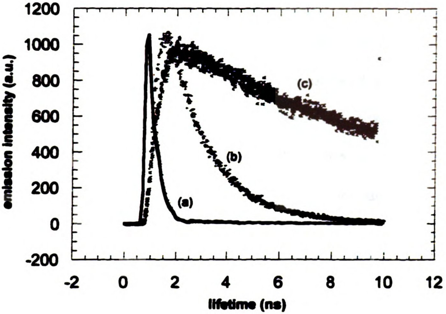

Figure 24. Time-resolved emission fluorescence spectroscopy of (a) instrument rise-time response, (b) 5% DMA monomer and (c) 5% DMA•5% (1,4,6-TMN) exciplex in isooctane solvent.

Table 3. Picosecond fluorescence lifetimes of 5% (wt) DMA and DMA•1,4,6-TMN exciplex as the wt % of 1,4,6-TMN is varied[a]

wt % of 1,4,6-TMN	Molar Concentration (M)	$\tau(DMA)/ns$	$\tau(DMA \bullet TMN)/ns$
0.00	0	1.59	-
0.10	0.004288	1.44	13.1
0.50	0.021614	0.92	-
1.00	0.042934	0.423	9.54
3.00	0.132327	0.18	-
5.00	0.225772	0.165	11.1
7.00	0.323388	0.142	10.3

[a] The solvent was isooctane and the temperature was maintained at 28 (± 0.5)°C. The lifetimes were detected at $\lambda_{det} = 390$ nm.

B-1. Sample preparation and apparatus

Temperature-dependent fluorescence measurements over a range from 20-200°C were performed with an apparatus consisting of a Pyrex round bottom and 1 cm quartz cuvette. The design of the cell permitted the exciplex to be prepared under high vacuum conditions, thereby precluding oxygen as a possible quenching source in photophysical measurements of monomer and exciplex fluorescence. Liquids added to the round bottom were thoroughly degassed by standard freeze-pump-thaw procedures; the round bottom was evacuated via a Kontes quick-release Teflon valve. The liquid sample was vacuum transferred to the cuvette and isolated by sealing a second Kontes quick-release Teflon valve between the two chambers. The cuvette portion of the cell could be detached from the round bottom so that it could easily be introduced into a high temperature apparatus, shown in Fig. 25, which was designed to permit temperature control of the fluorescence cuvette during spectroscopic measurements. The sample chamber was a rectangular aluminum block comprising upper and lower sections. A square slot in the lower aluminum block served as a sample holder, which was enclosed by the upper block. Openings on three sides of the lower block permitted absorption or right-angle fluorescence measurements to be performed. The aluminum block was heated by two sets of 75 W cartridge heaters, and their temperature were monitored with a thermocouple (Type J, Omega Model 199). The aluminum blocks were well insulated with machinable solid aluminum silicate ceramics. The cuvette could be translated vertically by 2.5 cm to position either the liquid or vapor phase regions of the cuvette on the optic axis. Temperature-dependent exciplex emission spectra was measured on either a F-4500 Hitachi spectrofluorimeter or a high resolution instrument.[110] For the latter, the excitation wavelength was 308 nm and emission was recorded over a 300-500 nm range at a scan speed of 240 nm/min with a Hamamatsu R1104 PMT as the detector. The excitation and emission bandpass were 5 or 10 nm.

B-2. Temperature-dependent fluorescence quenching

Exciplex formation between DMA and 1,4,6-TMN was preserved at elevated temperatures. Figure 26 shows the temperature-dependent exciplex fluorescence spectra of 5% DMA•5% 1,4,6-TMN solutions of isooctane at 28°C to 150°C. The significant blue-shift of the fluorescence profile with increasing temperature indicates that exciplex formation is dramatically attenuated. A shift of the equilibrium from exciplex to monomer is expected on the basis of entropic considerations. More quantitatively, if one assumes that the exciplex emission intensity is proportional to the concentration of exciplex, then the integrated intensity of the exciplex emission band provides the temperature-dependent equilibrium constants, and hence free energy for formation of the exciplex relative to K = 70.1 M^{-1} at 28°C.

The expression for the temperature-dependent equilibrium constant K(T), is given by:

$$K(T) = \frac{[E^*]}{[M^*][Q]} = \exp[-\Delta G / RT] = \exp[-(\Delta H - T\Delta S) / RT]$$

$$\ln[K(T)] = \frac{-(\Delta H - T\Delta S)}{RT} = \frac{\Delta S}{R} - \frac{\Delta H}{RT} \qquad (48)$$

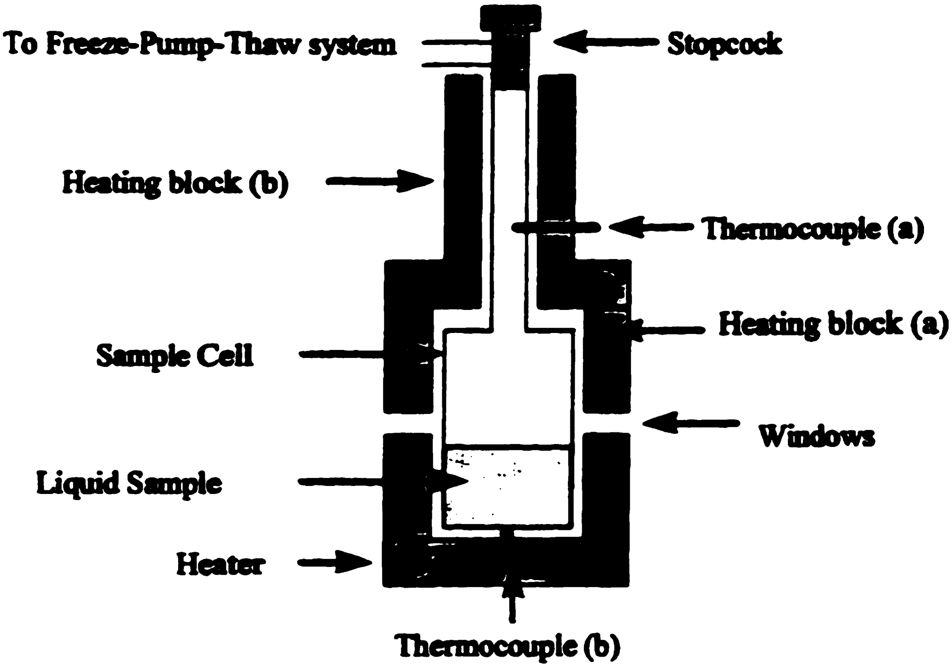

Figure 25. The heating chamber for high temperature exciplex fluorescence measurements

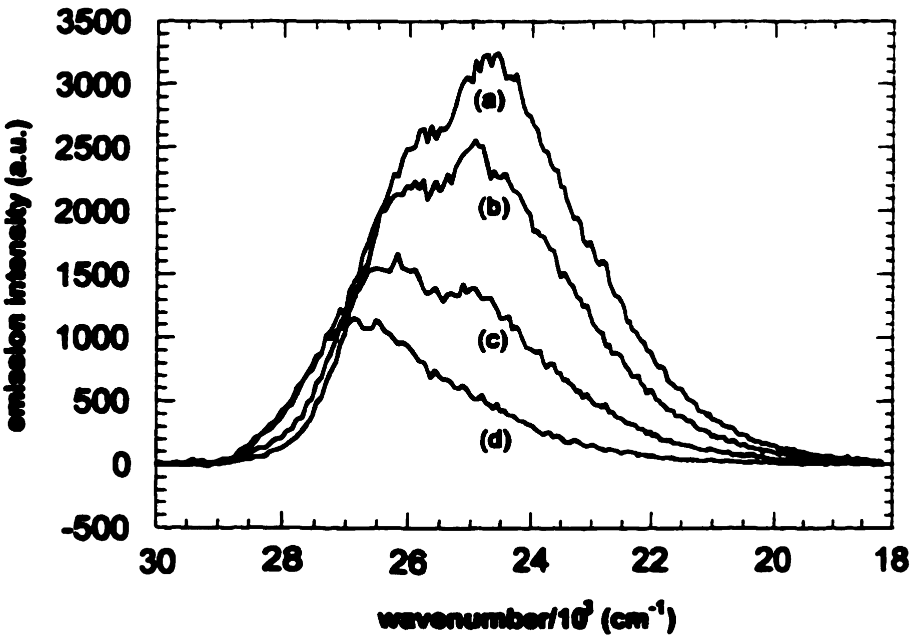

Figure 26. Fluorescence spectra of isooctane solutions of DMA•1,4,6-TMN (5% w:w) at (a) 28°C, (b) 60°C, (c) 100°C and (d) 150°C. The fluorescence spectral intensities are relative to each other.

where [E*] is the molar concentration of the exciplex-pair molecules in [DMA•1,4,6-TMN]. [M*] and [Q] are the monomer (DMA) and quencher (1,4,6-TMN) molar concentration, respectively. ΔG is the Gibbs free energy, ΔH the enthalpy, and ΔS the entropy of the system.

In fact, the temperature-dependent exciplex emission is the contribution from the pure exciplex and the monomer fluorescence. In order to find out the pure exciplex contribution only, the integrated emission intensity of the exciplex was determined from a Gaussian band-shape analysis of the spectra as shown in Fig. 26. In this analysis, the pure exciplex emission was entirely separated from the pure monomer emission. Two different central wavelengths for the Gaussian band shape were employed; 25×10^3 cm^{-1} and 27×10^3 cm^{-1} for the exciplex and monomer emission, respectively. As temperature increased, the integrated intensity of pure exciplex decreased relative to the pure monomer emission. The initial molar concentrations of DMA and 1,4,6-TMN used in the 5% DMA•5% (1,4,6-TMN) exciplex system were 0.3173 [M] and 0.2258 [M], respectively. Using these values with the room temperature (28°C) equilibrium constant ($K = 70.1 M^{-1}$), the exciplex concentration could be obtained with the value of 0.2189 [M] in room temperature. Assuming that the integrated exciplex intensity is proportional to the concentration directly, then the temperature-dependent equilibrium constant relative to K = 70.1 M^{-1} at 28°C can be calculated and recorded in Table 4 as a function of temperature. In order to obtain enthalpy (ΔH) and entropy (ΔS) of the system, The values of $\ln(K(T))$ were fitted using Eq. (48). The van't Hoff plot of these data shown in Fig. 27 yields ΔH =-16.9 kcal/mol and ΔS = -47.9 eu. It should be noted that calculated

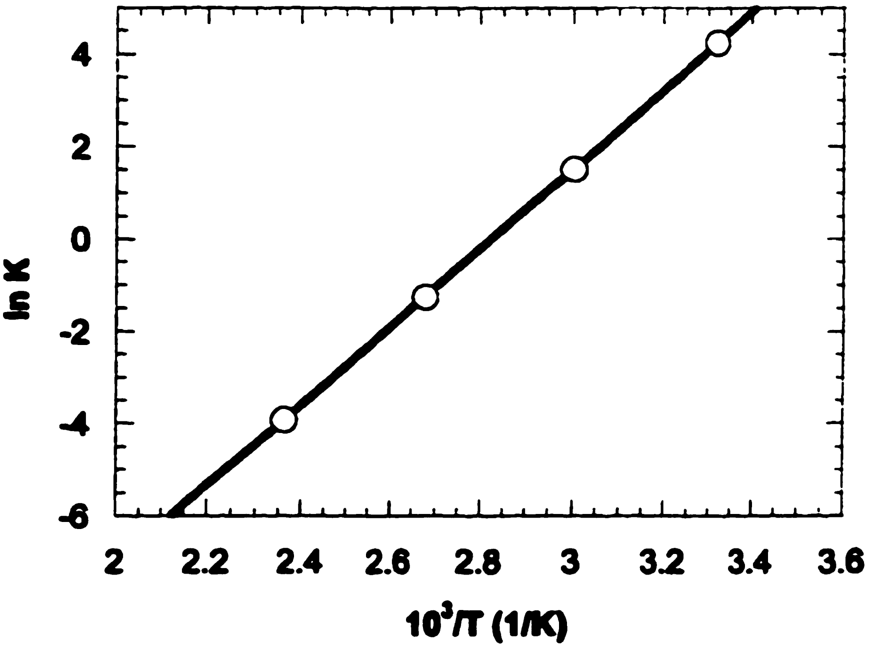

Figure 27. Van't Hoff plot of equilibrium constant for exciplex 5% DMA•5% (1,4,6-TMN) formation. The exciplex concentrations were determined from the integrated intensity of the deconvoluted exciplex fluorescence bands of Fig. 26.

Table 4. Temperature-dependent equilibrium constant K(T)

Temperature (K)	Exciplex-pairs (M2)	Equilibrium Constant (M^{-1})	Area of the exciplex fluorescence(×10^6)
301.1	0.219	70.1	12.11
333.1	0.177	4.63	9.81
373.1	0.093	0.29	5.14
423.1	0.033	0.02	1.84

enthalpy and entropy values are upper limits. The assumption that the exciplex fluorescence was proportional to concentration may not be justified since the temperature dependence of non-radiative decay paths of the exciplex has been ignored.[117] However, the negative entropy of formation is consistent with dimerization of monomers. Moreover, the enthalpy of formation is in line with that observed for other exciplexs of naphthalene (typically between 10-20 kcal/mol),[67,118] and the entropy of activation, though large, is consistent with that observed for some aromatic exciplexes.[119] The smaller value here probably results from the presence of three methyl groups on the naphthalene ring. These moieties provide a barrier to exciplex formation by sterically hindering the cofacial arrangement of the DMA and 1,4,6-TMN π-aromatic rings, which is the preferred geometry for exciplex formation. The results presented here indicates that the temperature-dependent measurements of the exciplex fluorescence indicate that the quenching mechanism leading to the formation of the exciplex is sufficiently favorable to permit the exciplex to exist at temperatures approaching 150°C.

3.3. Application of exciplex fluorescence to thermometry

The liquid phase temperature in the fuel sprays is one of the most important factors affecting the spray development, mixture formation and combustion processes. In a gas turbine or a automotive engine, fuel spray injected into a hot gas atmosphere evaporates by heat transfer from the surrounding air. Fuel vaporization, fuel/air mixing, ignition delay, and the position of the ignition start in fuel spray affect the spray combustion characteristics and the exhaust emissions significantly, and are functions of the liquid phase temperature in the fuel sprays.[120] In order to understand the spray combustion process, investigating the temperature distribution of the liquid phase is important. However, non-intrusive and highly space and time-resolved measurements of the liquid phase temperature in fuel sprays have not been measured for gasoline-based fuel. The measurement of the temperature within a dynamic spray environment is difficult. Thermocouples provide point measurements but may distort the local flows significantly. Laser light scattering techniques, such as those used in the forward scattering (Malvern) and phase doppler instruments,[121] have provided significant information on droplet number densities, size distributions, and velocity distributions, but have been virtually insensitive to droplet temperature. Recent modifications to the phase doppler techniques ("rainbow scattering") may lead to temperature information,[122] but these techniques will remain fundamentally point or line-of-sight techniques. Fluorescence methods, as described in this section, offer the possibility of minimally perturbing, real-time, two-dimensional measurements of temperature within droplets or sprays. A significant weakness of the fluorescence method is their sensitivity to the environment, particularly to quenching strongly by oxygen in the combustion atmosphere. However, as long as a pre-combustion environment is considered, the fluorescence method can be used as a "thermometer" in the temperature flow-fields.

3.3.1 Overview of exciplex thermometry

The applications of exciplex fluorescence to thermometry are well extensively reviewed by Melton.[5] Although the photophysical processes underlying the commonly observed shift of the exciplex emission band to shorter wavelengths as the temperature is increased are not well understood,[116] the temperature dependence of the fluorescence quantum yield can be used for exciplex thermometry. Zhang[123] and Alexander developed and used a fluorescent thermometer which exploited the decrease in the fluorescence quantum yield of Rhodamine B with increasing temperature over the range 20°C to 185°C. Melton and coworkers [105] developed a series of fluorescent thermometry systems based on the photophysics of exciplexes, particularly those for which the E* emission is significantly red-shifted with respect to the M* emission. In these exciplex fluorescence thermometry systems, the monomer M* and the exciplex E* both fluoresce, and since the ratio of M* concentration to E* concentration is temperature-dependent,[5] either through the viscosity of the solvent (low temperature, kinetic limit), or through the equilibrium constant (high temperature, thermodynamic limit), the ratio of the intensity of emission from E* to that from M* can be calibrated as a fluorescence thermometer. Stufflebeam[124] confirmed that, as predicted for bulk non-evaporating liquids, it was indeed possible to use an exciplex fluorescence thermometer based on the intermolecular excimer formed between excited state pyrene and ground state pyrene in decane to measure the temperature within ± 1°C over the range 25°C to 91°C. The blue-shift of the exciplex fluorescence spectra could also be exploited to develop exciplex shift thermometers.[5] This shift, as measured by the ratio of the intensity in a chosen spectral bandpass on the shorter wavelength side of the exciplex emission band to that in a chosen spectral bandpass on the long wavelength side, can also be exploited as a thermometer.[125] Schrum et al.[126] have also developed a fluorescence shift thermometer which makes use of the blue shift in the fluorescence of BTBP [N,N-bis (2,5-di-tert-butylphenyl)-3,4,9,10-perylenedicarboximide] in methanol or mineral oil as the temperature increases (15°C-70°C). They achieved temperature resolution of 1-2°C.

3.3.2. DMA•TMN exciplex thermometry

Analysis of the temperature sensitivity of the exciplex emission involves taking the ratio of I_E/I_M.[5,125] This parameter can be assigned in several ways. One can ratio the intensity of the exciplex peak to that of the monomer, or ratio the intensities in a band around these peaks - although the demarcation is arbitrary, this may be done quite accurately by performing Gaussian fits to the fluorescence spectra over a certain window about the maximum, or develop some entirely different temperature characteristic such as the correlation of the shift in the fluorescence maximum (λ_{max}) with temperature. In Section 3.2.2, temperature-dependence of the exciplex fluorescence quenching of 5% DMA•5% 1,4,6-TMN system was discussed in detail. As temperature increased, the fluorescence intensity decreased greatly and the overall emissions were blue-shifted as shown in Fig. 28. In terms of Gaussian band shape analysis, both of the intensities (i.e., shorter wavelength side (I_M) and longer wavelength side (I_E)) within the exciplex fluorescence intensity were obtained and recorded in Table 5. The ratios of these intensities could be used as an exciplex thermometer with temperature range from 28°C to 150°C. As increasing temperature the change of the fluorescence ratio ($\ln [I_E/I_M]$) was greatly decreased. The solid line is the best fit with an exponential decay equation; $y = a\,exp(-bx) + c$ with the fitting constants, $a=16.61$, $b=0.024$ *and* $c=-0.24$, respectively. Figure 29 shows the calibration result of 5% DMA•5% (1,4,6-TMN) exciplex thermometry in 90% isooctane.

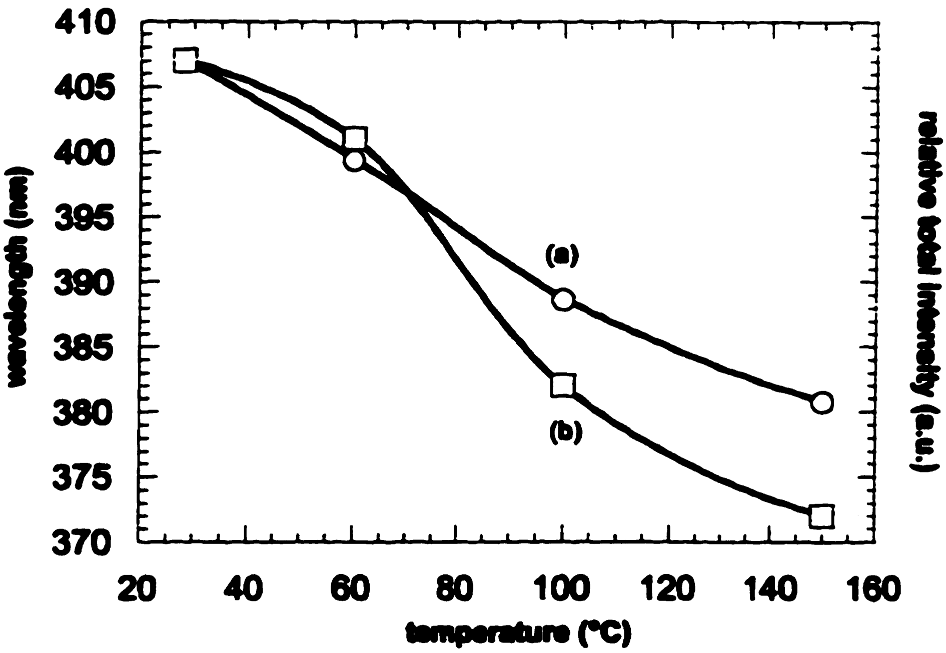

Figure 28. The change of total fluorescence intensity (a) and corresponding wavelength change at peak intensity (b) in Fig. 26 with respect to temperature. The total intensities are relative to each other.

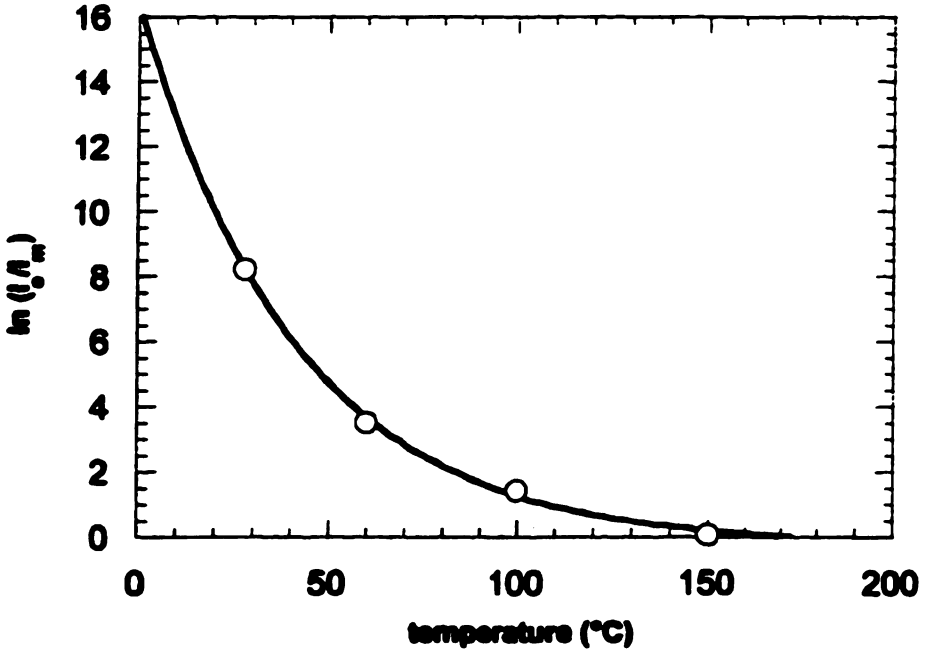

Figure 29. The fluorescence intensity ratio [$\ln (I_e/I_m)$] of exciplex to the monomer with respect to increasing temperature. The fluorescence intensities were calculated based on Gaussian band shape analysis. The solid line is a data fit equation ; $\ln (I_e/I_m) = a\exp(-bT)+c$, with $a=16.6$, $b=0.024$ and $c=-0.2421$, respectively.

Table 5. Pure monomer (I_M) and exciplex fluorescence (I_E) intensity and their ratios as a function of temperature. Both of the intensities were obtained by using the Gaussian band shape analysis.

Temperature (K)	Area of the exciplex fluorescence (×10^6) [I_E]	Area of the monomer fluorescence (×10^6) [I_M]	ln[I_E/I_M]
301.1	12.11	0.0032	8.24
333.1	9.81	0.29	3.53
373.1	5.14	1.20	1.45
423.1	1.84	1.68	0.095

Chapter IV. Experimental Methods (II): Physical Characterization of the Exciplex

4.1. Chapter Overview

This chapter presents the details of how a sample is prepared, and calibrated quantitatively for both of liquid and vapor phase fuel. It begins by describing the photophysics of Laser Induced Exciplex Fluorescence (LIEF) visualization whose fluorescences were employed in the calibration. Fundamental optics is described to explain how the image is acquired and processed. The most significant section is devoted to describing the liquid and vapor phase calibration process, such as relating fluorescence intensity to the concentration of liquid and vapor, particularly emphasizing two different procedures between direct- and indirect pressure measurement in the vapor phase calibration. In that Section, the calibration results for both liquid and vapor phase are discussed in detail and the crucial differences between direct- and indirect pressure measurement for vapor phase concentration are emphasized. The final section of this chapter describes the experimental methods for actual measurements of fuel LIEF imaging in a test quartz cylinder and in a motored engine.

4.1.1. Exciplex emission in liquid and vapor phases

The absorption and fluorescence spectra of organic molecules dissolved in non-polar solvent, such as typical fuels, are virtually identical to the spectra of the same molecules in the vapor phase. However, in some cases it is possible to react the fluorescing excited state molecules, M^*, with an appropriate ground state partner, Q, to form a second fluorescing species, $M\text{-}Q^*$, called an exciplex (E^*). The common mechanism for exciplex formation is the reversible equilibrium[106] which governs the concentration of the exciplex complex. A general scheme for the overall exciplex process is shown in Scheme 1 in Section 3.2.2.

In the liquid phase, the equilibrium may be shifted far to the right by adjusting the concentration of M and Q. Upon vaporization, the concentration of M and Q will be reduced so that M^* emission will dominate. Moreover, the equilibrium is temperature dependent, shifting to the left as temperature increases. Accordingly, the exciplex is less stable at elevated temperatures and the exciplex fluorescence emission is attenuated with respect to that for the monomer. For these reasons, in the Laser Induced Exciplex Fluorescence technique, the vapor phase fluorescence is dominated by M^* and the liquid phase emission is characterized by the red-shifted emission of the exciplex.[59,105] Because the exciplex forming dopants, M and Q, are typically dissolved in a non-fluorescing solvent which serves as a fuel, the liquid phase fuel is distinguished by the distinct emission from the exciplex, E^*, and emission from the monomer M^* will track the evaporating fuel. Figure 30 shows the fluorescence emissions from the vapor and liquid phase using a 5%DMA•5%TMN exciplex system in 90% isooctane solvent. The vapor and liquid phase fluorescence are dominated by the monomer (DMA) and DMA•TMN exciplex pairs, respectively. With the 308 nm excitation, the maximum intensity wavelengths for the vapor and liquid are 344 (nm) and 408 (nm), respectively.

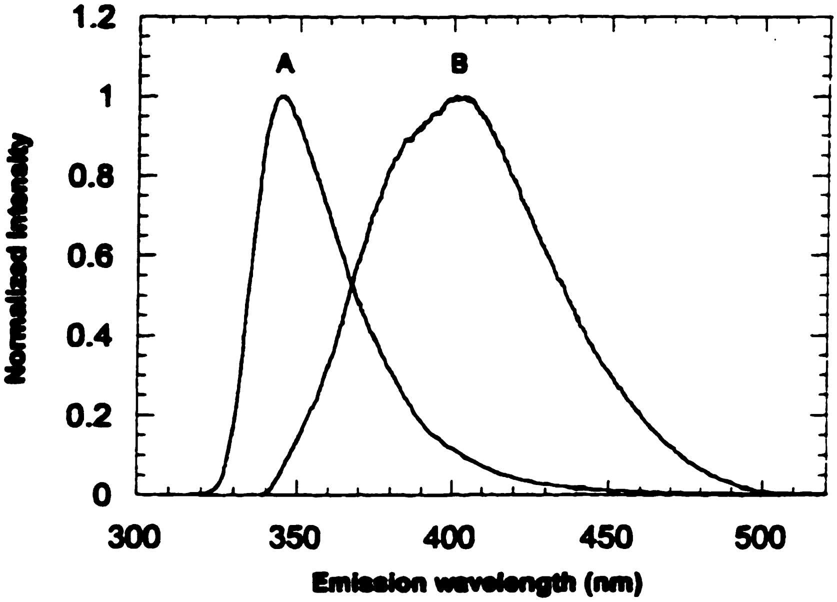

Figure 30. Vapor and liquid phase fluorescence emissions (A: vapor phase, B: liquid phase). 5%DMA•5%1,4,6-TMN exciplex system in 90% isooctane solvent was used.

4.2. Optical setup for two phase fluorescence intensity calibration

4.2.1. General field-optics

A general schematic diagram of a calibration experiment is shown in Fig. 31. The setup utilized the sample system, excimer laser, laser energy meter, light sheet forming optics, intensified CCD detector, and detector controller. The excimer laser was used as the excitation source, operating at a wavelength of 308 *nm* (XeCl line) with a maximum power of 150mJ/pulse at a maximum repetition rate of 250 Hz. Light from the excimer laser passed through a custom-made variable beam-attenuator with removable quartz discs for adjusting the pulse energy to a desired level, and a field stop to cut off the fringes. It then passed through the beam-splitter for the energy meter, and a field-optics consisting of fused-silica cylindrical focusing lens with a 300 *mm* focal length and a cylindrical recollimating lens with a -37.5 *mm* focal length to generate a 800 microns thick (FWHM) and 20.6 mm high vertical sheet, and finally the sample in the sample system. The fluorescence from the vapor (or liquid) was imaged by a quartz camera lens (Nikkor UV lens, 50 mm, f/11) onto a digital computer-controlled image acquisition system (Princeton Instruments ICCD-576x384) equipped with a gated image intensifier. For the laser-induced exciplex fluorescence (LIEF) imaging, laser and camera gate are all electronically synchronized to acquire the image. Fluorescent images taken are transferred to computer memory and written to disk. Two band-pass filters were employed in this study; for the vapor phase, a band-pass filter (CVI Laser Model F35-355-4), centered at 349.1 nm with 37.8 nm FWHM, was used and for the liquid phase, a long-pass filter (Corion LL-400-S) was employed. The relative transmittance of these

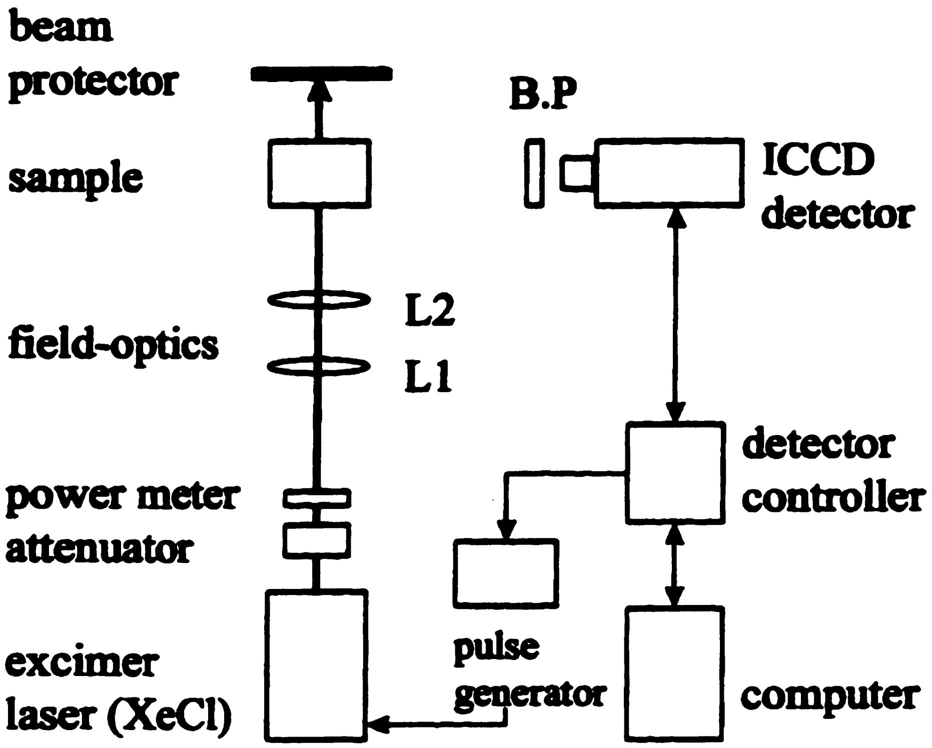

Figure 31(a). Schematic diagram of calibration experiment of fuel vapor and liquid droplet

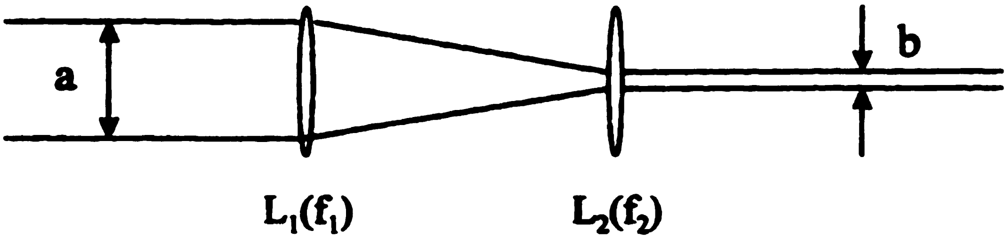

Figure 31(b). Schematic diagram of field optics to make a sheet of light. (a) and (b) are initial and final beam widths, 6.6 mm and 800 μm, respectively. L_1 and L_2 are fused silica convex and concave lens with focal length $f_1 = 300\ mm$, $f_2 = -37.5\ mm$, respectively.

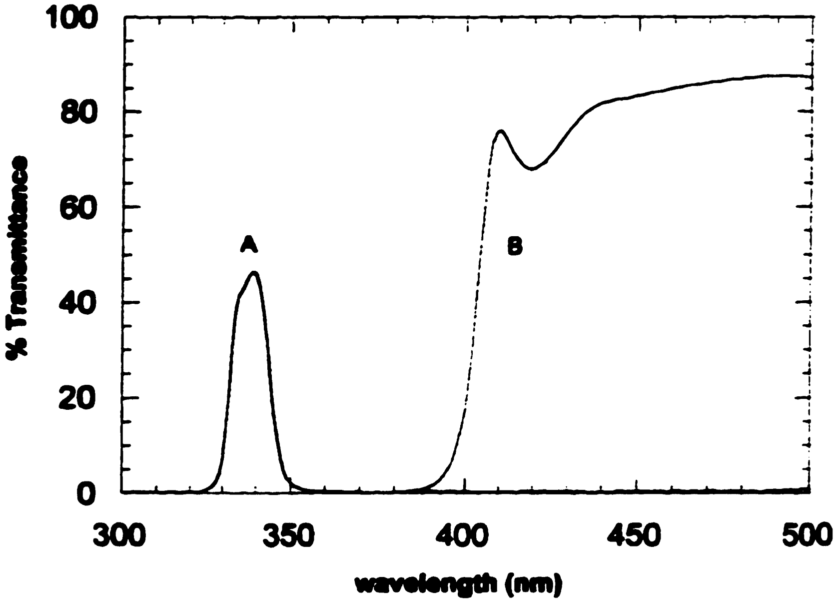

Figure 32. Bandpass filter % - transmittance (A: for vapor phase, B: for liquid phase).

bandpass filters are shown in Fig. 32. The fluorescence intensity data was extracted from the images and normalized with the laser pulse intensity and detector gain and finally correlated to the species concentration.

4.2.2. Field of view of image

When used for 2 dimensional imaging applications, Princeton Instruments ICCD cameras are designed to optically replicate a standard 35 mm SLR camera. The main difference between the two, however, is the size of the collected image - or the field of view at a given distance. Before calculating the field of view at a given distance, it is useful to first establish some definitions.

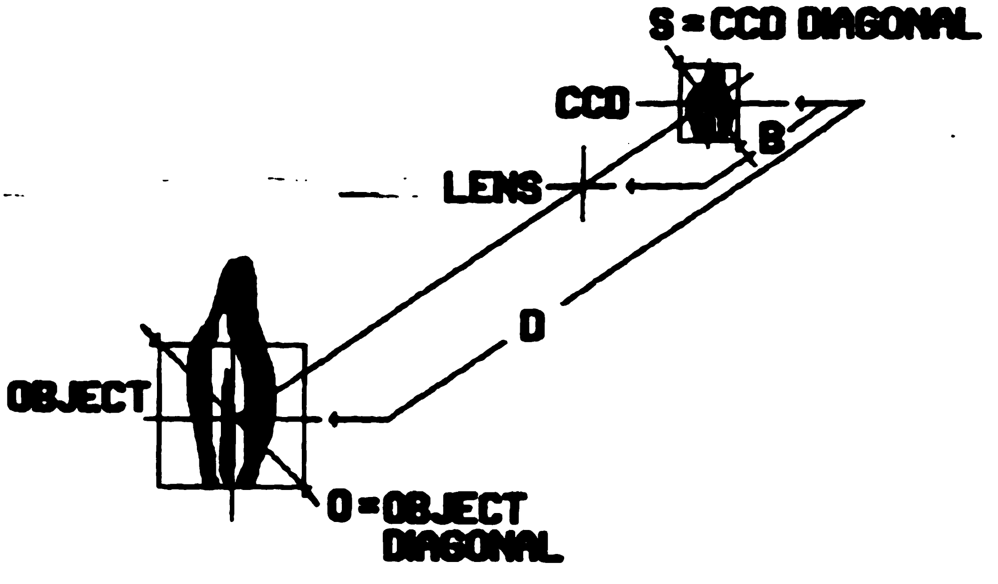

Figure 33. Imaging Field of View[127]

D : distance between image and focal plane of camera. (Focal plane of camera is 46.5 mm back from front edge of lens adapter), B : distance between objective lens and focal plane, F : focal length of the lens used (50 mm), S : ICCD diagonal dimension, O : field of view covered at a distance, D (or portion of object that is imaged).

Then the field of view can be calculated as

$$O = \frac{S}{M} \qquad \text{where} \quad M = \frac{FD}{(D-B)^2}$$

As an example, for an ICCD camera with a Thomson 7883, each pixel has a spatial resolution of 23 μm × 23 μm with 576 × 384 arrays. Therefore, the diagonal dimension of the focal plane of the ICCD camera is 15.9 mm. In the vapor-liquid calibration experiment, the distance between image and objective lens was set at 127 mm, and 50 mm Nikkor objective lens on a 18 mm extension tube was employed. With these parameters, the magnification (M) of the objective image and the field of view (O) can be calculated as

$$M = \frac{50 * (127 + 18 + 46.5)}{127^2} \approx 0.593$$

$$O = \frac{15.9}{0.593} = 26.81(mm)$$

By analogy, the horizontal and longitudinal field of view of the objective image can be calculated as 14.84 mm and 22.34 *mm*, respectively. Therefore, a calibration image area (liquid droplet or vapor) approximately 39 μm wide × 39 μm high was focused onto a single pixel (23 μm × 23 μm) of the detector.

4.3. Intensity-concentration calibration

4.3.1. Vapor phase

The vapor phase calibration was carried out in two steps using a sample of N,N-dimethylaniline (DMA), the vapor phase marker. The first step was to determine the vapor phase concentration versus temperature of the sample. The second step was to determine fluorescence intensity versus vapor temperature. Using the concentration-temperature relationship from the first step, the relationship between the fluorescence intensity and the vapor concentration of the sample could be obtained. There are two methods to obtain the vapor phase concentration. One method is the absorption measurement suggested by Rotunno et al.[62] For example, in order to calculate the vapor concentration of TMPD, Melton measured absorbances of TMPD as a function of temperatures and employed the Beer-Lambert law where he used the molar absorption coefficient ($\bar{\varepsilon}$) of TMPD cited from Berlman.[66] The other method proposed here is the direct-pressure measurement explained in Section B. This section is mainly devoted in describing the main differences in the vapor phase calibration procedures between the two methods.

A. Absorbance Measurement (Indirect pressure measurement)

a. Sample preparation and apparatus

For the vapor phase calibration, a small sample of oxygen-free, pure DMA was prepared using a standard freeze-pump-thaw method, and inserted to the quartz fluorimeter cell with a stem and 10 mm light path length, purchased from NSG Precision Cells. Before placing the sample in the cuvette, an absorbance measurement was made on the empty cuvette with the spectrophotometer. This was the blank signal that was used to subtract the effect of the cuvette walls from the subsequent sample measurements.

Temperature-dependent fluorescence measurements over a range from 30 - 200 °C, were performed with an apparatus consisting of a Pyrex round bottom and a 1 cm quartz cuvette. The design of the cell permitted the liquid sample to be prepared under high vacuum conditions, thereby excluding oxygen as a possible quenching source. Liquid samples were added to the round bottom using a microliter syringe fitted with a 10 inch hypodermic needle so that the sample could be placed on the round bottom, keeping the walls optically clear. Oxygen contained in the DMA solution was thoroughly degassed several times by standard freeze-pump-thaw procedures to make sure there was no more oxygen than 10^{-4} Torr. The DMA solution was frozen with liquid nitrogen, evacuated to 10^{-4} Torr, and thawed with warm tap-water. Approximately 200 microliters of DMA liquid sample were then vacuum transferred to the cuvette and isolated by sealing a second Kontes quick-release teflon valve between the two chambers. The cuvette portion of the cell could be detached from the round bottom so that it could easily be introduced into a high temperature apparatus designed to permit temperature control of the fluorescence cuvette during spectroscopic measurements. The sample heating chamber is shown in Fig. 25 and described in Section 3.2.2.

b. Calibration procedure

The first step was to determine the vapor concentration versus temperature from absorbance measurements with a UV-VIS spectrophotometer (CARY 1E Varian Model). Increasing the temperature of the sample increases the vapor concentration by increasing the saturation vapor pressure. The temperature-controlled sample heating system was mounted in the sample compartment of the spectrophotometer for this purpose as shown in Fig. 34. Measurements were made at a 10° C intervals from room temperature to 200° C.

The spectrophotometer was allowed to warm up approximately one hour and zeroed with sample chamber windows of the heating system in the sample beam. This removed the effect of the windows from the measurements. The reference beam was empty, i.e. air was the reference. The sample was then placed in the sample chamber of the heater and absorbance measurements were taken after the temperature equilibrated at each interval. After subtracting the blank signal, concentration was calculated using the Beer-Lambert's law

$$A(T_i) = \varepsilon\, b\, C\, (T_i)$$

where A is the absorbance, ε is the molar absorption coefficient, b is the path length (cm), and C is the unknown concentration of DMA vapor.

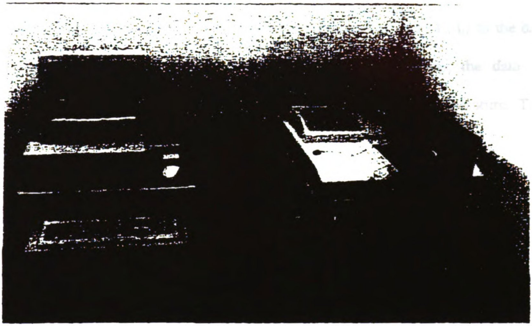

Figure 34. DMA sample absorbance measurement instrument using a temperature-controlled sample heating system with spectrophotometer.

The second step in the vapor phase calibration was to determine fluorescence intensity versus vapor concentration using the vacuum sealed DMA sample. Again, temperature was used as a specific parameter to vary the vapor concentration of DMA. Therefore, at a given temperature one pair of data (T_i, I_i) of DMA fluorescence emission intensity (I_i) and temperature (T_i) could be obtained. By correlating the pairs of data (T_i, I_i) to the data pairs of (T_i, C_i), which could be inferred from the first calibration step, the data pairs of fluorescence intensity versus concentration $(I_i, C_i)_{T=T_i}$ at a specific temperature, $T=T_i$, can then be developed.

c. Image acquisition and analysis

Images of the fluorescence were taken perpendicular to the laser sheet at approximately 10° C increments with the intensified CCD detector. A bandpass filter (CVI Laser Co. Model F35-355-4), centered at 349.1 nm with 37.8 nm FWHM, was employed to collect only vapor phase fluorescence. A general optics setup to acquire vapor phase fluorescence is shown in Fig. 35. The system was synchronized by externally triggering the ICCD detector from the excimer laser through the FG-100 pulse generator and the ST-130 detector controller. Several images were taken at each concentration level using 10 exposures per readout with background subtraction, and stored on the computer. The average pulse energy of the 10 pulses most nearly associated with each image was recorded for image processing later. The detector hardware parameters are adjusted by ten-turn potentiometers, but are not linear with the turn units on the dial face. Calibrations for these potentiometers, along with other operational information to assist the user, are contained in the Appendix.

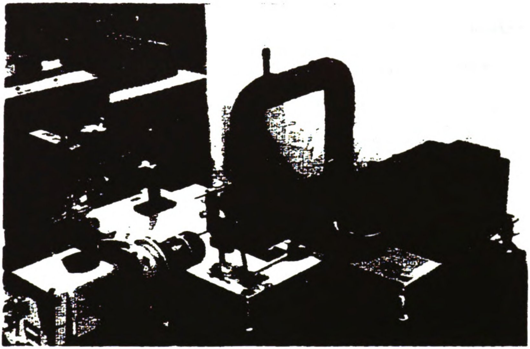

Figure 35. Experimental set-up for determining fluorescence intensity of DMA vapor phase (sample heating system with insulation removed).

Fluorescence intensity data were extracted from the images using the CSMA software.[128] A rectangular region of interest (ROI) containing the cuvette image (except the edges) was defined, and the average intensity per pixel was calculated. The region of interest remained the same for all images. The average intensities were normalized by the pulse energy, corrected for detector gain, and corrected for the attenuation effects of the quartz windows and cuvette walls. Finally, the intensities were plotted resulting in a calibration curve of fluorescence intensity versus mass concentration of DMA vapor. The concentration of fuel vapor was then inferred based on the mixture ratio of DMA to fuel.

B. Direct Pressure Measurement

a. Pressure Sensor Calibration

The MPX 2100-D series device is a silicon piezo-resistive pressure sensor providing a highly accurate and linear voltage output - directly proportional to the applied pressure. The sensor is a single, monolithic silicon diaphragm with the strain gauge and a thin-film resistor network integrated on-chip. This sensor is temperature compensated over 0° C to 85° C and able to measure pressure over 0 to 1000 *torr*. Prior to use in the vapor phase calibration experiment, the sensor was calibrated using a vacuum pump and a Baratron capacitance manometer (MKS Instruments Model 145BHS-1000) with a 0-1000 *torr* measurement range. Figure 36 shows a schematic diagram of a sensor calibration. A vacuum pump was used to decrease the air pressure in the sensor at a 100 torr interval, and the reduced air pressure, as well as sensor output voltage, were measured simultaneously by a Baratron manometer and multimeter,

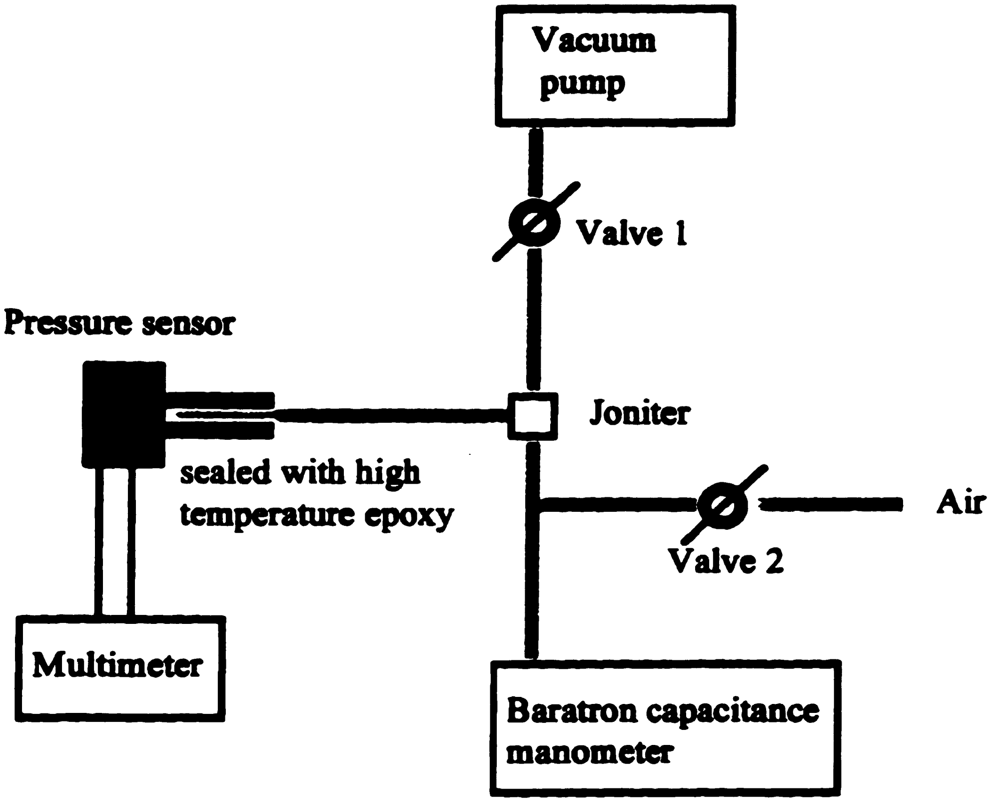

Figure 36. A schematic diagram of MPX2100-D pressure sensor calibration experiment setup.

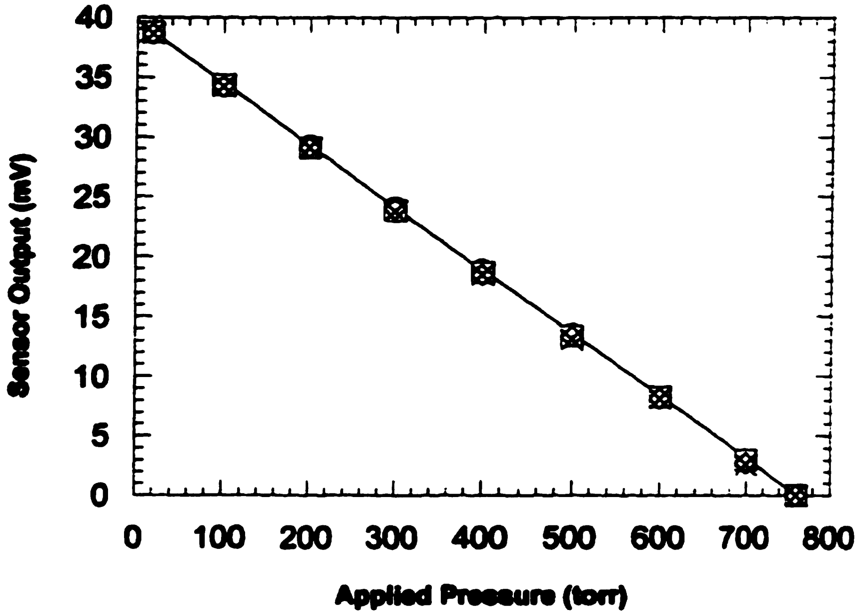

Figure 37. MPX-2100D pressure sensor calibration result. Solid line is the least squares fit to the equation $y = -0.0524x + 39.6$, max. deviation of 0.343.

respectively. At the lowest pressure, the sensor was allowed to leak, thereby increasing the pressure up to 700 *Torr*. Figure 37 shows a calibration of the sensor. In a series of calibrations, the data were quite repeatable and showed a linear relationship between the sensor output voltage and applied pressure. The linear regression fitting gives $y = -0.0524x + 39.6$ with maximum deviation of 0.343 and was used in the vapor phase calibration to obtain the DMA vapor pressure.

b. Experimental apparatus for pressure sensor calibration

The first procedure was to measure vapor pressure directly with respect to temperature. For this measurement, the high temperature sample cuvette was extensively modified, as shown in Fig. 38, to measure the DMA vapor pressure and temperature simultaneously. Two Pyrex tubes (ϕ = 1/8") were attached to the main stem to allow the insertion of stainless-steel tubing (ϕ = 1/16") that was connected externally to the pressure sensor and thermocouples. The *Kovar* joint, which is composed of Pyrex (ϕ = 1/8") and a metal tube (ϕ = 1/16"), was inserted between two Pyrex tubes and a sensor, and then silver soldering was provided to make sure that it was leak-tight. A J-type thermocouple, which is a plug-type configuration sensitive on the tip and sheathed with stainless-steel to protect the sensor part, was used to measure the vapor temperature inside cuvette and connected gauge indicator 2. A MPX-2100D pressure sensor was employed in this measurement. This sensor had a vacuum side port and a 1/16"- stainless steel tubing was inserted into it and sealed with high temperature epoxy. The temperature of the sample heating chamber could then be increased up to 200° C and be well-

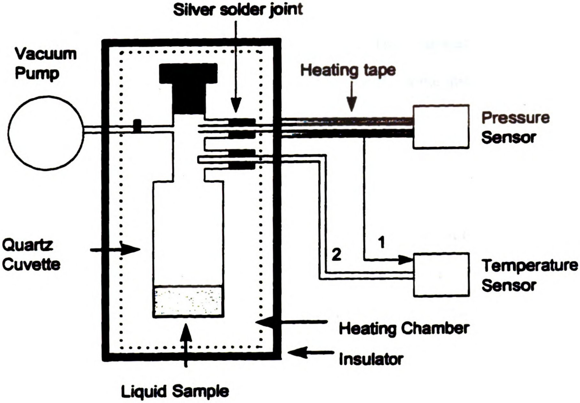

Figure 38. Vapor phase calibration instrumentation

insulated with the aluminum silicate ceramics. Thermal insulation was necessary to avoid the evaporated DMA vapor condensation along the stainless steel tubing which was in the room temperature environment. Therefore, it was wrapped with heating tape and maintained at constant temperature (150° C) during the measurement. This temperature was constantly monitored with thermocouple gauge indicator 1. With the aid of the instruments, the DMA vapor pressure and temperature were measured simultaneously.

c. Calibration procedures

The vapor pressure was measured at 10° C intervals from room temperature to 210° C. Once a *P-T* phase diagram was established, the molar concentration (n/V) could be determined using the equation of state of an ideal gas ($PV = nRT$). P and V are gas vapor pressure and sample cuvette volume, n is the number of moles of the sample, and R and T are gas constant ($\approx 8.31 J/mole\ K$) and temperature, respectively. This direct pressure method directly depends on the equation of state for an ideal gas. There are two main criteria[129] for the applicability of the ideal gas law . First, if the vapor pressure (P_v) is much smaller than the critical pressure P_c, i.e., $P_v << P_c$, the ideal-gas law can be assumed, regardless of the temperature. Secondly, at high temperature, greater than about $2T_c$, the ideal-gas law can be assumed to vapor pressures as high as four or five times P_c.[129] In the vapor phase calibration experiment, the DMA vapor pressure was regulated in terms of temperature of the sample cuvette and increased up to 760 *Torr*. The critical pressure and temperature of DMA [130] is 35.8 *atm*. at 687.5 *K*. Therefore, the ratio of P_v / P_c is of order 10^{-2}. With this ratio, it is reasonable to use the ideal-gas law to calculate DMA gas phase concentrations, as long as there exists liquid and vapor phase equilibrium with respect to temperature.

The second procedure was to measure vapor fluorescence intensity with respect to temperature as mentioned in Section A for the absorbance measurement method. Again, the same pair of cylindrical-fused silica lenses were used to generate a sheet of light (800 μm thick and 20.6 mm long) and a bandpass filter (CVI Laser Co. Model F35-355-4), centered at 349.1 nm with 37.8 nm FWHM, was employed to collect vapor phase fluorescence. Combining the results, one could correlate the fluorescence intensity and vapor phase concentration. The fluorescence intensity data was extracted from the images and normalized with the laser pulse intensity and detector gain, and finally correlated to the species concentration. The overall image acquisition procedures and data analysis methods are the same as the indirect pressure measurement method mentioned in Sec. A

4.3.2. Liquid Phase

The liquid phase calibration was carried out in a single step by taking fluorescent images of known sized droplets of exciplex-doped fuel with the ICCD detector. In the liquid phase calibration, 5%(w)DMA•5%(w)1,4,6-TMN exciplex system was used in 90%(w) isooctane solvent. Here, percent weight ratio was used. The fluorescence intensity of the droplets was then calculated from the images and plotted versus droplet mass. Again, the excimer laser provided an 800μm sheet of excitation light for the fluorescence and images were taken with the ICCD detector. The sheet forming optics and experimental setup were the same as in the vapor phase in Fig. 35. However, the

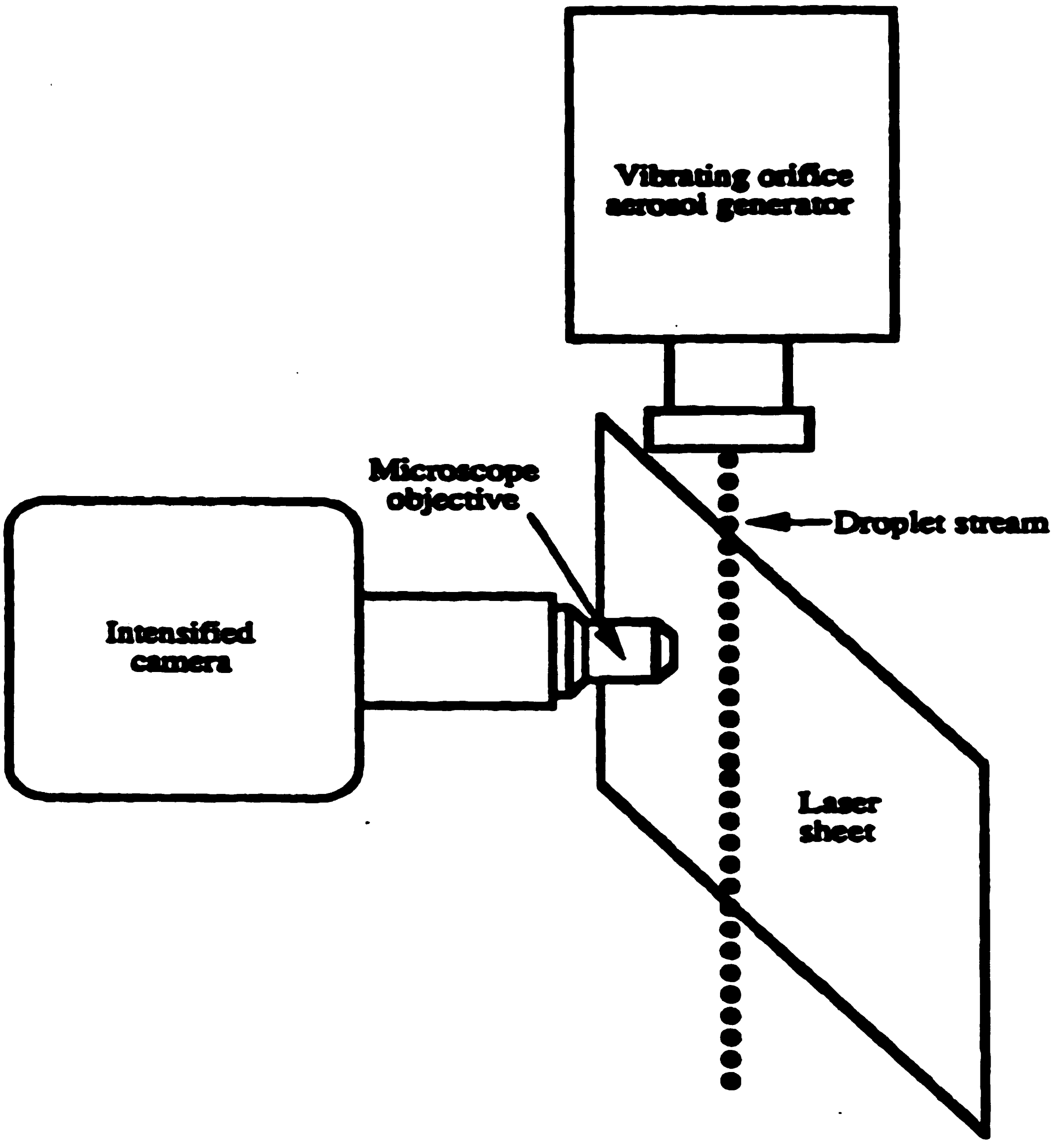

Figure 39. Experimental arrangement for droplet calibration.[131]

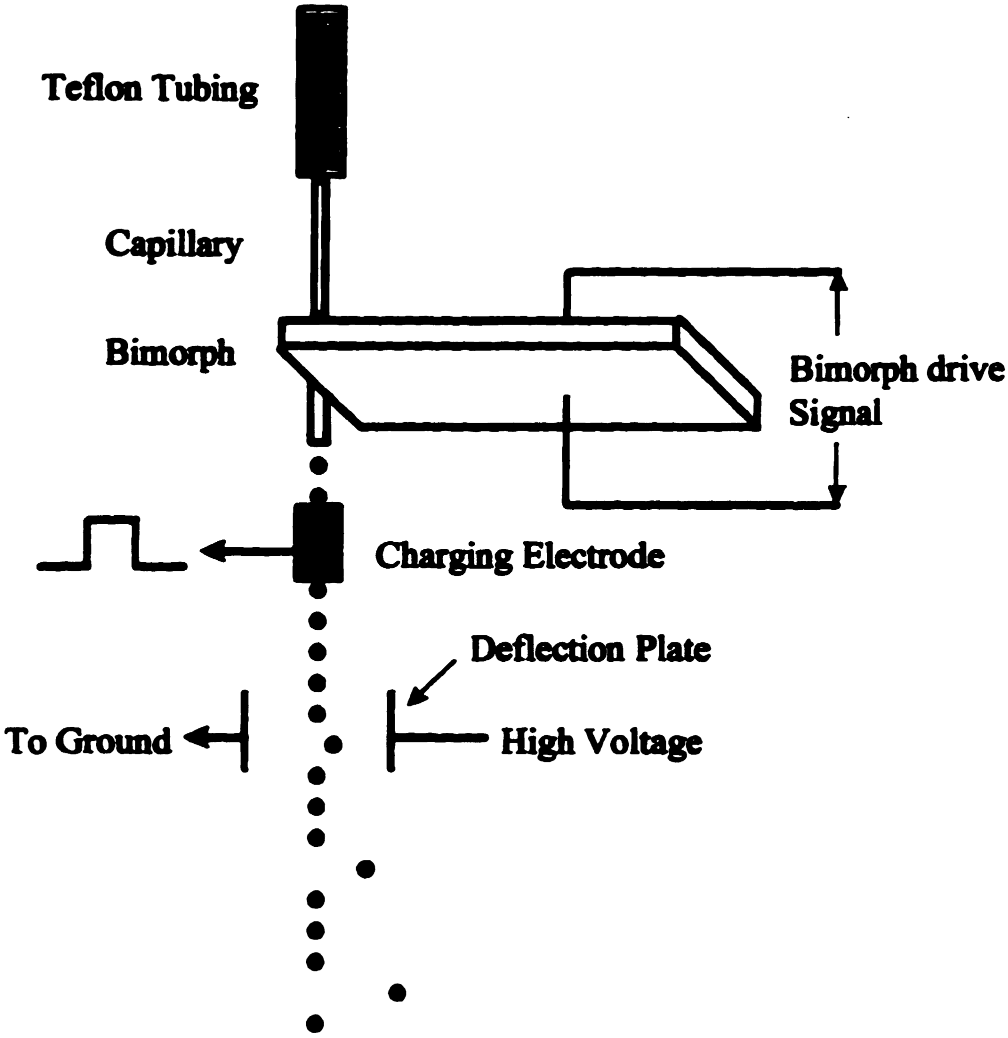

Figure 40. Schematic diagram of the droplet formation module of the isolated droplet generator.

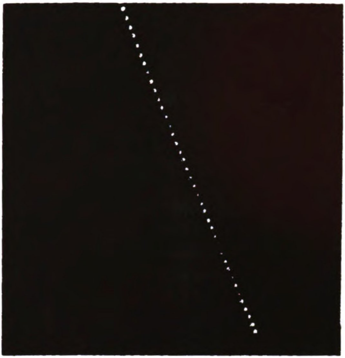

Figure 41. A view of fluorescent image of isolated droplet. The droplet was made by using a 5%DMA•5%1,4,6-TMN exciplex system in 90% isooctane solvent.

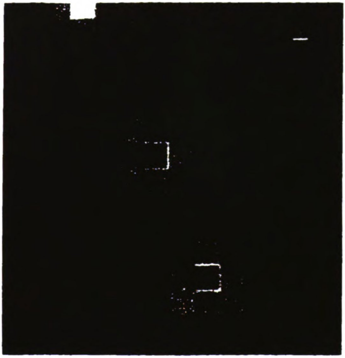

Figure 42. A zoom of some individual isolated droplet in Fig. 41. CSMA software was used to make a zoom.

bandpass filter in front of the detector was then changed to a long pass filter (LL-400-S Corion Co.) which transmitted long wavelengths beyond 400 nm. The droplet streams produced by the isolated droplet generator was directed downward through the vertical laser light sheet. Droplets were generated in the 90 to 180 microns diameter range by varying the flow rate through 20, 30 and 45 micron capillaries, and by varying the droplet production frequency from 7,000 to 28,000 drops per second. The isolated droplet generator, vertical laser sheet, and ICCD detector setup for the liquid phase calibration are shown in Fig. 39. Figure 40 is the droplet forming module showing the glass capillary and bimorph. With this image acquisition experimental setup, a series of droplet streams taken during the liquid phase calibration at a droplet production rate of 14,000 per second, is shown in Fig. 41 and a zoom of some droplets using the image processing software (CSMA) is shown in Fig. 42. Fluorescence intensity data was extracted from the images by zooming in on individual droplets and calculating the total intensity by summing the intensity values of the pixels containing the droplet. Since this calibration could be done in the open atmosphere and no quartz windows or cuvette were in the optical path, the intensities only needed to be corrected for detector gain. The intensities were again normalized by the pulse energy and the result was a calibration curve of fluorescence intensity versus mass of liquid fuel.

4.3.3. Result and discussion

A. Vapor phase

a. Absorbance measurement

Temperature-dependent DMA absorbance data are shown in Fig. 43. Temperature was allowed to vary over the 30° C to 200° C range at approximately 10° C intervals and kept constant within ± 1° C. The spectrophotometer scanned the absorbance of the DMA vapor phase over a range from 330 nm to 230 nm with a 1 nm resolution. There were no appreciable absorption bands in the far-visible regions. As temperature increased the absorbance of DMA vapor increased throughout the scan wavelengths, and finally saturated at high temperature. From these absorbance spectra, the absorbance of DMA vapor phase as a function of temperature could be deduced at 308 nm excitation line. The results are shown in Fig. 44. In the earlier stage of the sample heating process of the liquid DMA, there was no appreciable absorbance increase. However, further increasing the sample temperature yielded a higher absorbance with a saturation at a temperature near 150° C. In order to obtain the vapor concentration of the DMA as a function of temperature, the absorbance data in Fig. 44 was correlated to the Beer-Lambert law (absorbance [A] = εbC; ε is the absorption coefficient (L $mol^{-1}cm^{-1}$), b is the pass length (cm), and C is the DMA concentration (mol L^{-1})). In a series of experiments, the absorption coefficient (ε) of DMA in isooctane solvent was found to be 3.706×10^3 (L $mol^{-1}cm^{-1}$) as shown in Fig. 45 and temperature-dependent concentration could be calculated.

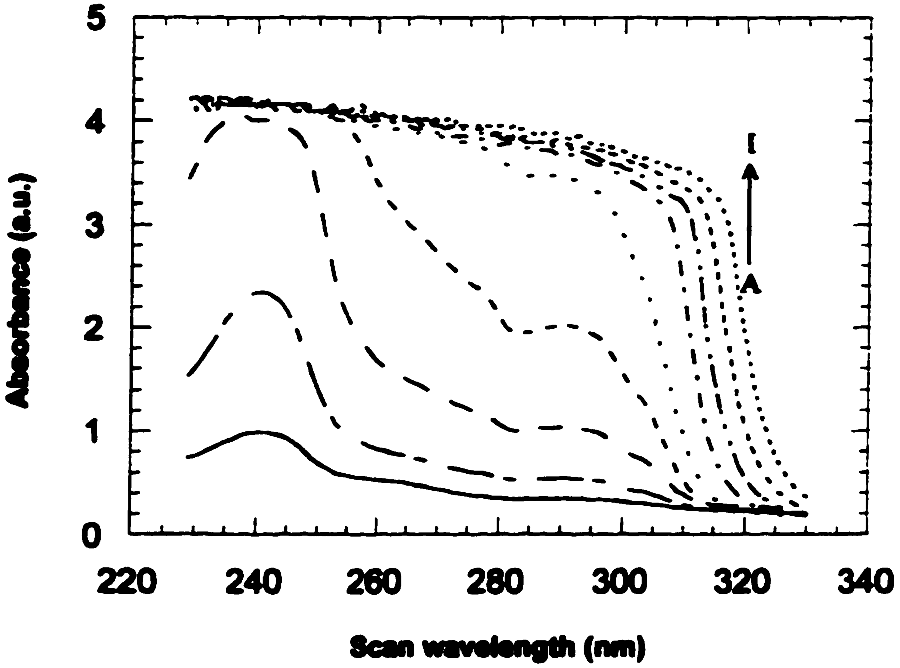

Figure 43. Plots of DMA vapor phase absorbances with respect to the wavelength (nm). Absorbance was measured with increasing temperature at a 20 °C interval from 30 °C (A) to 200 °C (I).

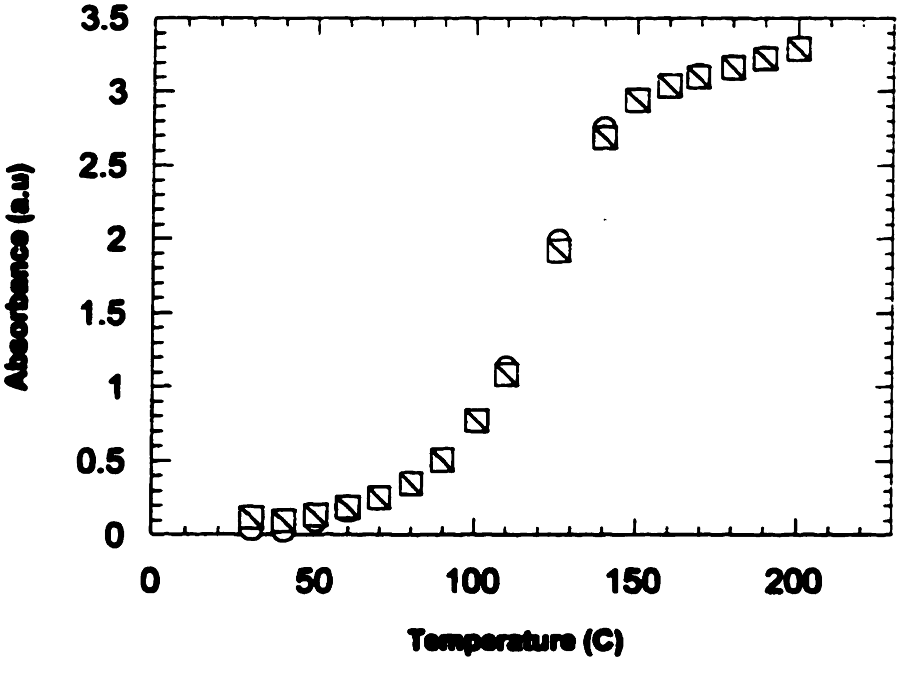

Figure 44. A plot of DMA vapor absorbance versus temperature at 308 *nm* excitation line. This plot was made by using Fig. 43.

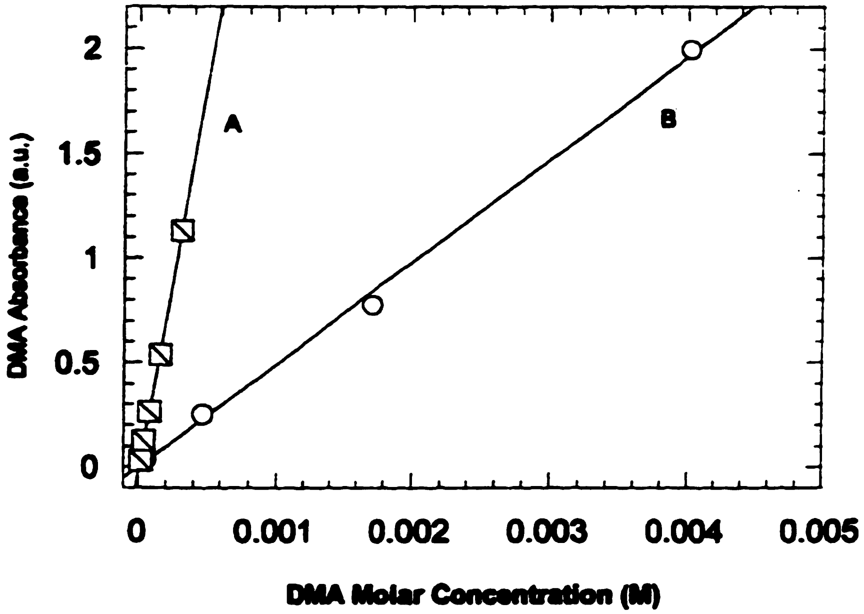

Figure 45. A plot of DMA absorbance versus concentration to calculate molar absorption coefficient. A is for liquid phase, and (B) is for gaseous phase. The fitting constant are 3700 and 482 (L mol^{-1} cm^{-1}) for liquid and gaseous phase, respectively.

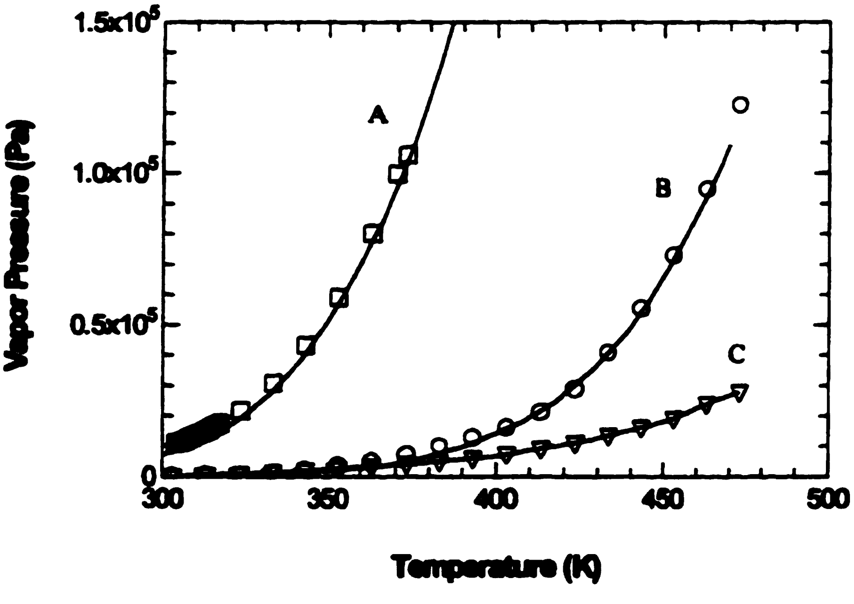

Figure 46. Vapor pressure-temperature phase diagram of the exciplex forming dopants; (A): isooctane, (B): DMA, and (C): 1,4,6-TMN. Solid line is the Clausius-Clapeyron Eq..

b. Direct Pressure Measurement

The relationship of the vapor phase pressure to temperature of the exciplex forming chemicals is shown in Fig. 46. The vapor pressure of isooctane, DMA, and 1,4,6-TMN was measured with increasing temperature. Among them, the isooctane had the highest vapor pressure at a given temperature. Based on the Clausius-Clapeyron equation (indicated with a solid line in Fig. 46), the measured data points for all three exciplex dopants were well matched with the theoretical calculations, except in the low temperature regions. It is believed that this is due to inaccuracies in the pressure sensor, especially at low temperatures. From the temperature-pressure relation of the DMA phase diagram, the measured vapor pressure of DMA can be correlated to the molar concentration (M) as a function of temperature as shown in Fig. 47.

In order to get the relationship of concentration to absorbance, it was necessary to correlate the absorbance data obtained in Fig. 43 with the concentration data shown in Fig. 47, using a common parameter, i.e., temperature. Figure 48 shows the concentration-absorbance relationship of DMA vapor phase. At low concentration of DMA the absorbance was quite linear and saturated as the concentration increased. In order to find out the molar absorption coefficient of DMA vapor phase, the linear parts of Fig. 48 were used and fitted with Beer's law ($A=\varepsilon bC$). The molar absorption coefficient was found to be 482 L mol^{-1} cm^{-1} as shown in Fig. 49.

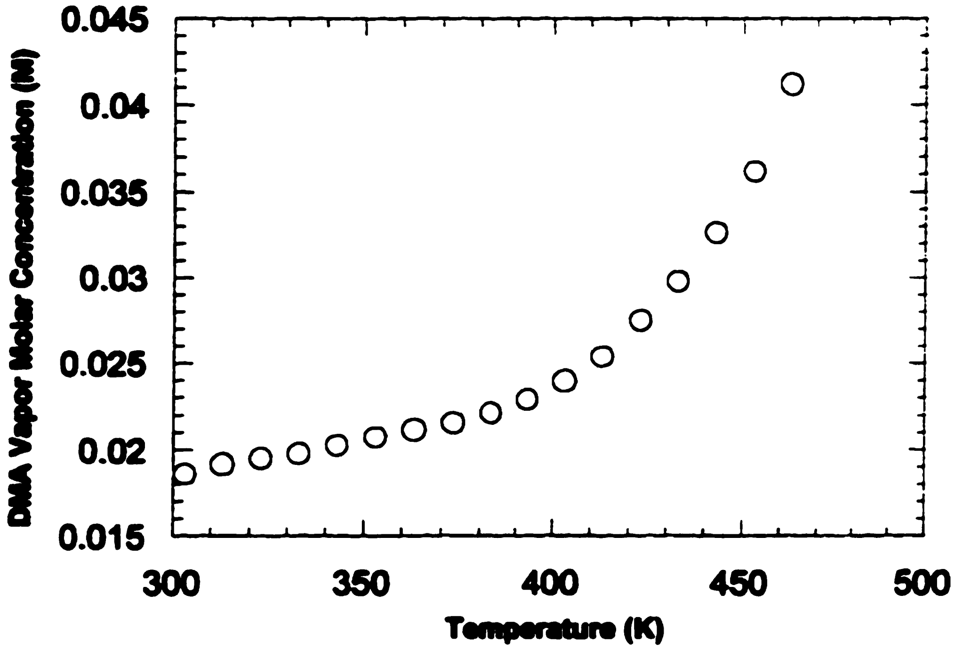

Figure 47. A plot of DMA vapor phase molar concentration versus temperature.

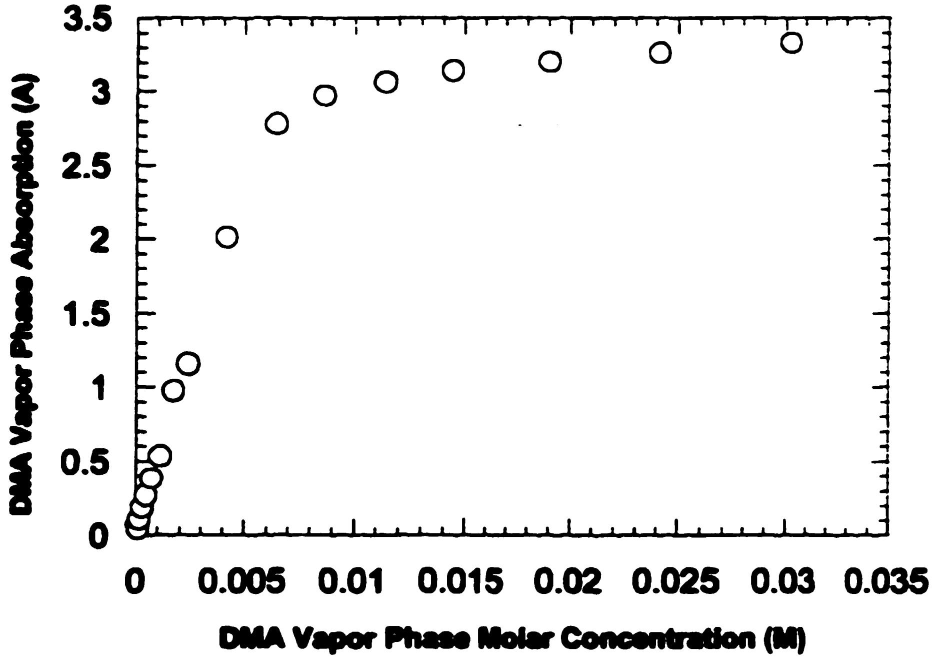

Figure 48. A plot of DMA vapor phase absorbance with respect to molar concentration.

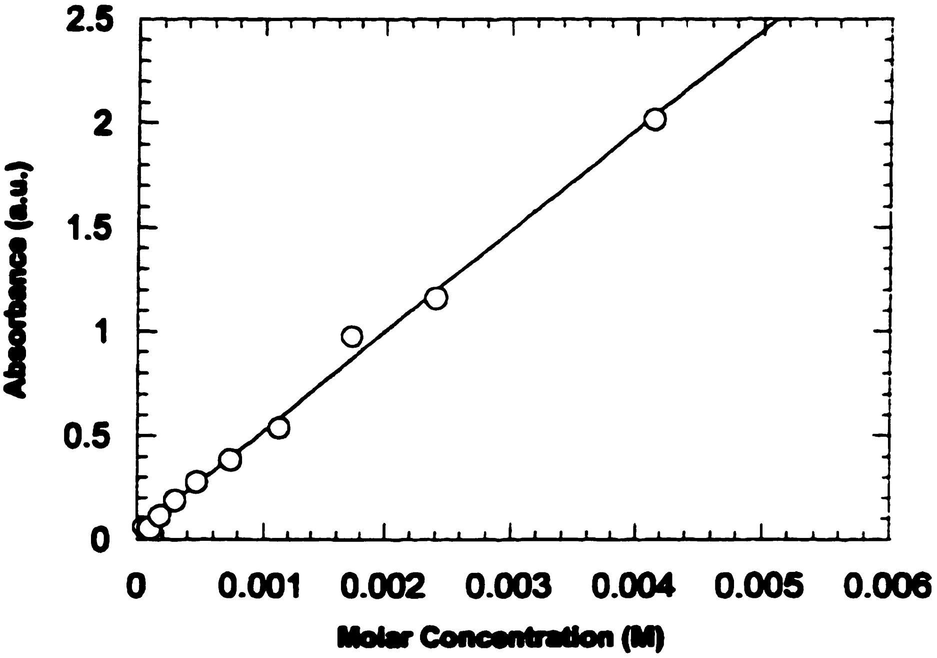

Figure 49. A plot of Beer-Lambert law of DMA vapor phase. Molar absorption coefficient (ε) of DMA vapor phase is found to be 482 (L mol^{-1} cm^{-1}).

c. Analysis of calibration data

In the vapor phase calibration, DMA fluorescence intensity images were captured at a series of temperatures. At high temperature ($T \geq 160°$ C) the emission intensity was saturated probably due to the high concentration of the DMA vapor phase. The captured image intensity (T_i, I_i) and DMA molar concentration (T_i, M_i) from the temperature-pressure data from Fig. 46 were correlated to determine the intensities and vapor concentration $(I_i, M_i)_{T=Ti}$, at temperature $T=T_i$, respectively. The calibration curve derived from these data is shown in Fig. 50. Here, the emission intensity was normalized by the excitation laser intensity and by the detector gain. Again the saturated emission intensity was due to the high concentration of DMA vapor phase. In order to analyze the vapor phase calibration data Eq. (18) was employed as shown below

$$S_f = [\eta\beta\Omega/4\pi][\phi_f^0][I_0 b^{-1} (1-\exp[-\varepsilon cb])]$$

The fluorescence intensity per laser pulse collected by each pixel of the detector array is proportional to the overall efficiency of the optics and detector, quantum efficiency of the monomer, and the total number of excited-state species molecules. If all excitation and detection parameters are kept constant, and assuming that the quantum efficiency of monomer is constant, then the normalized fluorescence intensity by laser excitation intensity and detector gain is only a function of species concentration,

$$S_f \propto 1-\exp[-\varepsilon cb]$$

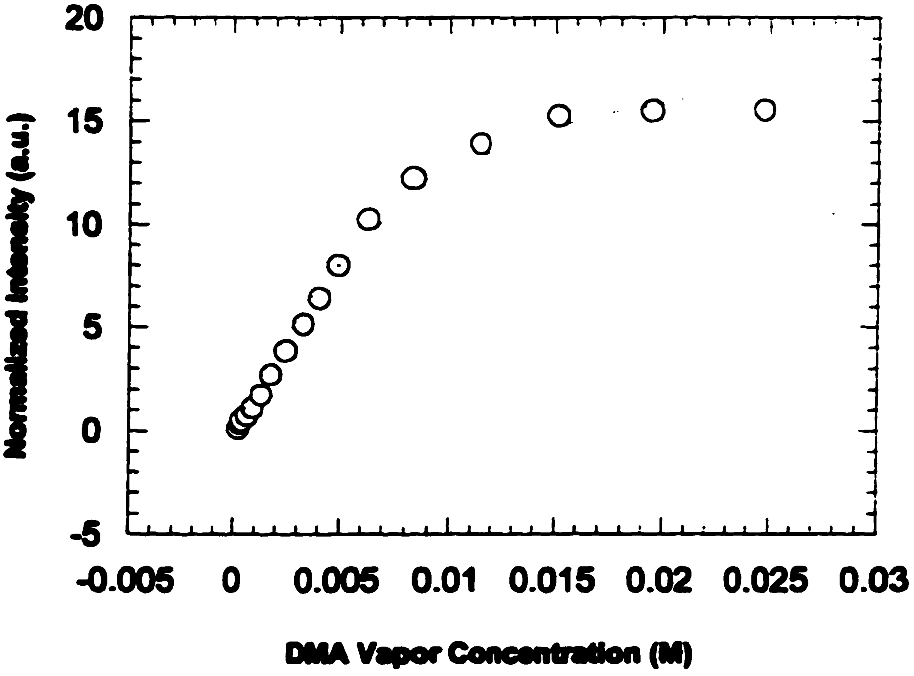

Figure 50. A plot of fluorescence intensity versus concentration of DMA monomer. The data points were fitted to Eq. (17) (solid line).

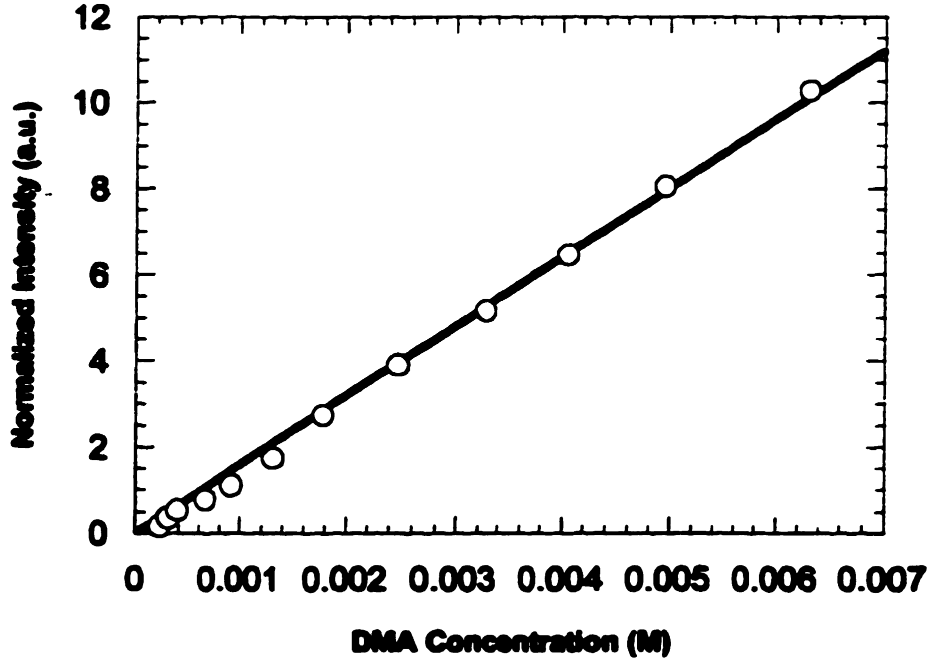

Figure 51. Fluorescence intensity as a function of DMA vapor concentration

If [εcb] << 1, the normalized fluorescence intensity $S_f \propto \varepsilon cb$. Therefore, at small concentrations of the monomer species, the normalized fluorescence intensity (S_f) should be linear to the species concentration. Figure 51 shows only the low concentration part and proves well the linearity of the normalized fluorescence intensity with respect to the species concentration. The slope of the calibration curve is 1.6×10^3(counts/M/pixel). The vapor phase concentrations of DMA are more uncertain at the lower concentration. In this region the pressure is small, and small inaccuracies could lead to large relative errors.

d. Comparisons and discussions

The relationship between vapor phase temperature and pressure can be expressed with the Clausius-Clapeyron equation,

$$\ln P = -\left(\frac{L_{12}}{RT}\right) + C$$

where P and T are gas vapor pressure and temperature, R and L_{12} are gas constant (*8.31 J/mol K*) and latent heat of vaporization, respectively. The vapor pressure of DMA as a function of temperature is shown in Fig. 52. The plot is $-\ln(P_{dma}/P_{atm})$ versus 1/T(K), and includes the direct vapor pressure measurements of this work indicated as (C), and pressures calculated from Melton's analysis of absorption measurements are shown as (A) (i.e., Rotunno et al.[62] determined vapor pressure of TMPD by measuring the absorption of TMPD as a function of temperature at 266 nm through his cell, and using the value of TMPD absorption coefficient (ε) given by Berlman,[66] where the absorption

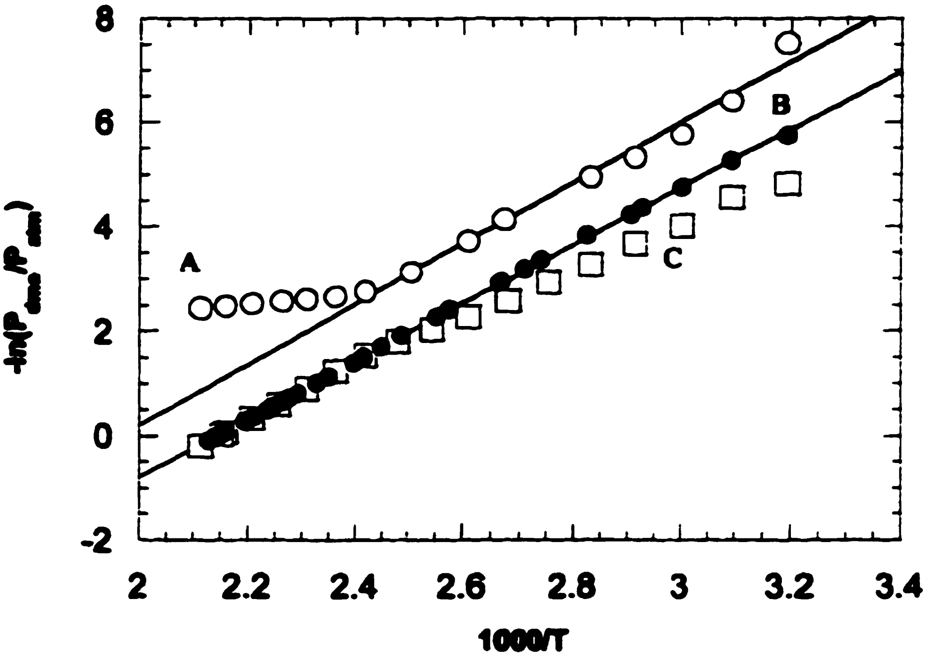

Figure 52. DMA vapor pressure - temperature relationship: (A) is from absorbance measurement using Melton's method, (B) is the reference data,[130] and (C) is from the direct pressure measurement. The solid line is the linear regression based on Clausius-Clapeyron equation.

coefficient was provided in cyclohexane solution and room temperature). (B) is the reference data cited from CRC handbook[130] to compare with the measurement. The straight line is the data fit using the Clausius-Clapeyron equation. The value of x at $y = 0$, i.e., $-\ln(P_{dma}/P_{atm}) = 0$, is the boiling point, and the gradient is proportional to the latent heat of vaporization. At high temperature the measured data were well matched to the reference data; however, a deviation at low temperature was revealed. This is attributed to inaccuracies in the pressure sensor, especially at low temperature. In this region the pressure is small, and small inaccuracies could lead to large relative errors. Based on the Clausius-Clapeyron equation, the direct pressure measurement was more accurate. The pressure measurements from the direct method give much higher vapor pressures than those of absorption measurements. In addition, at temperatures higher than 140° C, data (A) deviate much from the linear fit equation and tend to saturate. Probably this is due to the absence of the liquid DMA. It appears that the most likely cause of the discrepancy was an incorrect value of the molar absorption coefficient of DMA similar to the case of TMPD assumed by Melton. This is perhaps due to the fact that the value used was for DMA in a solution of cyclohexane solvent, whereas the direct pressure measurement here was in the vapor phase. Furthermore, since the molar absorption coefficient (ε) is a characteristic of the solute and depends on the wavelength of the excitation light, the solvent, and the temperature,[79] it may yield erroneous results for vapor concentration which depends on temperature in the measurement. In fact, the absorption coefficient (ε) of liquid DMA in an isooctane solvent was found to be 1.5×10^3 ($L\ mol^{-1}cm^{-1}$), however, the absorption coefficient based on direct pressure measurement was 490 ($L\ mol^{-1}cm^{-1}$). Felton et al.[64] measured the vapor pressure of TMPD as a function of temperature and found a serious discrepancy, nearly four times higher than the absorption measurement conducted by Melton. The method used by Felton et al. for vapor pressure measurement of TMPD is the same as conducted in the present study and is much closer to an estimate based on the Clausius-Clapeyron equation, using the latent heat of vaporization from Trouton's rule. Using the fitting constant from the Clausius-Clapeyron relation, the boiling point of DMA from the direct-pressure measurement can be calculated as 193.5° C. This is in good agreement with the known value [132] of 193~194° C. Also, the latent heat of vaporization can be calculated as 11.04 (*kCal/mol*). Using the absorption data, the boiling point of DMA is overestimated at 235.7 °C with a latent heat of vaporization of 11.52 (*kCal/mol*). Based on this argument, the direct pressure-temperature method is preferred for accurate measurement of the vapor phase concentration. Figure 53 shows the Clausius-Clapeyron relation of the exciplex forming dopants; 1,4,6-TMN (A), DMA (B), and isooctane (C), respectively. The boiling points of individual dopants as well as latent heats of vaporization are given in Table 6. The resultant data fit was made by using only high temperature parts of the measurements because of the inaccuracies in low temperature region.

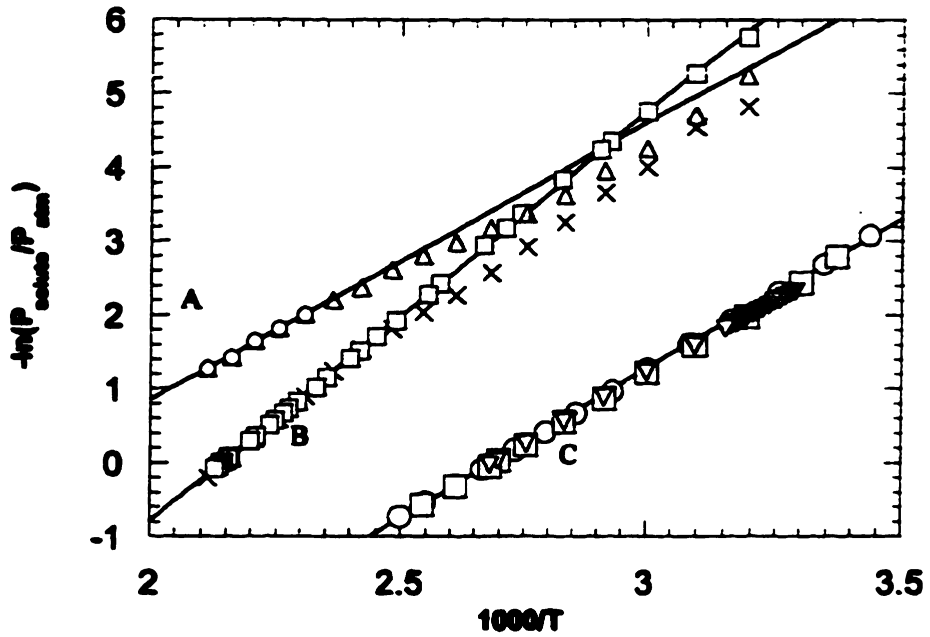

Figure 53. The Clausius-Clapeyron relation of the exciplex forming dopants; (A) 1,4,6-TMN, (B) DMA, and (C) isooctane, respectively

Table 6. The boiling points of individual exciplex-forming dopants and the latent heat of vaporization. Those values were calculated by using the Clausius-Clapeyron Eq.

	DMA	1,4,6-TMN	Isooctane
Boiling Point (B.P.)	193.5° C (193-194)	291.1° C	99.3° C (99)
Latent Heat of Vaporization (*kCal/mol*)	11.04	7.463	8.083

* The parenthetical term is the known value.[132]

B. Liquid Phase

In the liquid phase calibration, the same experimental set-up was used as shown in Fig. 35, except for some minor changes. The bandpass filter for the vapor phase fluorescence changed with the long-pass filter (LL-400-S Corion Co.) for the liquid phase fluorescence. The heating chamber and sample cuvette were replaced with the droplet generator. All optics and detection parameters for the image acquisition were kept constant. With this configuration, the overall efficiency of the optics and detector would be the same as the vapor phase calibration. The droplet volume (V_d), generated from the droplet generator, can be calculated by $V_d = F / f$ where F is the bulk flow rate and f is the production frequency. By substituting the formula for the volume of a sphere, the droplet radius (r_d) can be expressed as $r_d = (3F / 4\pi f)^{1/3}$.

Figure 54 shows the liquid phase calibration data with normalized droplet intensity with respect to droplet mass. It was noted [62] fluorescence from droplets of differing size should be proportional to the droplet mass provided that the droplets are optically thin. However, the droplet sizes used in this development were 90-180 microns, and the corresponding optical densities (optical density (D) = absorption coefficient (ε) × sample concentration in droplet × pass length (droplet diameter)) were well above 3; thus the droplets were not optically thin. Therefore, a decrease in the fluorescence capture efficiency with increasing optical density is expected. Additionally, droplets in this size range cannot be uniformly illuminated by a laser beam whose FWHM is 800 microns. If the droplets are randomly distributed in the beam, some will be more fully illuminated than others. A possible reason for this may arise from the light

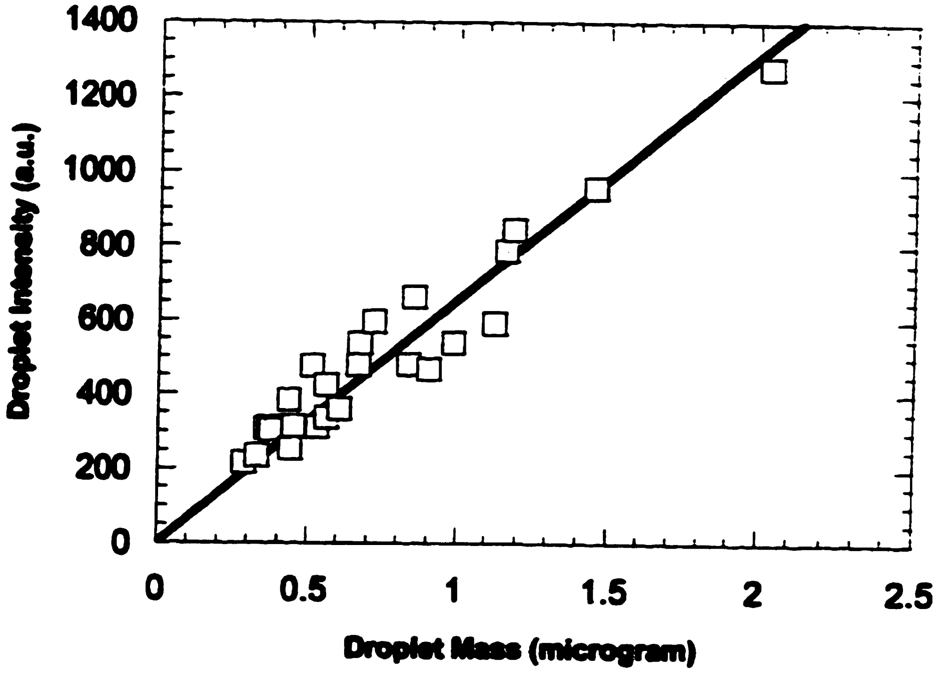

Figure 54. Fluorescence intensity as a function of droplet mass.

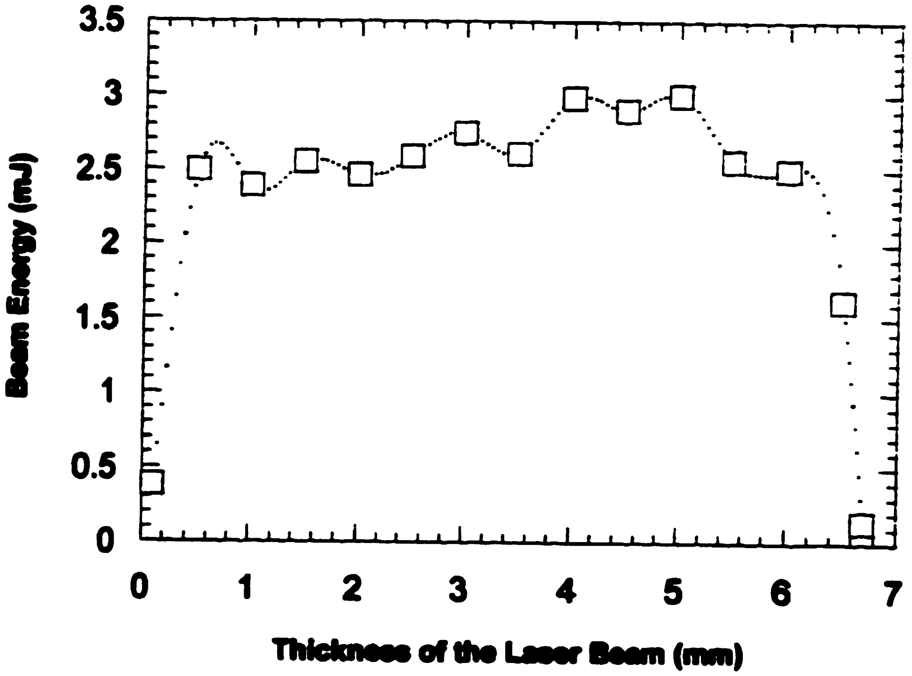

Figure 55. Laser beam intensity profile

intensity distribution across the thickness of the laser sheet as shown in Fig. 55. Although the sheet was quite thick (about 800 microns), its intensity profile was not smooth, so very small misalignment of the brightest part of the sheet relative to the drops might be enough to cause the erratic results. A more reliable approach might be to take many calibration images, scanning the sheet in very small increments across the droplet stream, and taking the maximum intensity as the appropriate one. This would ensure that the droplets were in the same part of the sheet for every point in the calibration. Nevertheless, the measured fluorescence intensity versus droplet mass showed a good linear relationship. In fact, the liquid phase calibration was not influenced by the droplet absorption of excitation light but rather related to the mass of droplet. One of these reasons probably can be explained by the *saturation*[133] of the fluorescence. With a very high excitation as the case in this study, it is possible to approach saturation conditions for fluorescence in which a significant fraction of the solute molecules is in the excited state. It can be shown that the fluorescence signal is related to the incident irradiance $(E_p)_0$ in photons $cm^{-2}\ s^{-1}$ by

$$E_f \propto ck_f \{\ 1+ k_f / [\sigma(\lambda)(E_p)_0\phi_f]\ \}^{-1} \qquad (49)$$

where k_f is the rate constant for fluorescence emission in s^{-1} and $\sigma(\lambda)$ is the absorption cross section (cm^{-2}); $\sigma(\lambda)$ is related to the molar absorptivity by

$$\sigma(\lambda) = 2.303\varepsilon(\lambda)/N = 3.82 \times 10^{-21}\ \varepsilon(\lambda)$$

where N is Avogadro's number. Eq. (49) predicts that a plot of E_f vs. incident irradiance will reach a plateau. Figure 56 shows the saturation curve for the fluorescence of 5%DMA•5%TMN in 90% isooctane exciplex system with respect to laser energy (or

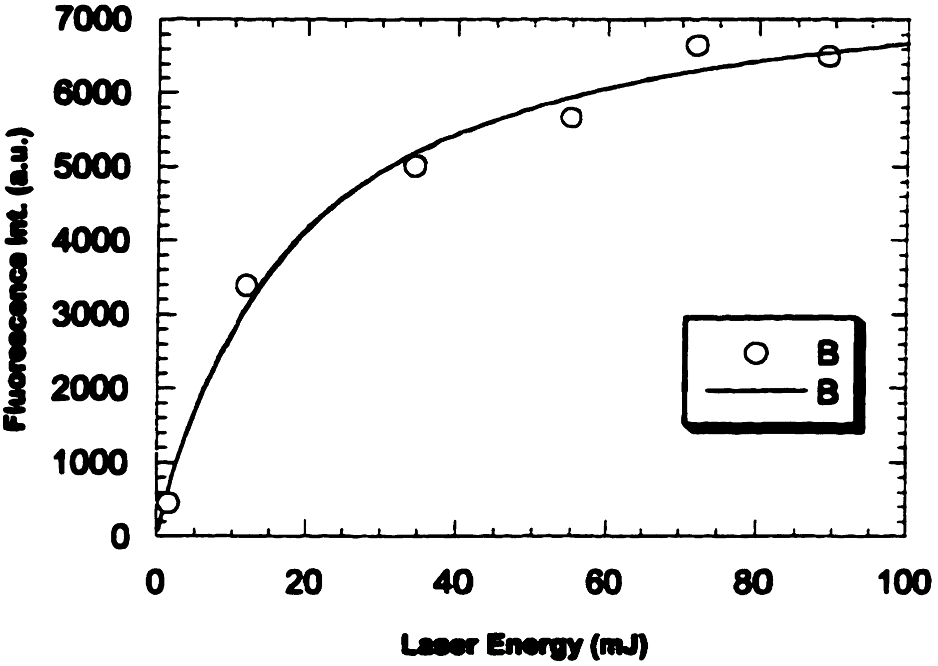

Figure 56. Saturation curve for the fluorescence of 5%DMA•5%TMN•90% isooctane exciplex system versus laser energy. Exciplex liquid stream (50μm in dia. 20.6mm long) was excited with 308(nm) from Excimer laser. The DMA number of moles is approximately 8.8526 x 10^{-9} in that volume.

irradiance) from 308 nm excitation. The solid line is the actual data fit using Eq. (49). The number of moles of the solute within the excitation volume in Fig. 56 can be calculated to be 8.853×10^{-9} and higher than those of droplets used in the liquid phase calibration (i.e., the highest droplet diameter used in this study is 180 μm and it corresponds 0.67×10^{-9} (mole)). Therefore, all droplets in this study are in the region of saturation with high laser excitation. At low irradiances such as achieved with conventional sources, the second term in the brackets in Eq. (49) dominates and $E_F \propto c(E_p)_0 \phi_F \varepsilon(\lambda)$ as discussed in vapor phase calibration. At very high irradiances, the second term vanishes. Under these conditions the fluorescence signal is independent of the source irradiance, fluorescence quantum efficiency, and the molar absorptivity $\varepsilon(\lambda)$ because the rates of stimulated absorption and emission are balanced. Thereby, the fluorescence intensity only depends on the concentration of solute (i.e., volume of the droplet). In addition, nonradiational deactivation becomes negligible. The absorbance decreases with increasing irradiance because the ground-state and excited state population are equalized. Working under saturated conditions provides several advantages: E_F is independent of the source intensity fluctuations and the environment of the molecules (e.g., the effect of the quenchers), and nonlinearities due to primary absorption effects and due to secondary absorption effects are reduced or eliminated.[133] The slope of the line, which was the liquid phase calibration constant, was 6.56×10^2 (counts/droplet image/μg). This slope was probably accurate within ± 15% due to the laser intensity profile.

4.4. Experiment for actual measurements

4.4.1. Fuel spray LIEF imaging in a test-quartz cylinder

A. Fuel LIEF method

The Laser Induced Fluorescence (LIF) image under certain conditions can be interpreted quantitatively, with the fluorescence intensity proportional to the mass of fuel present in the laser light sheet. LIF involves absorption of light followed by spontaneous emission. In previous LIF studies of fuel distributions in flames or engines, other researchers have used fuels of pure ketones or acetaldehyde; conventional fuels doped with a ketone, with acetaldehyde, or with toluene; or undoped commercial-grade fuels (i.e., gasoline).[134] However, the fluorescing components of commercial grade gasoline have not yet been fully identified. In the present LIF imaging, an Aldrich commercial-grade N,N-dimethylaniline (DMA) was used as a fuel dopant in a spectrophotometric grade isooctane which is served as a gasoline fuel. For the two-phase fuel spray visualization, DMA•1,4,6-TMN exciplex system was employed. The fluorescence intensity should be correlated to the number of the fuel molecules, whether they are present as liquid or as vapor phase.

B. Experimental setup

Figure 57 is the overall schematic experimental set-up for the sequential fuel LIF imaging using image acquisition system, fuel injection system and appropriate field optics. The image acquisition systems are consisted of ICCD camera, FG-100 pulse generator, ST 130 Controller and Computer. All necessary information for the image

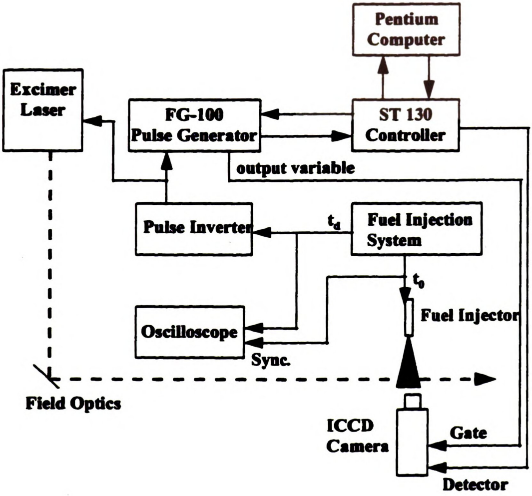

Figure 57. A sequential schematic diagram of fuel LIF image acquisition experimental setup.

acquisition, such as, camera exposure time, image pixel size and number of acquiring image frame, synchronization with excimer laser, were previously memorized by the image acquisition software (CSMA) in the computer hard disk through the FG-100 pulse generator and ST 130 controller settings. Fuel injection systems for 2.4 L direct injection gasoline engine were provided by Chrysler for the study of liquid and vapor phase fuel distributions in internal combustion chambers. This system consisted of fuel injector and delay generator box, which provided fuel injection signal out (t_0), delayed signal out (t_d), fuel injection duration, and fuel injection frequency. Except for the fuel injection signal out, all output signals could be adjusted with a 10-turn potentiometer, thereby the required experimental parameters could be easily set up. A Tektronics 100 MHz digital oscilloscope was used to monitor the delayed signal out.

The spectrophotometric grade isooctane solvent is typical of a gasoline fuel. Pure isooctane solvent does not absorb UV-VIS light, therefore, for the fuel LIF imaging a seed is necessary to provide the fluorescence emission with the UV- laser excitation. For the fuel LIF imaging, N,N-dimethylaniline (DMA) was used as the fuel dopant. There are two reasons for this choice. First, the DMA has a high quantum efficiency ($\varphi \approx 0.11$), therefore, its relatively high fluorescence emission intensity makes it easy to visualize fuel distribution. Second, we already developed visualization systems based on DMA and TMN-isomers with an isooctane-based fuel. This preliminary experiment was the first step to check the LIF imaging acquisition and the validity to use the DMA•TMN-isooctane exciplex system for two phase fuel visualizations. For quantitative application of the fuel vapor and liquid visualization using a LIEF technique, 5%DMA•5%1,4,6-TMN exciplex system was employed in an isooctane solvent. A Nitrogen environment was provided inside the quartz cylinder to protect against fluorescence quenching due to oxygen during the experiment. The fuel injector was continuously fired at a repetition rate of 10Hz and produced two pulses; one for fuel injection (t_0) and the other for image acquisition at a time delay (t_d) with respect to the fuel injection time. Fuel injection duration was set to 4.0 ms. The excimer laser is externally synchronized with the delayed signal out (t_d) of the fuel injector. For the experiments performed with a continuous wave laser, the gate duration controlled the exposure time. Gate duration was varied between 2.5 μs and 11 μs. However, for the measurements using the pulsed excimer laser, with a 18 ns pulse duration and approximately few ns fluorescent lifetime, an extremely brief exposure time which is independent of the camera gate duration was achieved. With this condition the acquired images are "frozen". Since the exposure time of the ICCD detector was set as 1.0 sec during the measurements, each acquired image frame is exposed to 10 laser shots. For this study, we set the delayed signal out (t_d) from 0 to 5.04 ms as an increment of 0.56 ms or 0.11 ms to mimic 600/1500 rpm engine cycle as an 2°/1° crank-angle degree interval, respectively.

A detailed schematic diagram of the fuel LIF imaging field-optics setup is shown in Fig. 58. A pulsed excimer laser, 308 nm (XeCl), is the excitation source, with a maximum power of 150mJ/pulse at a maximum repetition rate of 250 Hz. The laser beam is formed by two pairs of cylindrical fused silica lenses into a sheet of light approximately 800 μm thick by 50 mm high, directed into the quartz cylinder. To minimize reflection losses, all mirror and lenses were anti-reflection (AR) coated. The sheet of light passed through the center of the fuel injector which was located at the center of cylinder axis. The fuel fluorescence emission was imaged by a quartz camera lens (Nikkor UV lens, 50 mm, f/11) onto an ICCD camera, which is a digital, computer-controlled image acquisition system (Princeton

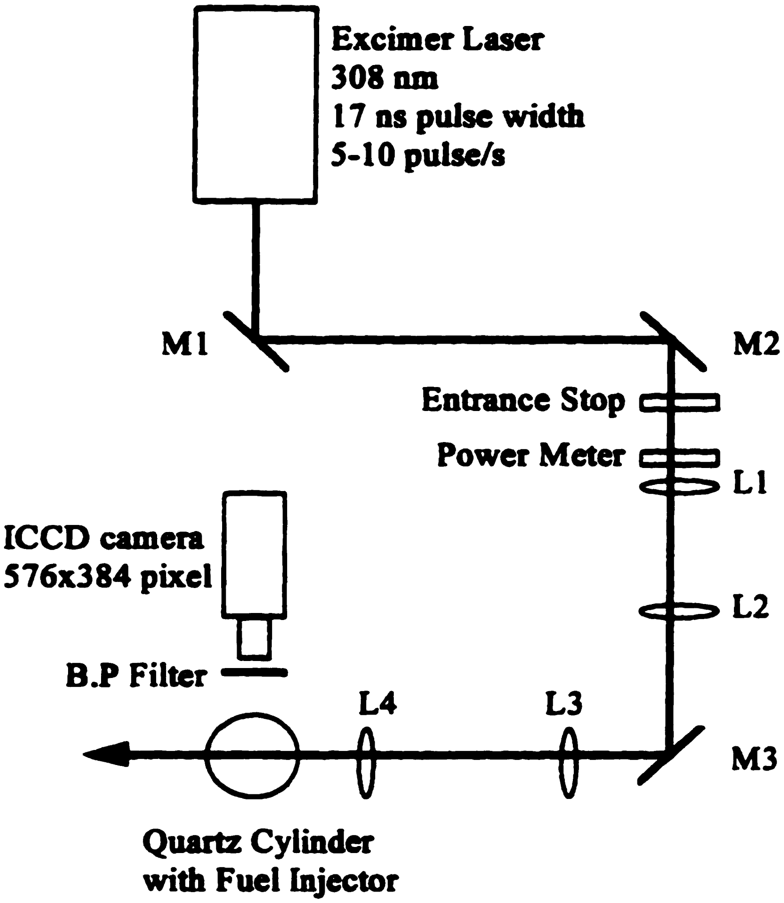

Figure 58. Schematic diagram of fuel LIF imaging field-optics, including fuel injector and optically accessible quartz cylinder. The final beam steering mirror (M3) moves the laser sheet through the quartz cylinder.

Instruments) equipped with a gated image intensifier. The Princeton Instruments camera has a high dynamic range (16-bit digitization), low noise (cooled detector to minimize dark count and slow readout to minimize readout noise), wide spectral sensitivity (180-800 nm), high quantum efficiency (≥12% at 300 nm), adjustable gain (≤1 to 100 counts/photoelectron), and adjustable electronic gating (3.5 ns to 80 ms). One disadvantage of the camera system is its relatively modest spatial resolution, which is limited by the 576x384-pixel detector and further reduced by a factor of 2 or 4 by the fiber-optic-coupled intensifier. Another disadvantage is the long image-readout time (about 5s for an unbinned full frame), so no more than one image can be obtained per injection. The CSMA software can produce mono chrome (gray-scale) images. However, false-color processing (assigning a color to correspond to an intensity range) is often used for image enhancement. In our application, each pixel in the image corresponds to a bin by 2. For in-cylinder fuel LIF imaging, the fuel injector, laser and camera gate were all electronically synchronized to acquire the image at a specified delay time after fuel injection. The fuel injector was typically fired continuously for 20-30 seconds before starting data acquisition, and typically either five 10-laser-shot averaged images or up to 50 individual images were taken, transferred to computer memory, and written to disk. With this configuration, only one image could be taken per fuel injection. Since oxygen is a good fluorescence quencher for aromatic hydrocarbons, the experiments were done in a nitrogen environment.

4.4.2. In-cylinder fuel LIEF imaging in a motored-engine

A. Engine assembly & optical chamber

The engine assemble consists of a single cylinder motored engine with an elongated piston containing a quartz piston crown. On top of this is mounted a 2.4 liter 4 cylinder direct injected Chrysler head where only one combustion chamber was being used. A separate intake system was designed to deliver a preheated atomized mixture to the engine for the calibration. All tests using this experimental setup were run at a motored speed of 600 rpm with a wide open throttle (W.O.T.). The base engine is an AVL 530 diesel crankcase and cylinder. This has been refitted with a 100 mm stroke crankshaft which matches the stroke of the cylinder head being used. The advantage of using this engine is that it provides a balanced rotating and reciprocating mass. This crankcase is also fitted with an additional flywheel which adds additional inertia to keep a constant rpm for a single cylinder. The cylinder head is a 2.4 liter double overhead cam Chrysler direct injection prototype. It contains four valves, two spark plugs, and a centrally located high pressure prototype injector as shown in Fig. 59.

In this experiment, only the number two combustion chamber was used. An optical combustion chamber including Chrysler engine head, quartz cylinder, elongated piston and ICCD detector is shown in Fig. 60. The lifters of all other cylinders have been removed so as only to actuate the required valves. The cylinder head was mounted above the AVL engine on two supports and a quartz cylinder and steel spacer was placed in between. The bore and stroke of the combustion chamber are 3.444", and 3.937", respectively. This gives a single cylinder displacement of 0.8 liters and a compression ratio of 9.4 to 1. The quartz cylinder was made of GE 124 fused quartz, which has a transmission of 92% in the range of UV light

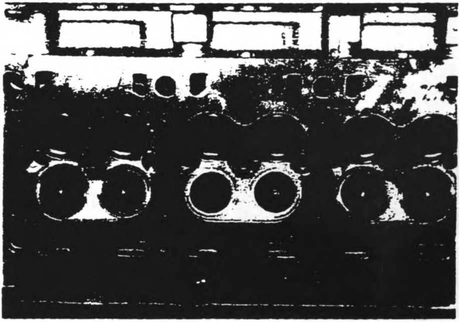

Figure 59(a). The Chrysler 2.4 L double overhead cam direct-injection engine head.

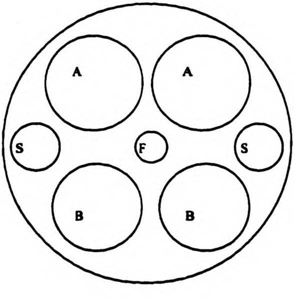

Figure 59(b). A schematic diagram of the 2.4L Chrysler engine head showing two intake (A), and exhaust (B) valves. Fuel injector is located in the center (F), and two spark plugs are situated in the left and right corners (S).

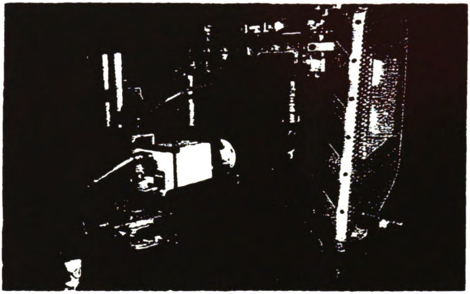

Figure 60. Image acquisition experimental setup for actual measurements in real engine operation. Chrysler engine head, field - optics (left side), ICCD detector, optical quartz chamber including mirror and piston, and AVL engine are shown.

that is used. The cylinder was 10 mm thick, which provided enough strength without losing laser power. The piston extension, which is a hollow tube with a slot cut in one side for access of a stationary mirror, was bolted directly to the top of the AVL piston. This was machined from billet 70705 T651 aluminum for a high strength to weight ratio. The piston extension contains a quartz piston crown and Rulon® rings. This material is a fluoropolymer with a low coefficient of friction. It also has a temperature range of (-400F to +500F). These properties make a well-suited sealing material for the quartz cylinder. The quartz piston is also made of GE 124 fused quartz and is 1.78 cm thick. This quartz piston crown makes up about 65% of the piston top. This makes it possible for large portions of the combustion chamber to be viewed at times when the piston is close to Top Dead Center (TDC). This is the maximum that can be used because of the need for piston ring lands. The mirror that was used to gain access to the combustion camber is a first surface mirror with UV enhanced aluminum coating for good UV light transmission, which was purchased from Edmund Scientific. The mirror is an ellipse mounted at a 45 degree angle with the axis of piston motion as shown in Fig. 61. This allows a plane view of the cylinder through the quartz piston. The double overhead cams of the cylinder head are driven by a power takeoff from the AVL, via single gear belt pulley. For alignment purposes, extensions were added to the camshafts. This entire assembly was motored by a 15 horsepower variable speed direct current motor. The oiling of the cylinder head is separate from the crankcase oiling system of the motored engine. The reason for this is the head does not sit at the same angle it was designed for which creates oil draining problems. An oil pump draws oil from a reservoir and supplies oil to an inlet passage in the head. A pressure switch monitors the oil supply and if the pressure drops below a set point, shuts the pump off. Oil draining of the head is

Figure 61(a). A picture of surface mirror mounted at a 45° angle with the axis of piston motion.

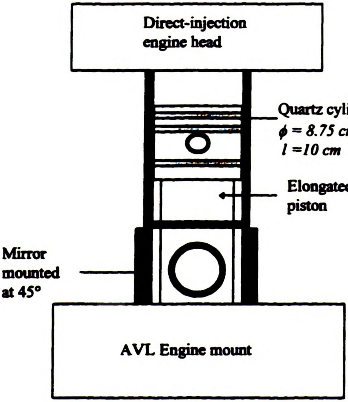

Figure 61(b). A schematic diagram of a side view of optical chamber (above); elongated piston, surface mirror and quartz cylinder are shown.

accomplished by applying a slight vacuum to return lines installed in the return passages of the cylinder head.

B. Intake system

A special intake system for the exciplex calibration and direct injection tests was needed because of the quenching of the exciplex fluorescence by oxygen. This system also needs to be able to measure the mass flow rate of nitrogen and fuel, and create a homogeneous mixture for the calibration. The intake system for the calibration of the exciplex vapor phase consists of a nitrogen balance system, laminar flow element (LFE), intake heater assembly, fuel injection and mixing zone, and an intake plenum. Similar homogenous charge mixing systems have been developed in the past for emission testing of small engines and a similar design was chosen for this. The intake system for the in-cylinder direct injection measurements is similar to the calibration setup except the heater and injection systems are bypassed.

The nitrogen balance system works like an accumulator. It consists of a 55 gallon container with a plastic diaphragm acting as a flow balancing device. Nitrogen is delivered from compressed nitrogen tanks through regulators to the bottom of the container. The outlet is via the top through a 2 inch diameter flexible hose. The nitrogen is next drawn into the laminar flow element which measures the mass flow rate.

The laminar flow element is Model 50mh10-1 ¼ from Meriam Instruments. It is rated at 17.0 SCFM and 8 inches of water differential. This was mounted between an up steam tube length of 15 inches and a downstream length of 7 inches to ensure laminar flow. These dimensions correspond to 10 diameter upstream and 5 diameter downstream length, recommend by Meriam to ensure accurate readings. The differential pressure ports were connected to a Meriam inclined tube manometer which displayed the flow rate in SCFM. The inclined tube manometer used was model 40HE35 with a maximum capacity of 8 inches of water differential which allows for 17 SCFM to flow through the element.

Next the nitrogen passed through a heater assembly. The heater element consists of a 300-500 watt heat gun replacement element. This heater assemble is automatically controlled by a closed loop thermocouple control unit (API Instruments Co.). This heated air is drawn into an injection chamber where the atomized fuel is introduced. This injection chamber consists of an aluminum block with the nitrogen entering at 90 degrees to the fuel inlet.

The fuel injection system consists of pressurized fuel passing though orifices. The fuel was pressured by nitrogen in a pressure vessel which delivers the fuel at a given pressure without pulsation. The fuel then passes through 7 μm sintered metal filters, a shut off valve, and then the orifices. The orifices were polycrystalline diamond wire extrusion dies produced by Hoosier Wire and Die. The configuration of this orifice is illustrated in Fig. 62. The sizes that provided the necessary flow rate were 0.003, 0.004, 0.005 inches in diameter. Once the isooctane and DMA mixture was injected in to the nitrogen stream the mixture passed though a mixing chamber consisting of spiral wound wire screen of varying mesh size. This chamber was also heated using heating tape and controlled with a Variac to maintain an elevated temperature for liquid evaporation. As a check, a sight glass was put in line to ensure that the mixture was in vapor form, and no liquid fuel was on the walls. This mixture then passed though an insulated tube with a length to diameter ratio of over 40 to ensure fully developed flow and proper mixing. The mixture then entered the intake plenum. This consisted of a 15 gallon tank with pressure and vacuum relief. This proved to provide

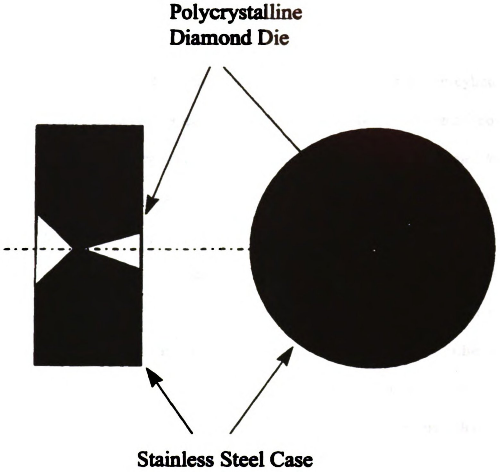

Figure 62. Wire die Orifices.

adequate volume to stabilize the flow for the LFE. The mixture then passed though a straight section of manifold to the intake side of the cylinder head.

C. Direct-injection fuel control & laser synchronization

The control of the fuel to the high pressure injector for the in-cylinder direct injection, was accomplished with a specially designed control box. This control box uses an input from a 360 degree Dynapar shaft angle encoder. This encoder was attached to the cam takeoff of the AVL with a flex coupling. This cam takeoff is geared internally with 2:1 ratio. This allows for the encoder to spin once for every complete engine cycle, two revolutions of the crankshaft. The control box provides a 5 volt TTL signal out for synchronization of the laser and the CCD camera. This signal has sufficient delay to allow the laser pulse and camera to capture an image at any point in the cycle. The fuel injection pulse out signal which is also adjustable anywhere in the cycle is sent to a special control device provided by Chrysler, which operates the high pressure injector. This box also contains a digital readout tachometer for accurate rpm readings. The fuel system that delivers fuel to the high pressure injector is made up of a fuel reservoir from which a low pressure (30 psi) 12 volt pump draws fuel. This low pressure pump primes the high pressure pump which is a roller pump driven by a ½ horsepower electric motor. The system pumps much more fuel than is needed, so a return from the high pressure pump to the reservoir is used.

Chapter V. Results and Interpretations

5.1. 2-D Section of images of fuel spray in a test quartz cylinder

In this section, the optical methods developed in the previous chapters are used to visualize the injection of a liquid spray in an optically accessible quartz cylinder. In Section 5.1.1., the qualitative temporal and spatial distribution of the liquid spray is described. In Section 5.1.2., a quantitative description of the spray visualization is made for both the liquid and vapor phase.

5.1.1. Fuel Spray LIF imaging

In order to simulate a 600 rpm engine environment, atmospheric pressure tests were conducted at 600 injections per minute with a 4.0 ms injection duration in the apparatus described in Sec. 4.4. The injector was fired for three or four preparatory injections, and after that the fluorescence images were recorded. For this LIF image acquisition, the vertical sheet of light passed through the center of the fuel injector. All acquired images had the same experimental conditions except that the delay time t_d was varied. Figure 63 shows nine LIF fluorescence images that display the development of a fuel spray and its distribution in 0.56 ms steps, corresponding to successive 2° crank-angle degree (CAD) intervals at 600 rpm engine speed. Different false color scale assignments were used to encode the spray fluorescence intensities. Figure 64 represents the intensity contour map of total emission fluorescence from the fuel spray. In Fig. 63, image capture was made from 0.56 ms to 5.04 ms after the start of fuel injection, corresponding to 2° CAD and 18° CAD, respectively. At 0.56 ms after the start

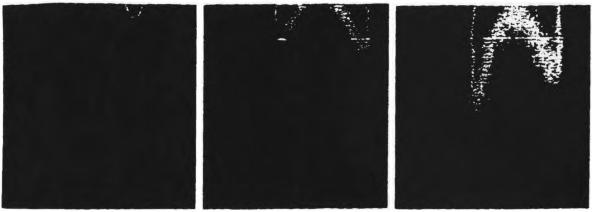

(a) t_d = 0.56 ms *(b) t_d = 1.126 ms* *(c) t_d = 1.684 ms*

(d) t_d = 2.243 ms *(e) t_d = 2.801 ms* *(f) t_d = 3.360 ms*

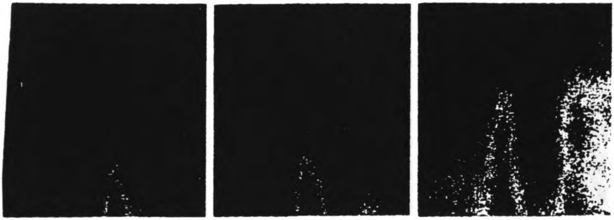

(g) t_d = 3.920 ms *(h) t_d = 4.480 ms* *(i) t_d = 5.040 ms*

Figure 63. Sequential fuel laser induced fluorescence (LIF) images after fuel injection (t_0) (visualization was made by using a 5%DMA/95%isooctane fuel).

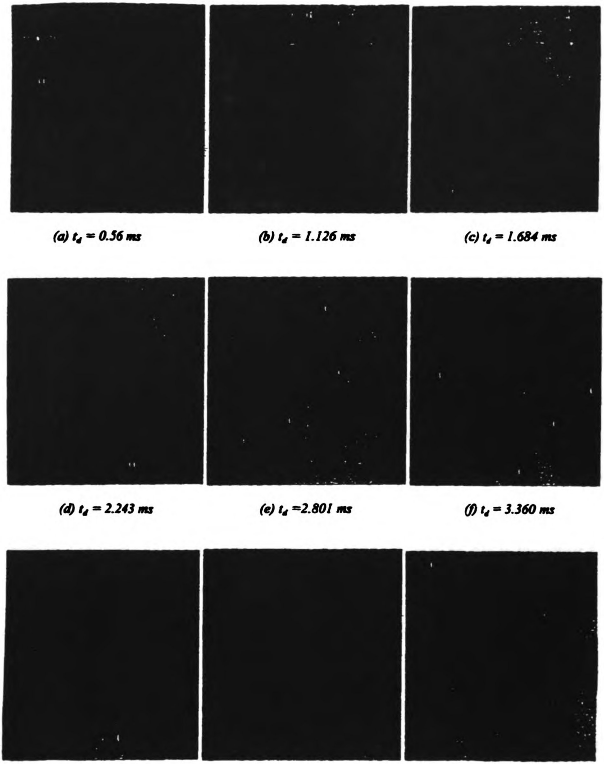

(a) t_d = 0.56 ms *(b) t_d = 1.126 ms* *(c) t_d = 1.684 ms*

(d) t_d = 2.243 ms *(e) t_d =2.801 ms* *(f) t_d = 3.360 ms*

(g) t_d = 3.920 ms *(h) t_d = 4.480 ms* *(i) t_d =5.040 ms*

Figure 64. The contour map of the fuel LIF image intensity in Fig. 63.

of injection, the spray emerged like a bullet with a dense spatial fuel distribution. Most of the fuel resided in the center of the spray core. However, 1.126 ms (4° CAD) later, the situation was quite different. The center core was now divided by two main branches with an included angle greater than 30°. Moreover, its bullet-like fuel distribution was completely changed to a spray cone which had a strong fuel concentration on both sides of the upper part of the cone. However, the central part of the spray injection line was not completely filled, having a much weaker concentration, akin to a hollow cone spray. The liquid fuel on the outer surface of the spray was far from the main liquid stream which was in the center and tended to move apart from it. Moreover, there existed collisions which could produce atomization of fuel droplet in the interface between nitrogen molecules and liquid on the outer surface. Therefore, it was anticipated that liquid phase fuel was predominant in the interior of the spray and fuel vapor was distributed weakly away from the cone. This is a reasonable assumption since vapor can easily develop by atomization and by the vaporization process of the liquid fuel on a droplet's outer surface. The longer tail of the spray on the right hand side may be due to the effect of nitrogen gas flow impinging on the fuel on that side.

The image in Fig. 64c, taken at 1.684 ms (6° CAD) after the start of fuel injection, shows further development of main liquid stream downward, filling the central part of the spray. However, one can apparently observe two branches of main streams. On the leading edge of the spray, a vortex-like motion is developed. This could be due to the vapor phase because the liquid is generally less perturbed by the ambient fluid motion than the gas phase because of its inertia. As injection proceeds, the spray fluorescence is more intense overall, and then shows the highest fluorescence intensity near the injector tip with a value of 0.763 at 2.243 ms after the start of fuel injection as shown in Fig. 64d. It was observed that in the images recorded at times greater than 2.801 ms, the hollow-cone spray collapsed completely, because entrainment of ambient air into the injected jet produced a low-pressure region beneath the injector. Furthermore, the fluorescence intensity decayed with a relatively high concentration toward the bottom of the chamber, as be seen very clearly in Fig. 64.

By mid-injection (up to 2.243 ms) the fuel distribution has become reasonably axisymmetric, and the concentration decreased axially (from top to bottom) and increased temporally (from 1.126 ms to 2.243 ms). On the other hand, images recorded from 2.8 ms after the start of injection showed opposite behavior - a temporal decrease while remaining axially symmetric. Moreover, as the end of injection approached, the intensity distribution became asymmetric. At the end of injection, the overall fuel concentration diminished and the injected fuel spread toward the bottom of the chamber, due to gravity. After mid-injection, a wide fuel distribution could be observed with weaker intensity, probably due to the evaporation of liquid. For example, in Fig. 64f, the third contour map at 3.360 ms after the start of injection had an intensity value of 0.234. As injection proceeded, however, it decrease to 0.073 at 5.04 ms. These features are qualitatively consistent with the effects of evaporation of liquid drops from the periphery of the spray, and possibly more rapid spreading of the vapor by turbulent diffusion. In Fig. 64h and 64i at the end of injection, the overall concentrations were much lower and the image field was filled by the fuel at low concentrations due to the vapor phase.

5.1.2. Fuel Spray LIEF Imaging

We now examine the two-phase distribution of liquid and vapor using exciplex imaging. A quantitative concentration map of the spray is shown in Fig. 65. The spray consisted of the 5%•DMA•5%1,4,6-TMN•90%-isooctane exciplex system. All experimental set-up conditions were the same as the fuel LIF imaging discussed in Section 5.1.1, except the fuel injection duration which was set to 3.0 ms. In order to simulate a 1500 rpm engine speed, the injection frequency was set at 25 Hz, equivalent to 1500 injections/minute. Additionally, two bandpass filters were employed to capture the liquid and vapor phase spray separately. Image capture was made between 0.333 ms and 2.444 ms after the start of fuel injection at steps of 0.111 ms, corresponding to 3° CAD to 22° CAD at 1° CAD intervals. All images of the liquid and vapor phases consisted of averages of 10 individual laser shots. The spray profile was taken at 333 μs after the start of injection.

In Figure 65(a) and (b), images of the liquid and vapor phase spray, respectively, are shown, while Figure 65(c) and (d) shows contour maps of liquid and vapor phases. In Fig. 65(a) and (b), the general behavior of the spray shows a symmetry about the injection line. However, higher fuel concentrations exist in the left upper part of the spray, which is believed to be due to an asymmetry in the fuel injector, especially at higher injection frequencies. In particular, it can be seen that the highest concentrations of the vapor are associated with the highest concentrations of the liquid, i.e., the vapor was evaporating from individual liquid droplets. The general shape of the spray had a high fuel concentration on both the right and left sides of the spray. However, the center part of the spray was not completely filled, apparently forming a hollow cone.

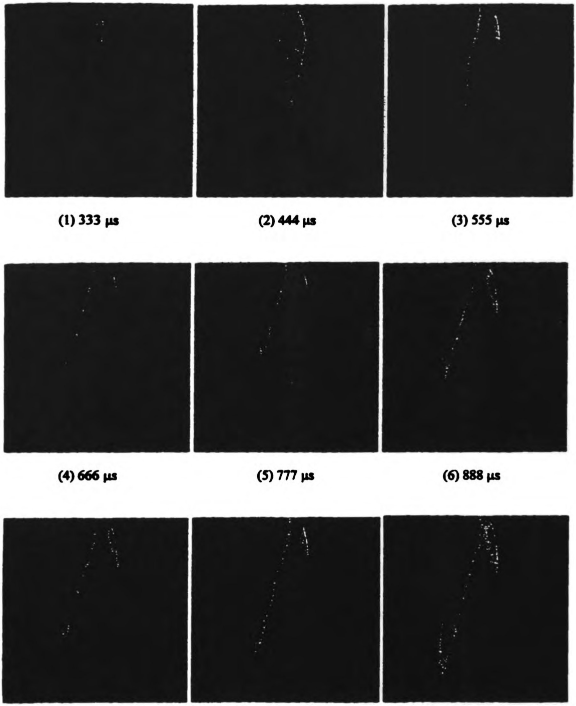

(1) 333 μs

(2) 444 μs

(3) 555 μs

(4) 666 μs

(5) 777 μs

(6) 888 μs

(7) 1000 μs

(8) 1111 μs

(9) 1222 μs

Figure 65(a). Liquid phase fuel spray visualization using a laser induced exciplex fluorescence visualization technique (5% DMA•5%1,4,6-TMN exciplex system was used).

(10) 1333 μs

(11) 1444 μs

(12) 1555 μs

(13) 1666 μs

(14) 1777 μs

(15) 1888 μs

(16) 2000 μs

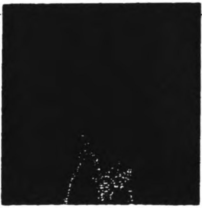

(17) 2111 μs

(18) 2222 μs

(19) 2333 μs

(20) 2444 μs

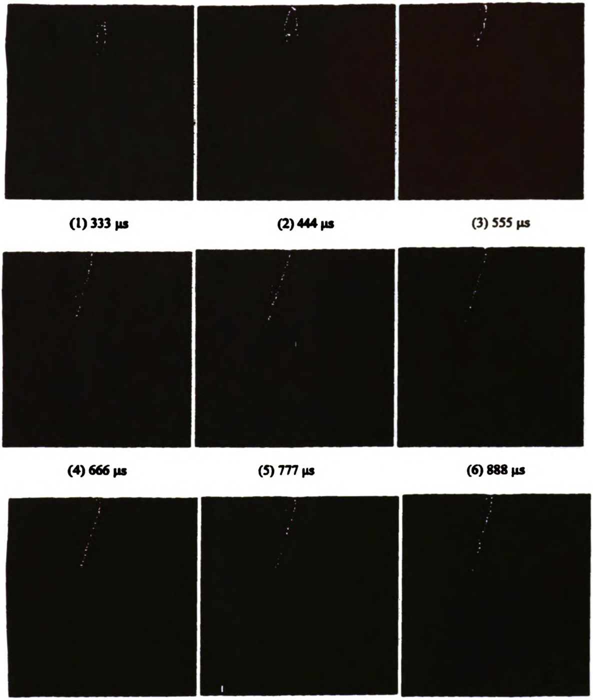

(1) 333 μs

(2) 444 μs

(3) 555 μs

(4) 666 μs

(5) 777 μs

(6) 888 μs

(7) 1000 μs

(8) 1111 μs

(9) 1222 μs

Figure 65(b). Vapor phase fuel spray visualization using a laser induced exciplex fluorescence visualization technique (5% DMA•5%146-TMN in 90% isooctane exciplex system was used).

(10) 1333 µs

(11) 1444 µs

(12) 1555 µs

(13) 1666 µs

(14) 1777 µs

(15) 1888 µs

(16) 2000 µs

(17) 2111 µs

(18) 2222 µs

(19) 2333 μs

(20) 2444 μs

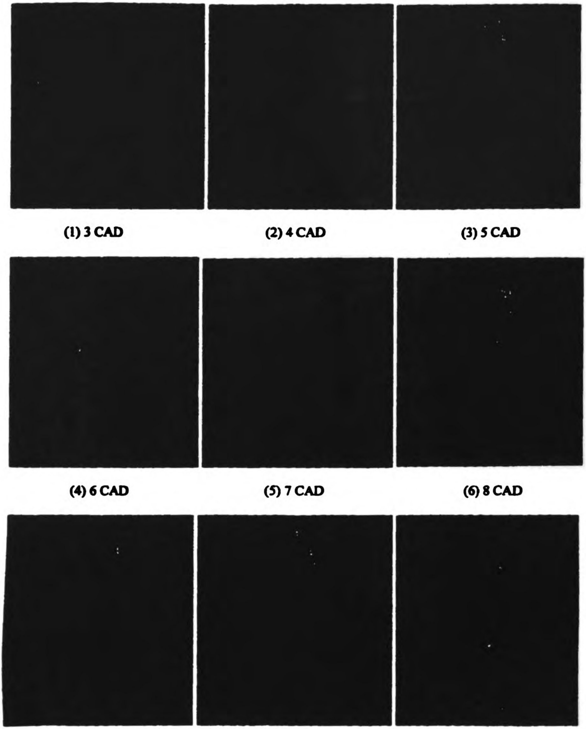

(1) 3 CAD (2) 4 CAD (3) 5 CAD

(4) 6 CAD (5) 7 CAD (6) 8 CAD

(7) 9 CAD (8) 10 CAD (9) 11 CAD

Figure 65(c). Contour map of the liquid phase fuel spray in Fig. 65(a).

(10) 12 CAD

(11) 13 CAD

(12) 14 CAD

(13) 15 CAD

(14) 16 CAD

(15) 17 CAD

(16) 18 CAD

(17) 19 CAD

(18) 20 CAD

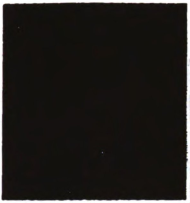

(19) 21 CAD

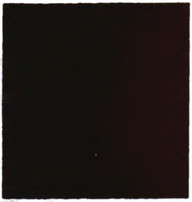

(20) 22 CAD

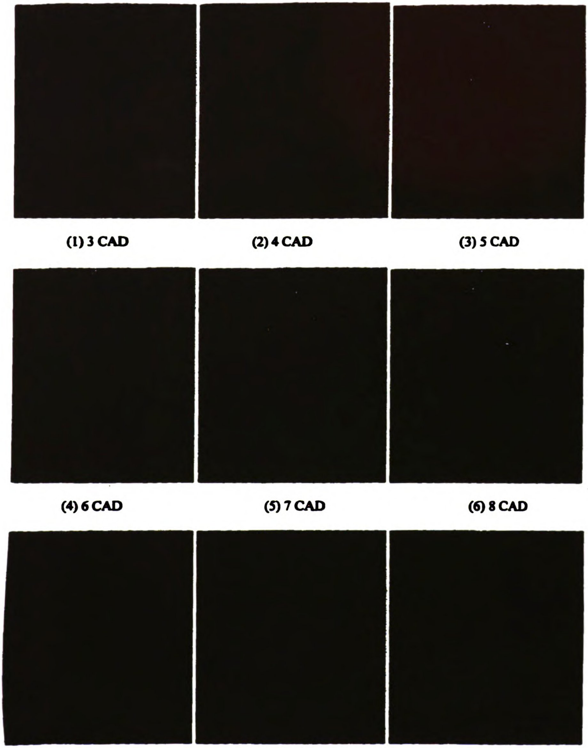

(1) 3 CAD

(2) 4 CAD

(3) 5 CAD

(4) 6 CAD

(5) 7 CAD

(6) 8 CAD

(7) 9 CAD

(8) 10 CAD

(9) 11 CAD

Figure 65(d). Contour map of the vapor phase fuel spray in Fig. 65(b).


(10) 12 CAD


(11) 13 CAD


(12) 14 CAD

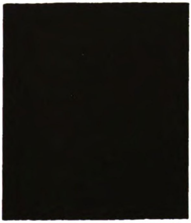
(13) 15 CAD


(14) 16 CAD


(15) 17 CAD


(16) 18 CAD


(17) 19 CAD


(18) 20 CAD

(19) 21 CAD

(20) 22 CAD

In Fig. 65(c) and (d), both the liquid and vapor fluorescence decreased from the injector tip to bottom and also decreased radially from the center line. This probably was partly due to the fast atomization process at the interface between the air and fuel on the outer surface. Generally, the liquid phase fluorescence is 70-80 times higher than that of the vapor phase in most parts of the spray area.

A. Time-dependent analysis of the spray

The temporal evolution of the liquid fuel spray is shown in Fig. 66. The intensity fluctuations in the early stage of injection can be explained by the injector characteristics. Upon receiving an electronic pulse from the control system, the injector opens its valve maximally and stabilizes valve position during the first several hundred µs. Fluorescence intensities were obtained at various axial positions along the injection line (from the injector-tip to the bottom) at different times after start of injection. As time proceeded, the fluorescence intensity of most of the investigated positions increased and reached a maximum near 1.67 ms after the start of injection. Between 0.78 and 1.67 ms, greater fluorescence intensity from liquid fuel spray was observed near the fuel injector tip. In addition, the relative intensity of all investigated positions (or pix.) was increased. However, at 1.78 ms after the start of injection, quite different progressions were observed: high intensity at large distance and low intensity near the injector-tip. As time evolved further, the fuel intensity was decreased gradually keeping their relative features moderately constant. This phenomenon may be explained by assuming the fuel injection consists of two steps: the valve opening and the valve closing process. During the opening process, especially between 0.56 ms and 1.67 ms, fuel concentration

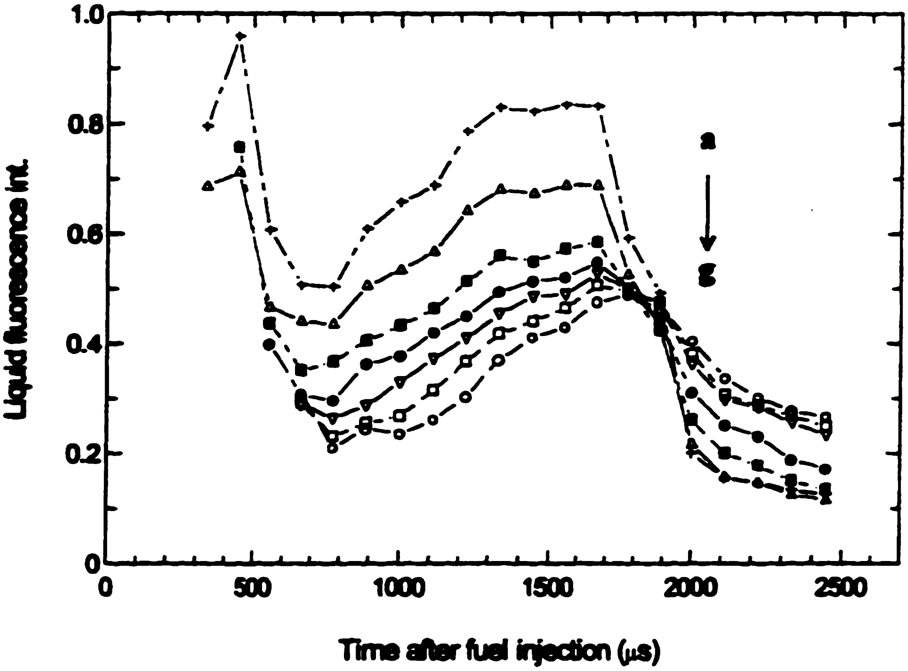

Figure 66. Temporal evolution of the liquid phase fuel spray with the distance from the tip of the injector; (a): 30, (b): 50, (c): 90, (d): 120, (e): 150, (f): 170, and (g): 190 pix., respectively.

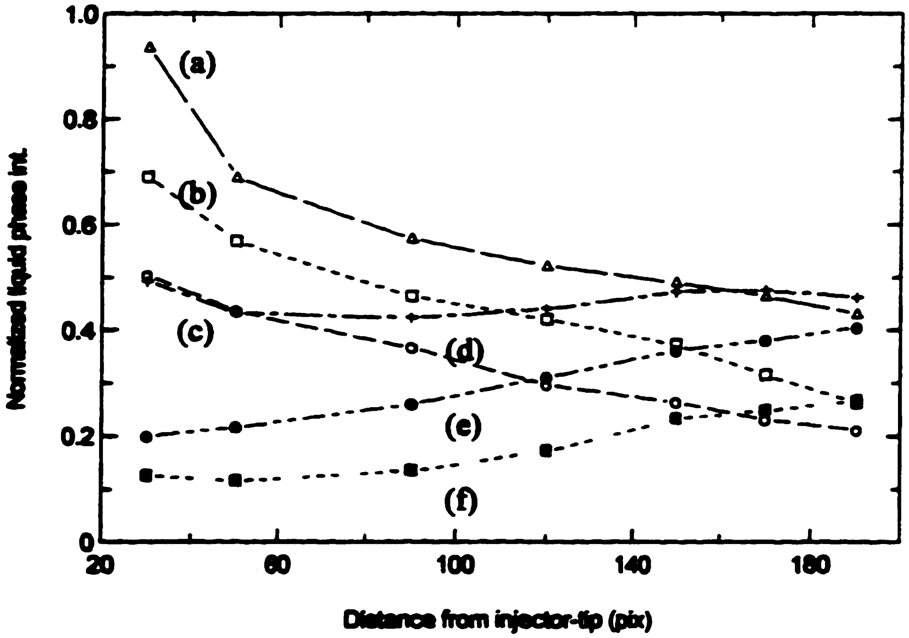

Figure 67. Normalized liquid phase fluorescence intensity with respect to the distance from the injector tip at fixed time after fuel injection; (a): 0.78 ms, (b): 1.11 ms, (c): 1.56 ms, (d) 1.78 ms, (e): 2.0 ms, and (f): 2.44 ms after start of injection.

continuously increased, due to the high liquid mass flow rate resulting from the large inside volume of the injector. However, at 1.78 ms after the start of injection, during the valve closing process, the inside volume of the injector decreases resulting in a relatively small amount of fuel exiting the injector. The reason for relatively higher intensity at far distance (e.g., 190 pix.) in the injection line compared to a near one (e.g., 30 pix.) is possibly due to the reduced fuel supplied from the injector during the valve closing process, and also due to the prior injected fuel which would be moving downward. Figure 67 shows this phenomenon clearly. In Fig. 67, the normalized fluorescence intensity of the liquid was plotted vs. the axial distance from the center of the injector-tip at various times subsequent to injection. Individual data sets of (a), (b) and (c) were taken at 0.78 ms, 1.11 ms and 1.56 ms after the start of injection, respectively, and exhibit the general progression of features during the valve opening process. Data (d), (e) and (f) were taken at 1.78 ms, 2.0 ms and 2.44 ms, respectively, and indicate the general behavior of the liquid spray during the valve closing process.

The *vapor* phase fluorescence intensity and its contour map are shown in Fig. 65(b) and (d). Individual numbers on the contours show the relative intensity normalized by the highest intensity value observed in a liquid phase image taken at 1.67 ms after injection. The spatial and temporal progressions of vapor phase spray are similar to those of the liquid phase. In particular, it can be seen that the highest concentrations of the vapor are associated with the highest concentration of the liquid, i.e., the vapor is evaporating from individual liquid droplets. The temporal behavior of the vapor phase spray at different heights from the center of the injector-tip is shown in Fig. 68. The general features of the spray look the same as the liquid phase. However, the intensity

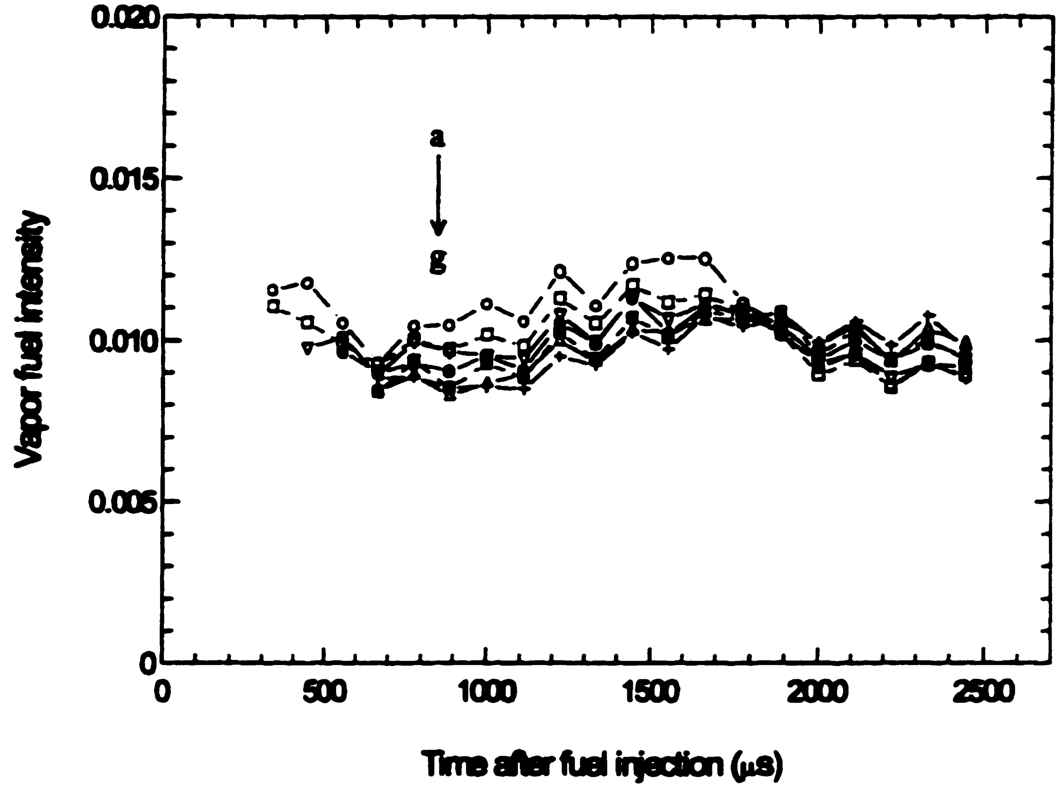

Figure 68. Temporal evolution of the vapor phase fuel spray with the distance from the tip of the injector; (a): 30, (b): 50, (c): 90, (d): 120, (e): 150, (f): 170, and (g): 190 pix., respectively.

was relatively constant with a value of 0.01, much smaller than that of the liquid phase throughout the injection process.

B. Simple model of droplet vaporization

In Chapter 2, vaporization of the liquid droplet through the heat-transfer or mass-transfer controlled case was discussed in detail. There are two models for the vaporization of the liquid droplet given by[95]

$$D_0^2 - D^2 = k_1 t \tag{25}$$

$$-dm/dt = k_2 D^2 \tag{26}$$

$$D_0 - D = k_3 t \tag{27}$$

where D is the droplet diameter at time t, D_0 is the initial droplet diameter, the k_i*'s* are the vaporization constants determined by a combination of physical constants and by the Nusselt number of the droplet, and m is the mass of droplet lost during vaporization. For a relatively large droplet size Eq. (25) can be used, but for small droplets Eqs. (26) and (27) are preffered.

It is assumed that the vaporization behavior of the liquid droplet is mass- or heat-diffusion controlled as described by Eq. (25) or (27) and, further, the measured fluorescence intensity is proportional to the mass of vaporized droplet. This gives the following relationships for the emitted intensity vs. time.

$$t = 1/k_3(D_0 - D) = D_0/k_3(1 - D/D_0)$$

$$t = 1/k_1(D_0^2 - D^2) = D_0^2/k_1(1 - D^2/D_0^2)$$

$$I = k_4(D_0^3 - D^3) = D_0^3 k_4(1 - D^3/D_0^3) \qquad (50)$$

where k_4 is the proportionality constant relating emission intensity to the volume of the vaporized droplet. In order to understand the qualitative features of the emission intensity due to droplet vaporization, all constants in the equation were normalized with 1 ($k_1 = k_3 = k_4 = D_0 = 1$), and D was allowed to vary from 1 to 0. A theoretical curve for both the large and small droplet size is shown in Fig. 69 and 70. If the relationship between vaporization time and droplet diameter are linear as shown in Fig. 70a, then Eq. (27) is a better approximation for the vaporization behavior of small droplets, suggesting mass-transfer control.[95] On the other hand, if the vaporization time is proportional to D^2, as shown in Fig. 70b, then Eq. (1) is a better approximation for the vaporization of relatively large droplets, suggesting mass- and heat-transfer control.[95]

A second approach can be taken toward deducing the relationship between D and t from the emission fluorescence. By assuming the maximum emission fluorescence of the vapor signal I_{max} to be proportional to the initial droplet mass,[95] i.e., $I_{max} = k_4 D_0^3$ and recalling from Eq. (50), that $I = k_4(D_0^3 - D^3)$, the following expression can be reached:

$$D/D_0 = (1 - I/I_{max})^{1/3} \qquad (51)$$

Substitution of Eq. (51) into Eq. (25) results in the following relation:

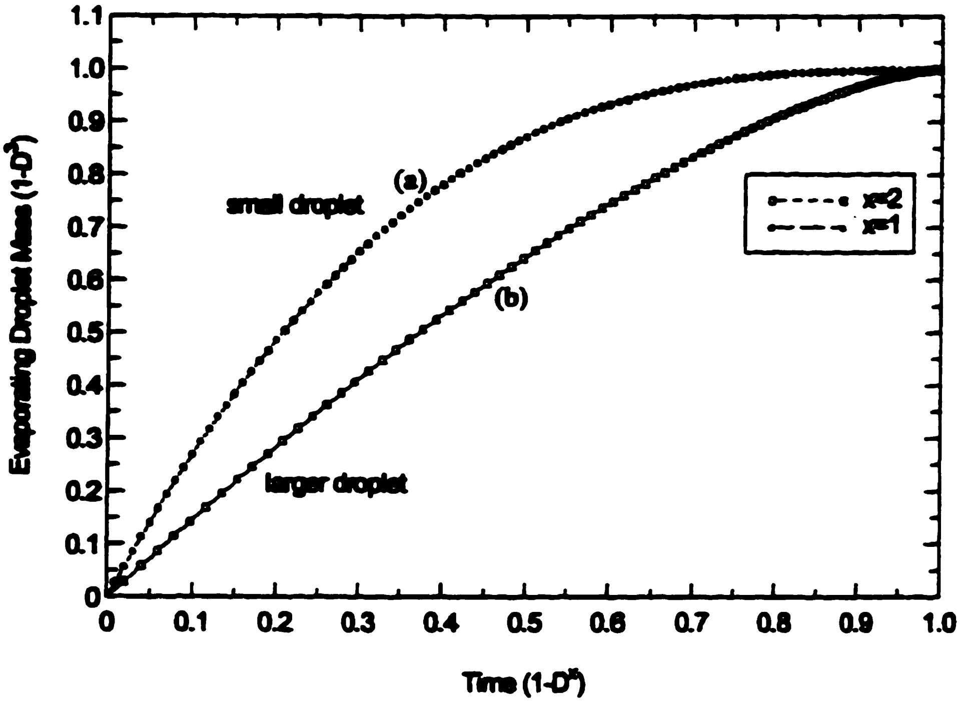

Figure 69. Theoretical calculation of droplet evaporation; [95] (a): small droplet, (b): large droplet, respectively.

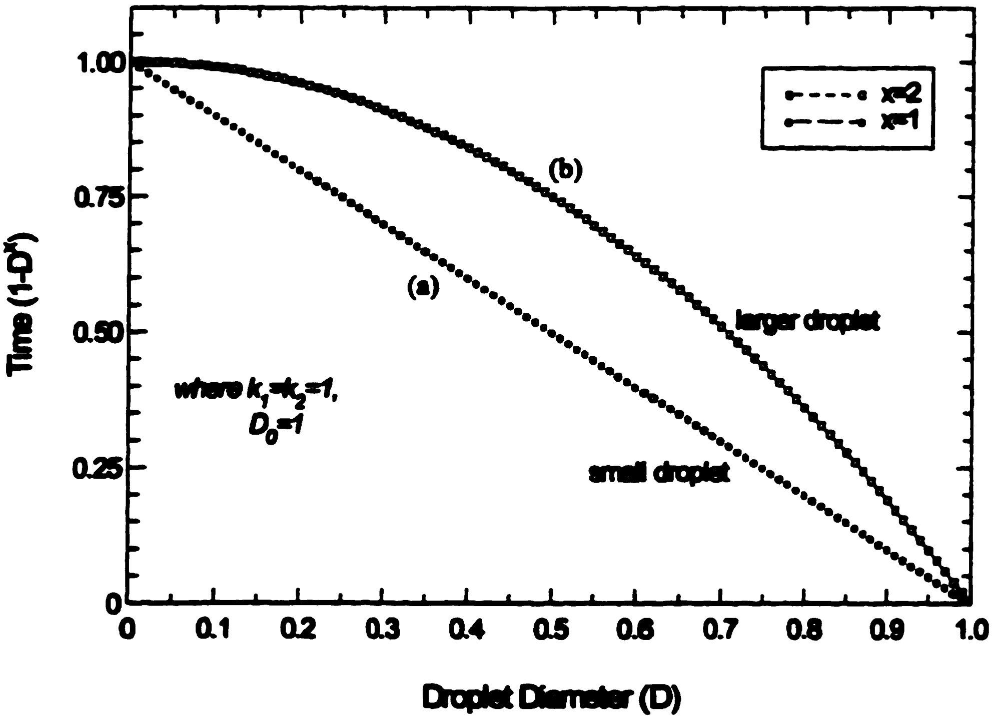

Figure 70. Qualitative size-dependent droplet evaporation; (a): small droplet, (b): large droplet, respectively.

$$1 - (k_1/D_0^2)t = (1 - I/I_{max})^{2/3} \qquad (52)$$

A plot of $[1 - I/I_{max}]^{2/3}$ versus t should, therefore, yield a straight line if normal heat or mass transfer controls vaporization for large droplets. In the case of small droplets, substitution of Eq. (51) into Eq. (27) yields:

$$1 - (k_3/D_0)t = (1 - I/I_{max})^{1/3} \qquad (53)$$

In this situation, a plot of $[1 - I/I_{max}]^{1/3}$ versus t should give a straight line.

In order to investigate the vaporization process qualitatively in the static spray measurement, vapor phase fluorescence intensity was used. Then, the total fluorescence intensity of the vapor phase was calculated from the image in Fig. 65(b) as a function of elapsed time. In order to see whether the change in total vapor phase fluorescence intensity was due to the vaporization of the liquid droplets, $(1 - I/I_{max})^x$ in Eq. (52) or (53) was plotted as a function of time as shown in Fig. 71. The exponent x depends on the size of the droplet : for small droplets (≤ 0.1 μm), x = 1/3, and for large droplets, x = 2/3. The data indicated by (a) and (b) in Fig. 71 represent the analysis for a small droplet and a relatively large droplet, respectively. Two solid lines in the data represent the best fits of these data. As can be seen, the data points (b) were fitted well with an exponential equation, while data points (a) were fitted with a simple linear regression indicating small droplet vaporization: y = a – bx, where y is equal to $(1 - I/I_{max})^{1/3}$, x is the elapsed time (or vaporization time), and a and b are fitting constants indicating the droplet

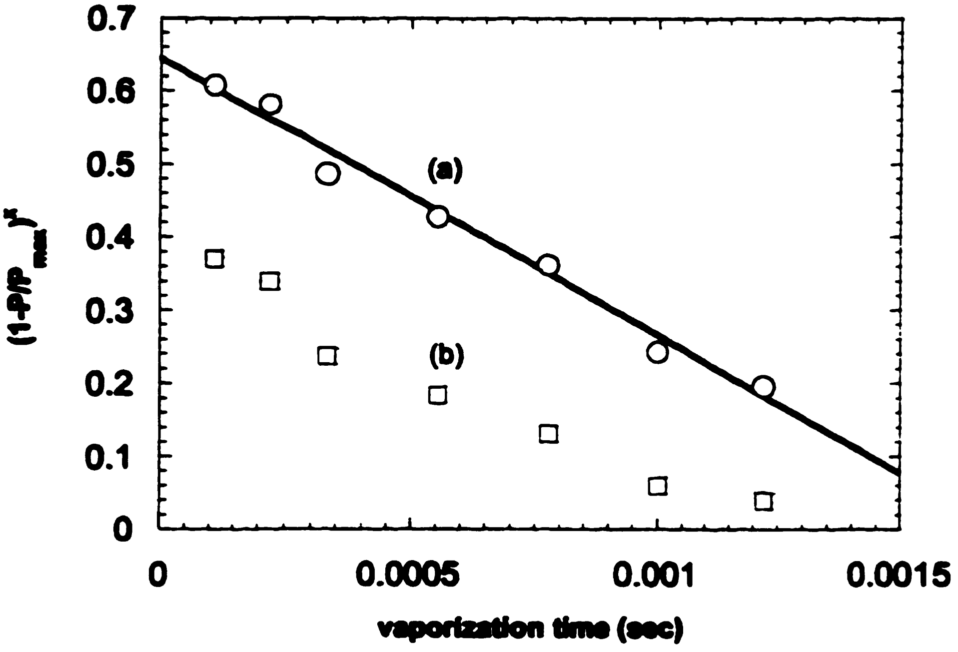

Figure 71. A plot of $(1\text{-}P/P_{max})^x$ as a function of time (vaporization time).(a): x = 1/3, small droplet, (b): x = 2/3, relatively large droplet analysis.

diameter ratio, i.e., (D/D_0) and vaporization rate constant (k_3/D_0), respectively. Although the vapor phase fluorescence intensity is the sum of the contributions from the vaporization of all different size droplets, it may be concluded that, early in the injection process only small droplets whose diameter are smaller than 0.1 μm [95] seem to play an important role in the vaporization process.

5.2. Direct engine applications

While the direct calibration method mentioned in Chapter 4 can be applied to both the liquid and vapor phase fuel spray quantification which is in ambient temperature and pressure, it may not be applicable for direct measurement of the fuel concentration in an internal combustion chamber with a motored engine condition. Since the fluorescence intensity from the phase markers can be affected by the pressure, temperature, and the mixture density which are continuously changing with the moving piston inside the quartz cylinder, some means for the quantitative evaluation of the fuel distribution, especially during the compression process, is necessary in the motored engine condition. In fact, the fluorescence intensity of the DMA vapor phase developed in Chap. 4 depends on the concentration and quantum yield explicitly. The quantum yield of most of the organic molecules, such as DMA, depends on temperature and pressure.[68] Therefore, the fluorescence intensity of DMA in the vapor phase is an implicit function of those parameters in a motored engine condition. On the other hand, the effect of temperature and pressure variation on liquid phase fluorescence intensity is not as severe. During the fuel intake process, the pressure of the inside quartz cylinder is relatively constant (i.e., ambient pressure) as shown in Fig. 72. Most of the liquid phase fuel can survive only a

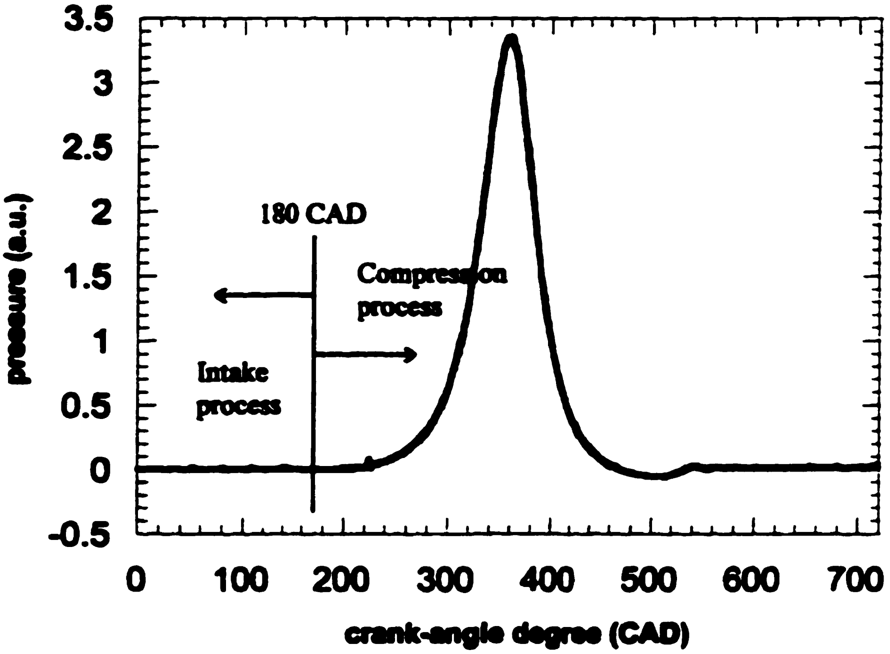

Figure 72. A plot of pressure versus crank-angle degree using a Chrysler 2.4L 16-valve. The engine speed was 600 rpm.

short time after fuel injection because of the fast fuel atomization and vaporization process due to air flow. As a result, during the compression cycle in which temperature and pressure are relatively high, most of the liquid phase fuel will be vaporized; its fraction is much smaller than that of the vapor phase. Therefore, the next section, emphasis is placed on the vapor phase fuel calibration in a motored engine.

5.2.1. In-cylinder fuel vapor calibration

Figure 73 shows the experimental schematic diagram of an in-cylinder fuel vapor calibration. The same experimental setup was used in the actual engine measurements. In the calibration, 5% DMA was used in 95% isooctane fuel. A perfectly premixed, uniform gaseous charge was supplied to the combustion chamber through the engine intake manifold. In the motored engine condition, calibration was made using a equivalence ratio (ϕ) instead of DMA concentration. The equivalence ratio (ϕ) is defined as the fuel to air ratio at stoichiometry. It can be calculated by measuring the rate of mass flow of fuel and air.

The combustion chamber was emulated by an optically accessible quartz cylinder, shown in Fig. 61(b). A schematic diagram of the engine cylinder head configuration is shown in Fig. 59(b). Figure 74 represents a typical fluorescence image as a function of crank-angle degree (CAD) obtained from the premixed DMA vapor phase using a 0.004" orifice size and 80 psi fuel delivery pressure with 600 rpm engine speed. The bright specks in the images, especially at the right hand side, is believed to be due to the reflection between the inner and outer wall of the quartz cylinder.[135] Individual images

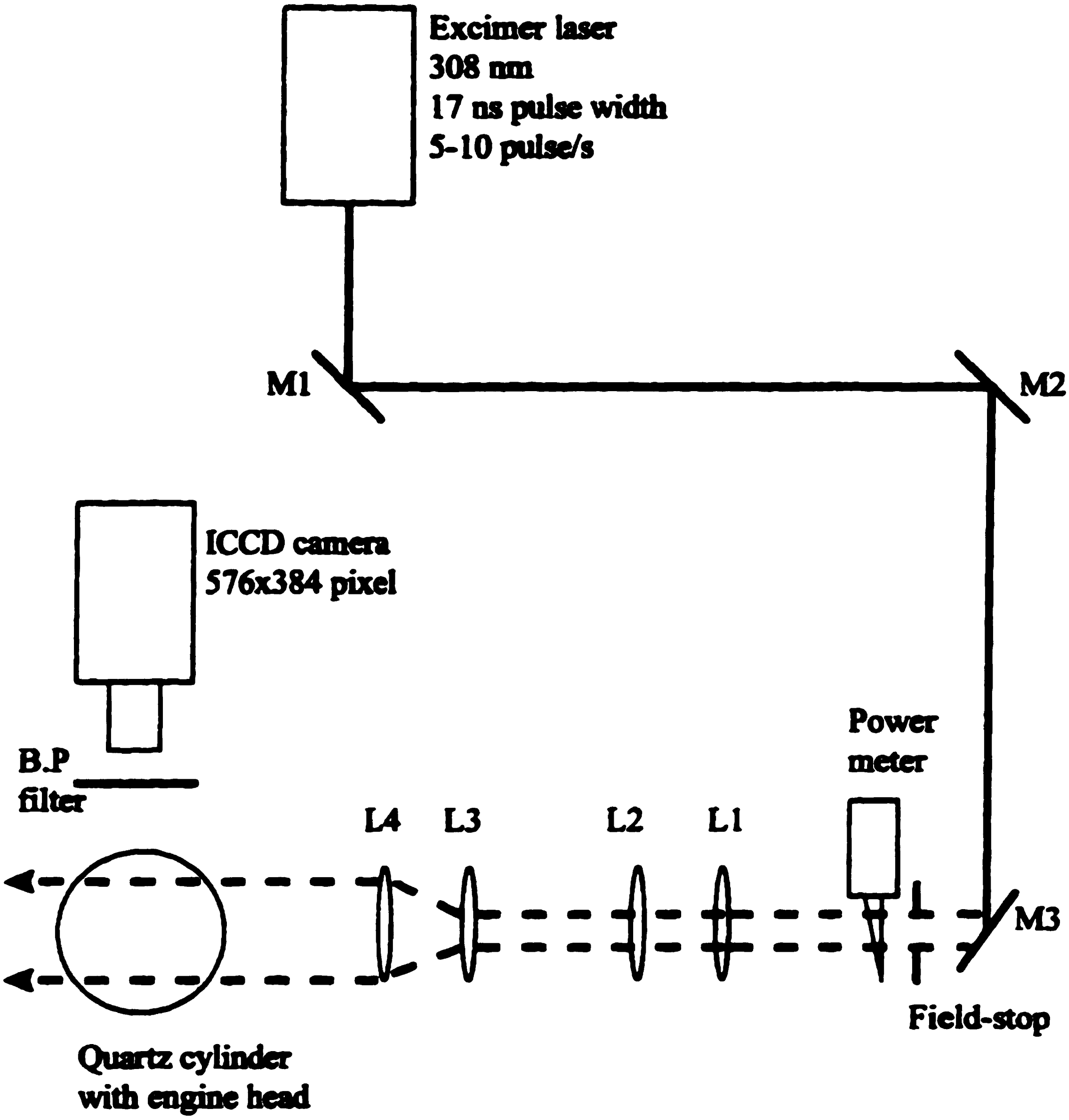

Figure 73. A schematic diagram of an in-cylinder fuel vapor calibration (or actual engine measurements) setup. The final beam steering mirror (M3) moves the laser sheet through the combustion chamber (quartz cylinder). Approximately, 800 μm thick and 50 mm wide horizontal sheet of light was produced using a field-optics consisting cylindrical fused-silica lenses. (*L4 = 145.63 mm, L3 = -37.5 mm, L2 = -37.5 mm, L1 = 300 mm*, respectively).

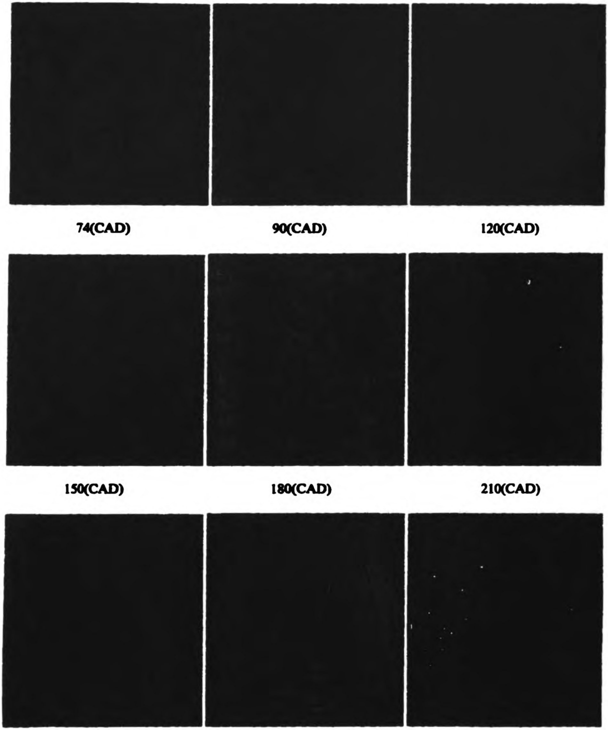

74(CAD) 90(CAD) 120(CAD)

150(CAD) 180(CAD) 210(CAD)

240(CAD) 270(CAD) 300(CAD)

Figure 74. A typical of DMA vapor phase calibration image (5%DMA in isooctane solvent : premixed & preheated) using a 0.004" orifice and 80 psi fuel delivery pressure.(0.004"-80 psi).

were made by averaging over five laser shots. Each image was then used to calculated the equivalence ratio as a function of CAD. As seen in Fig. 74, although the same equivalence ratio was used, the fluorescence intensities of consecutive images slowly increased as the crank-angle advanced. However, each image reveals fluorescence attenuation along the laser beam direction (e.g., the fluorescence intensity at the left-hand side of the image is slightly higher than that of right-hand side). The attenuation effect was enhanced by increasing equivalence ratio and CAD. However, the latter had more effect, especially large CAD.

Using these images, the DMA fluorescence intensity was then calibrated as a function of CAD for all equivalence ratios. The mass flow rate of isooctane was measured as a function of applied pressure and shown in Fig. 75. As was the mass flow rate of fuel, the mass flow rate of air was also measured at 600 rpm, which provides various equivalence ratios. The fluorescence intensity of DMA vapor phase for various crank-angle degrees is shown in Fig. 76. Regardless of their relative equivalence ratios, the general features were quite similar: during the intake process the fluorescence intensity gradually increased, but during the compression process it increased abruptly. Generally, those images that contained high equivalence ratios produced high fluorescence intensity at each CAD. In order to know the relationship between fluorescence intensity and equivalence ratio with respect to various crank-angle degrees, the data in Fig. 76 were rearranged and the fluorescence intensity plotted as a function of equivalence ratio at fixed CAD. Figures 77 and 78 represent the results during the intake and compression process, respectively. The intensity of individual data in Fig. 77 and 78 was normalized by the maximum intensity (e.g., the maximum fluorescence intensity per

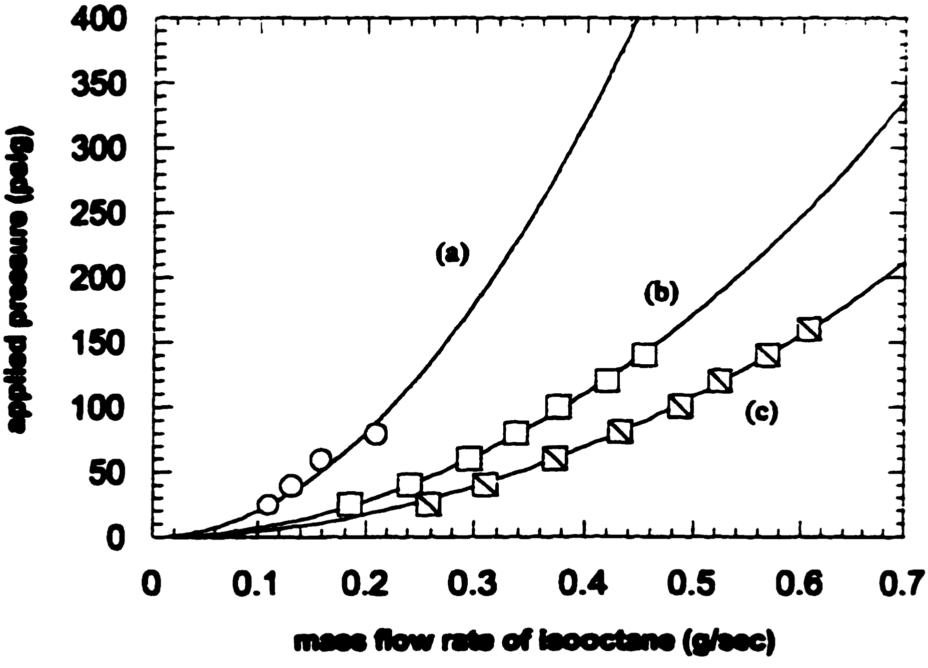

Figure 75. A plot of isooctane mass flow rate as a function of applied pressure; (a): 0.003", (b): 0.004", and (c): 0.005" orifice size, respectively.

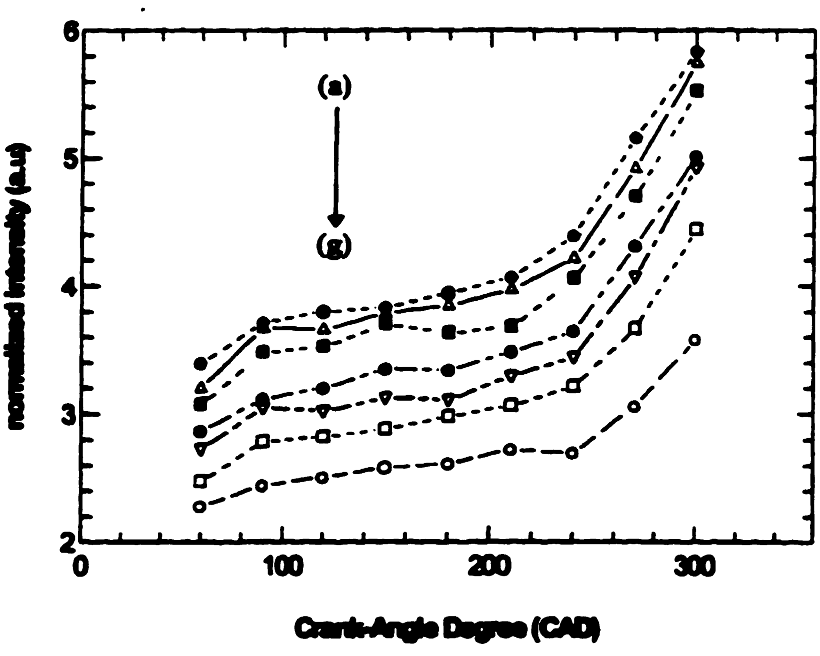

Figure 76. A plot of normalized intensity of DMA vapor phase as a function of crank-angle degree for a various equivalence ratio (ϕ); (a): 1.09, (b): 1.031, (c): 0.954, (d): 0.862, (e): 0.779, (f): 0.682, and (g): 0.563, respectively.

pixel can be found when equivalence ratio (ϕ) is equal to 1.09 at 300 CAD). As shown in Figs. 77 and 78, the fluorescence intensity was increased by increasing the CAD. This may be explained by the growth of dense DMA vapor mixture due to the rising piston. Rising piston reduces the effective volume thereby causes relatively dense mixture. However, as observed in Figs. 77 and 78, the intensity increment does not follow a linear progression as the crank-angle advances. As discussed in Chap. 4, the vapor phase fluorescence intensity is proportional to the quantum yield and fluorescent species concentration in the excited electronic state as shown in Eq. (54)

$$S_f \propto [\phi_f^0][I_0 b^{-1} (1-\exp[-\varepsilon cb])] \qquad (54)$$

In fact, quantum yield is a function of temperature and pressure i.e., at given species concentration, fluorescence intensity is diminished as increasing temperature and pressure probably due to collisional quenching between molecules. In a motored engine condition, especially during the compression process, all thermodynamic parameters (e.g., T, P, and V) are continuously changing with crank-angle degree, therefore, for direct measurement of an equivalence ratio from the fluorescent image, it is necessary to take into account of the variation in pressure, temperature and mixture density inside the cylinder. Moreover, as shown in Fig. 7 in Chapter 3, the DMA absorption and emission profile overlap, therefore, there exists a potential secondary re-absorption of the DMA fluorescence emission by the unexcited DMA vapor within the distance between excitation zone and the top of the piston head. Following Shimizu et al.[68] the measured fluorescence intensity per pixel was represented as a function of the equivalence ratio (ϕ) and crank-angle degree (θ), leading to the following equation to replace Eq. (54)

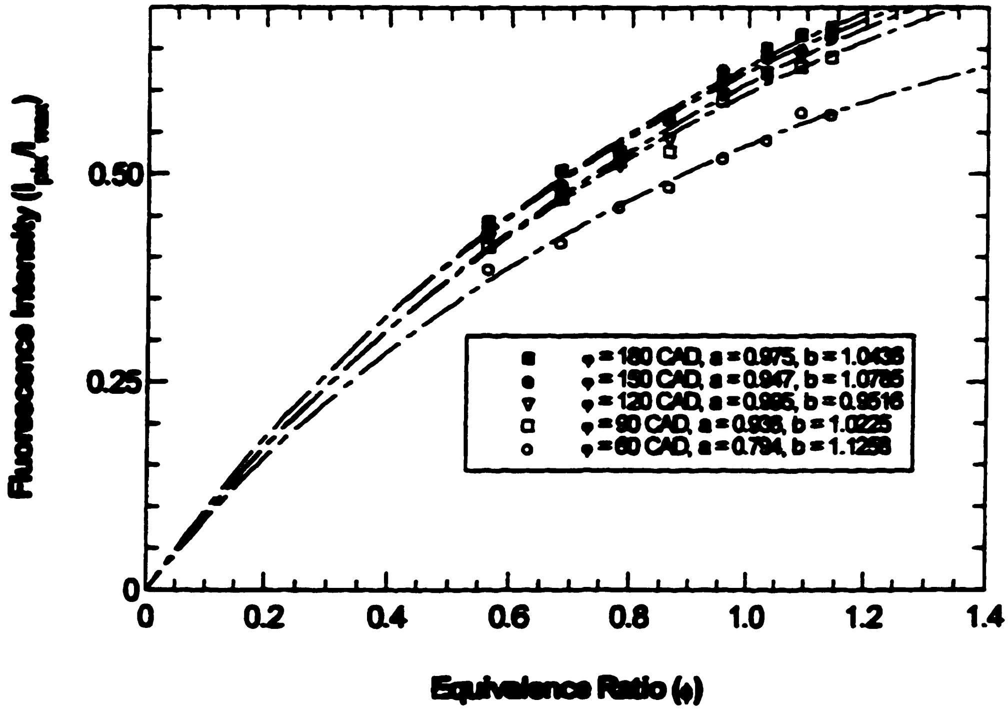

Figure 77. Fluorescence intensity as a function of equivalence ratio (ϕ) for various crank-angle degree (intake process).

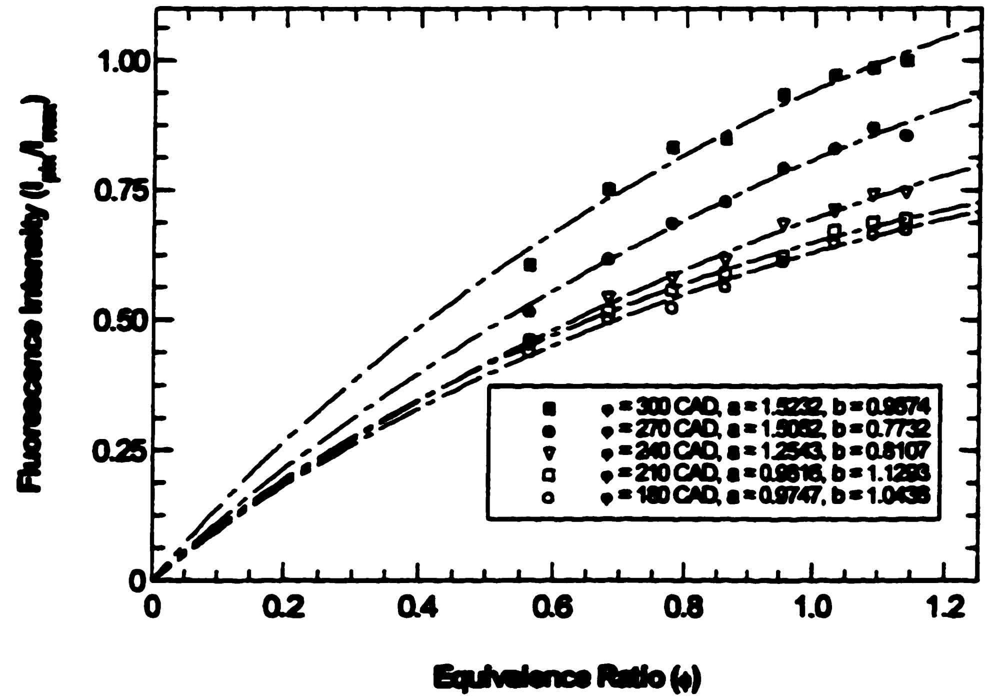

Figure 78. Fluorescence intensity as a function of equivalence ratio (ϕ) for various crank-angle degree (compression stroke).

$$L_{pix} \propto \alpha(\theta)(1-\exp[-\beta(\theta)\phi]) \qquad (55)$$

Here, $\alpha(\theta)$ and $\beta(\theta)$ are explicit functions of the crank-angle degree (θ), and are again implicit functions of transient pressure, temperature, mixture density and the distance between excitation zone and the top of the piston head. The dashed lines in Fig. 77 and 78 are fits of Eq. (55) to the data. On the basis of the measured fluorescence intensity and equivalence ratios, the following parameters, i.e., $\alpha(\theta)$ and $\beta(\theta)$, were obtained for nine representative crank-angle degrees and were tabulated in Table 7. Those values in Table 6 were used as calibration factors in the vapor phase analysis.

Table 7. Transient Temperature, Pressure, Mixture density, and Fluorescence Absorption Effect in the Emission Fluorescence Intensity.

Crank-Angle Degree (θ)	$\alpha(\theta)$	$\beta(\theta)$
60 CAD	0.794	1.126
90 CAD	0.936	1.023
120 CAD	0.995	0.952
150 CAD	0.947	1.079
180 CAD	0.975	1.044
210 CAD	0.962	1.129
240 CAD	1.254	0.811
270 CAD	1.505	0.773
300 CAD	1.523	0.967

5.2.2. Actual engine measurements and interpretation

The bottom views of the 2-D section of liquid phase fuel distribution were obtained at 600 rpm engine speed using a Chrysler 2.4L, 16 valve direct injection spark-ignition engine at wide open throttle (WOT). The isooctane fuel doped with exciplex forming chemicals (e.g., 5%DMA•5%1,4,6-TMN•90% isooctane), was directly injected into the combustion chamber. The injection pressure and duration was set to 700 psi and 1.5 ms, respectively and the fuel injection start was made at 60 CAD after Top Dead Center (TDC). From the preliminary experiment, it was found that the liquid phase fuel could survive until 150 CAD after fuel injection. Therefore, it was necessary to observe the qualitative liquid phase fuel distribution within that time interval. Figures 79(a) and (b) show the liquid phase fuel distributions between 74 and 90 CAD. Those images are average over five laser exposures obtained with the horizontal laser sheet passing through the cross section of the combustion chamber at 2 cm below the top of the quartz cylinder. The two sequential images at fixed crank-angle degree in Figs. 79(a) and (b) represent the cycle-to-cycle variations in the fuel distributions. The first image in Figure 79(a) was taken at 3.89 ms (74 CAD) after injection start, and revealed a relatively highly stratified charge distribution in the central part of the spray. As time proceeded the stratified charge dispersed widely and dissipated. This was anticipated due to the fast atomization and vaporization process in the accompanying air flow field. During this time, the high intensity part of the fuel (e.g., red color) in the central part of the spray fluctuated along the horizontal line of the combustion chamber.

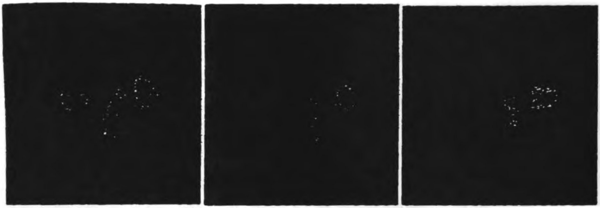

74(CAD) 76(CAD) 78(CAD)

80(CAD) 82(CAD) 84(CAD)

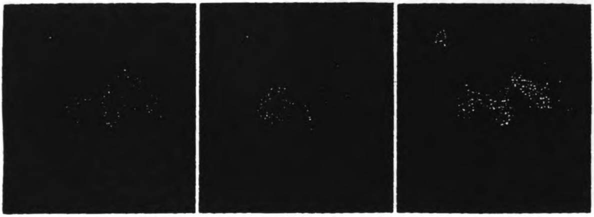

86(CAD) 88(CAD) 90(CAD)

Figure 79(a). In-cylinder liquid phase fuel distributions using a 5%DMA•5%1,4,6-TMN•90%isooctane exciplex system *(fuel injection start : 60 ATDC and fuel injection duration : 1.5 ms).*

74(CAD) 76(CAD) 78(CAD)

80(CAD) 82(CAD) 84(CAD)

86(CAD) 88(CAD) 90(CAD)

Figure 79(b). An example of cyclic variations in Fig.79(a).

A. Liquid phase fuel distributions

Liquid phase fuel image was obtained by one laser pulse excitation i.e., no averaging was required. In order to observe the instantaneous cyclic variations, two consecutive images were acquired at a fixed crank-angle degree, from 74 to 300 CAD. Figures 80(a) and (b) show two consecutive liquid phase fuel distribution images as a function of CAD. At 3.89 ms after fuel injection start (74 CAD), highly localized fuel was observed inside the fuel spray, particularly in the left and right corners. This is a direct indication that an intense jet of liquid emerges from the left and right sides of the fuel injector tip. The consecutive image at this crank-angle shown in Fig. 80(b) represents quite different features, namely, the existence of significant cyclic variations. Approximately 8.3 ms (90 CAD) later, the liquid phase was distributed across most of the cylinder cross-section, and around 16.6 ms (120 CAD), the area inside the cylinder was almost uniformly occupied. In the early intake process after the start of injection, it seemed that, although the liquid phase initially penetrated toward the axial line of the spray injection, it quickly broke up into small droplets with the accompanying air flow and rapidly vaporized. In the time between 25 ms (150 CAD) and 41.7 ms (210 CAD) after the start of injection, both atomization and vaporization processes were active such that a very small amount of liquid remained. Some scattered groups of droplets were found near the walls of the combustion chamber, and on the left wall of the cylinder a thin layer of the liquid film developed. This is believed to be due to the impingement of liquid onto the wall of the combustion chamber. At 50 ms (240 CAD) after the start of injection, however, the liquid fuel was enhanced, especially in the central part of the combustion chamber. In Fig. 80(b), the same feature was found at 58.3 ms (270 CAD)).

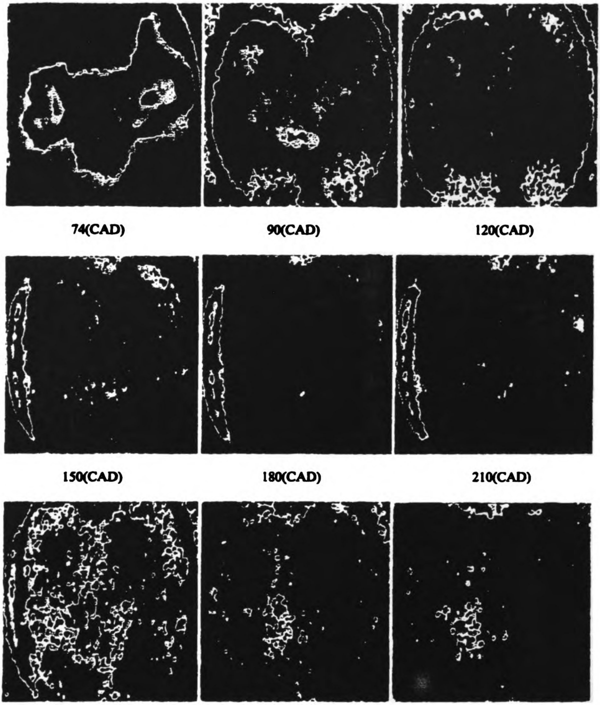

74(CAD) 90(CAD) 120(CAD)

150(CAD) 180(CAD) 210(CAD)

240(CAD) 270(CAD) 300(CAD)

Figure 80(a). In-cylinder liquid phase fuel distributions using a 5%DMA•5%1,4,6-TMN•90%isooctane exciplex system *(fuel injection start : 60 ATDC and fuel injection duration : 1.5 ms).*

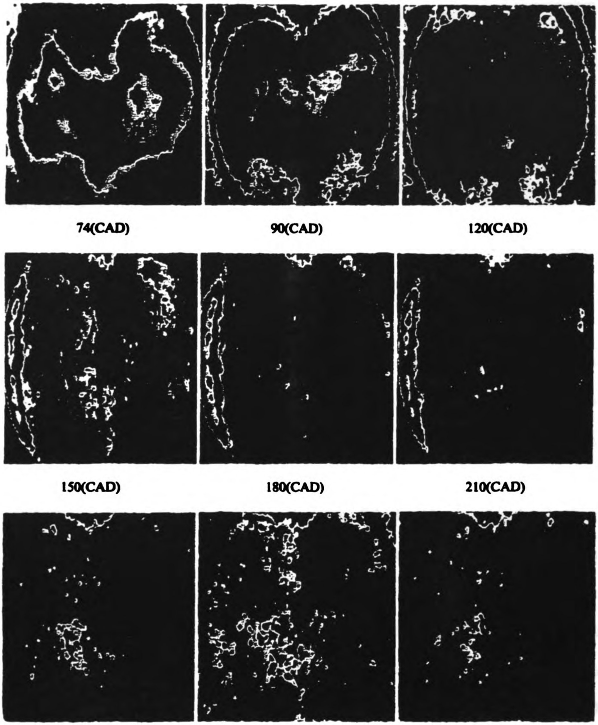

74(CAD) 90(CAD) 120(CAD)

150(CAD) 180(CAD) 210(CAD)

240(CAD) 270(CAD) 300(CAD)

Figure 80(b). An example of cyclic variation of liquid phase fuel distribution in Fig. 80(a).

As time evolved further, the liquid fuel disintegrated into small droplets but still remained in the central part of the combustion chamber at 300 CAD. The enhancement of the liquid phase at 240 CAD (or 270 CAD in Fig. 80(b)) is not understood well but believed to be due to air flow motion inside combustion chamber. Another possible reason for the fluorescence enhancement is liquefaction of vaporized fuel at this specific value of CAD.

In order to make a quantitative representation of the liquid phase fuel distribution, Fig. 80(a) was converted to a iso-intensity contour map, and the results of intensity-concentration (or mass) relation of the liquid phase calibration in Chap. 4 were employed. Figure 81 shows the mass distribution of the liquid phase fuel inside the combustion chamber. The number indicates the amount of mass present in unit of nanograms (10^{-9}g). As shown in the image taken at 74 CAD, the fuel distribution is highly asymmetric. Relatively dense fuel was localized in the left and right corner of the combustion chamber. As time proceeded, the mass of the liquid was reduced and spread out. Eventually, a very small portion of liquid fuel remained at Bottom Dead Center (BTC) ($\theta = 180°$ CAD) except for a thin layer of liquid film on the left side of the combustion chamber. At a later time after the start of injection ($\theta = 240°$ CAD), a small amount of liquid suddenly appeared in most parts of the combustion chamber. Although much liquid evaporated as Top Dead Center approached, a small mass of the droplets still remained in the central part of the combustion chamber at 300 CAD.

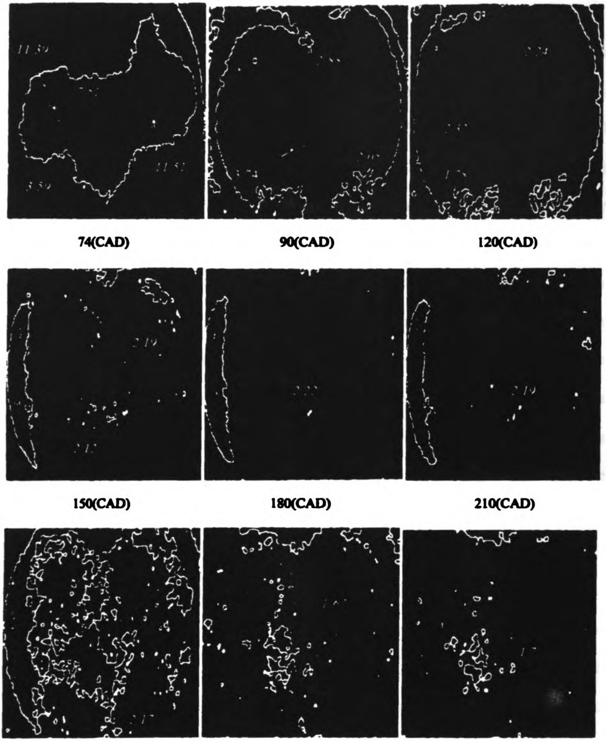

74(CAD) 90(CAD) 120(CAD)

150(CAD) 180(CAD) 210(CAD)

240(CAD) 270(CAD) 300(CAD)

Figure 81. In-cylinder liquid phase fuel distributions (contour-map) using a 5%DMA•5%1,4,6-TMN•90%isooctane exciplex system (number indicates 10^{-9} g / pixel) *(fuel injection start : 60 ATDC and fuel injection duration : 1.5 ms).*

B. Vapor phase fuel distribution

As in liquid phase imaging, two consecutive images of the vapor phase distribution were obtained at the same CAD. Except for the earliest time after injection (e.g., 74 CAD), the vapor phase distribution was quite different from that of the liquid phase. The two consecutive images obtained at the same CAD in Figs. 82(a) and (b) represent the cycle-to-cycle variation in the vapor distribution. Initially, a dense vapor phase appeared and then quickly diffused throughout the combustion chamber. As the crank-angle advanced, i.e., from 90 to 210 CAD, the diffusion process was depleted the central part of the chamber. On the contrary, during the compression process, vapor phase fuel was enhanced greatly and formed stratified charge around the fuel injector. In order to make a quantitative representation, the vapor phase distribution in Fig. 82(a) was converted to an iso-intensity contour map and the results of intensity-equivalence ratios of the vapor phase calibration in Chap. 5 was employed. Since, at given CAD(θ), the fluorescence intensity is known from the measurement and two unknown parameters, such as $\alpha(\theta)$ and $\beta(\theta)$ can be obtained from Table 6, the corresponding equivalence ratio (ϕ) can be calculated from the equation, $I_{pix} = \alpha(\theta)(1-\exp[-\beta(\theta)\phi])$. Figure 83 represents the vapor phase fuel distribution in the combustion chamber as a function of CAD. The individual numbers noted on the contour map are equivalence ratios. As can be seen here, during the intake process it seemed more likely that the amount of vapor, as well as its equivalence ratio diminished, probably due to the diffusion of vapor during the intake process. Conversely, during the compression process, more intense vapor phase formed as the crank-angle advanced, and highly stratified vapor charge mixture was developed near the fuel injector at 300 CAD.

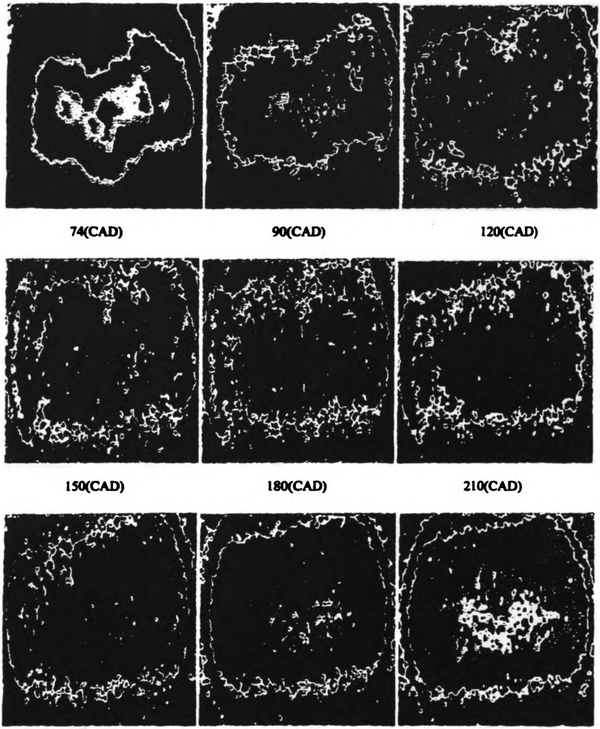

Figure 82(a). In-cylinder vapor phase fuel distributions using a 5%DMA•5%1,4,6-TMN•90%isooctane exciplex system *(fuel injection start : 60 ATDC and fuel injection duration : 1.5 ms)*.

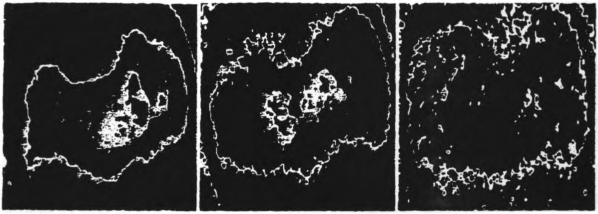

74(CAD) 90(CAD) 120(CAD)

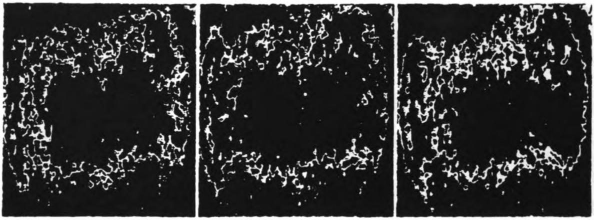

150(CAD) 180(CAD) 210(CAD)

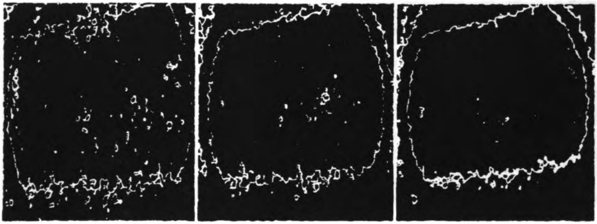

240(CAD) 270(CAD) 300(CAD)

Figure 82(b). An example of cyclic variation of vapor phase fuel distribution in Fig. 82(a).

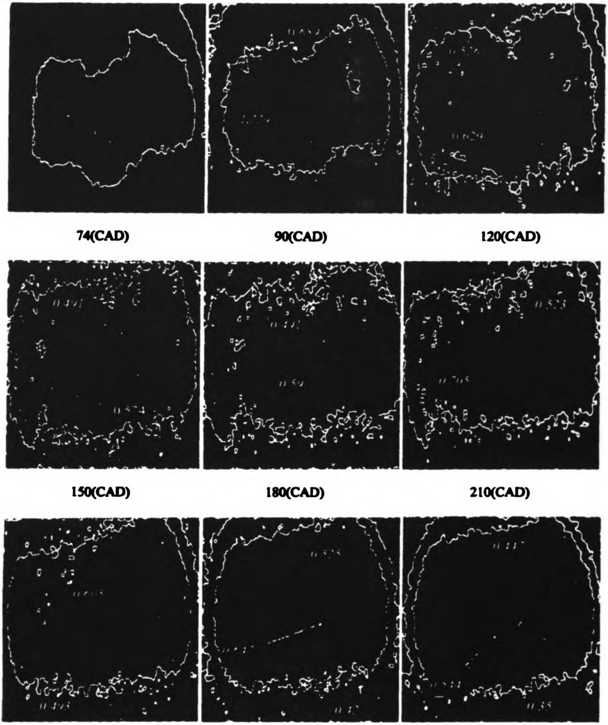

74(CAD) 90(CAD) 120(CAD)

150(CAD) 180(CAD) 210(CAD)

240(CAD) 270(CAD) 300(CAD)

Figure 83. In-cylinder vapor phase fuel distributions (contour-map) using a 5%DMA•5%1,4,6-TMN•90%isooctane exciplex system (number is the equivalence ratio (ϕ)) ***(fuel injection start : 60 ATDC and fuel injection duration : 1.5 ms).***

Although the stratification of vapor phase fuel as the piston approaches Top Dead Center (TDC) is not well understood, this may bring benefits in the fuel combustion process because stratified charge mixture around the spark plug can prevent the misfire which obviously causes fuel waste. Recently, many studies of the direct injection stratified charge (DISC) engine have appeared.[134,136,137] With a lean mixture, the stratification of charge around the spark plug is the most important factor in the direct injection engine in improving fuel efficiency [138] and reducing raw NO_x emissions.

Chapter VI. Conclusions and Further Recommendations

6.1. Summary and conclusions

In this study, visualization of a two-phase spray was performed with laser sheet illumination in an optically accessible quartz cylinder using a laser induced exciplex fluorescence technique. Two-dimensional fluorescence image sections from the liquid and vapor phases were obtained. The exciplex fluorescence provided two color emission from the monomer and exciplex which tagged, respectively the vapor and liquid components of the spray. The work evolved in four stages: (1) development of the exciplex system using N,N-dimethylaniline (DMA) and trimethylnaphthalene (TMN) - isomers in a 2,2,4-trimethylpentane (isooctane) solvent; (2) calibration of the exciplex fluorescence for quantitative interpretation of liquid and vapor phase fuel concentrations; (3) exciplex visualization of a hollow cone spray in a static test cylinder; and (4) exciplex visualization of the fuel distribution in an internal combustion chamber under motored engine conditions. Observations and conclusions from the four sections are represented in the following.

6.1.1. Development of new exciplex system

New exciplex systems formed between dimethyl- or diethyl- substituted aniline and trimethyl substitute naphthalene in isooctane fuel were developed. The 5%DMA•5%1,4,6-TMN in 90% isooctane exciplex system had the best quantum yield and largest spectral separation between the monomer and exciplex emission. A fluorescence experiment, conducted at temperatures around 200° C, revealed that this system was sufficiently stable to permit useful applications in this regime.

6.1.2. Calibration of exciplex fluorescence

A. Ambient condition

Using the optimized exciplex, fluorescence intensity vs. concentration calibration experiments were performed. The results showed, that at small concentrations, both the liquid and vapor phase fluorescence intensity were linear with the concentration (or mass) of the fluorescing molecules. Although the molar absorption coefficient (ε) of the liquid droplet employed in the liquid phase calibration was optically thick ($\varepsilon \geq 3.0$), the measured fluorescence intensity versus droplet mass showed a linear relationship. This can be explained by the saturation effect of the fluorescence intensity coupled with a very high excitation from the intense excimer laser pulse. Under these conditions the fluorescence signal is independent of the source irradiance, fluorescence quantum efficiency, and the molar absorption coefficient $\varepsilon(\lambda)$, because the rates of stimulated absorption and emission are balanced. Thereby, the fluorescence intensity only depends on the concentration of solute. In the vapor phase calibration, two different approaches, direct pressure measurement and absorption measurement, were performed to calculate the molar concentration of the DMA. Based on the Clausius-Clapeyron equation, the direct pressure measurement was more accurate. The pressure measurements from the direct method gave much higher vapor pressures (about five times) than those of absorption measurements. It appeared that the most likely cause of the discrepancy was an incorrect value of the molar absorption coefficient of DMA, perhaps due to the fact that the value used was for DMA in a solution, whereas the direct pressure measurement was in the vapor phase. Moreover, since the molar absorption coefficient (ε) is a characteristic of the solute and depends on the wavelength of the excitation light, solvent, and temperature, the absorption method is more sensitive to error for vapor-phase concentrations which are dependent on temperature.

B. Motored engine condition

In a motored engine condition, liquid phase fluorescence intensity-concentration (or mass) calibration results were directly used by assuming that the effects of temperature and pressure on the fluorescence intensity were weak. In the vapor phase, a pre-mixed DMA vapor charge was supplied and uniformity was provided in the combustion chamber. A measurement of the fluorescence intensity versus equivalence ratio (ϕ) was performed. The calibration results showed that the fluorescence intensity increased with respect to equivalence ratio as the crank angle increased. Moreover, at fixed equivalence ratio, fluorescence intensity increased nonlinearly as a function of crank angle. This can be explained mainly by the fact that the compression increases the density of the DMA molecules. However, negative contribution could be expected from increased collisional fluorescence quenching, re-absorption, and additional attenuation.

6.1.3. Results of the fuel spray in a static quartz cylinder

Results of the fuel spray obtained by laser illumination showed that it had a hollow cone shape. The highest concentrations of the vapor were associated with the highest concentrations of the liquid phase implying that the vapor fuel was evaporating from individual liquid droplets. The spray generally showed symmetry about the spray axis but at high concentration an asymmetry was observed. The liquid phase fluorescence was typically 70-80 times larger than that of the vapor phase in most parts of the spray area. To better understand the droplet vaporization process in the spray, a simple droplet model was employed. Results showed that, during the injection process, very small droplets (dia. $\leq 0.1\ \mu m$) play an important role in the vaporization process and the mass diffusion-controlled vaporization (rather than heat diffusion-controlled) is the dominant effect.

6.1.4. Results in a motored engine

Two-dimensional image sections were obtained from an optically accessible combustion chamber equipped with a 2.4L, 16-valves Direct Injection Spark-Ignition (DISI) engine as a function of the crank angle degree. The in-cylinder measurements revealed that both the liquid and vapor phases showed cycle-to-cycle variations. However, the liquid phase showed much more cyclic variation. The life span of most of the liquid phase was relatively short, i.e., during the intake process most of the liquid was vaporized. This is believed to be due to fast atomization and evaporation resulting from the turbulent air flow. In the early stage of the compression, the liquid phase was enhanced abruptly. Near the end of a cycle, most of the liquid phase fuel was disappeared, and a very small mass of liquid still remained in the central part of the combustion chamber. This is probably due to in-cylinder air flow. The fuel distribution of the vapor phase differed from the liquid phase. As time proceeded, more vapor phase developed in the central part of the cylinder and eventually a very intense stratified charge developed near the injector. The reason why stratification of the vapor phase occurs as the piston approaches its TDC is not well understood. However, it may bring benefits to the fuel combustion process since a stratified charge around the spark plug can prevent misfires which wastes fuel.

6.2. Further recommendations

Although the application of the DMA•1,4,6-TMN exciplex system in a direct injection spark ignition (DISI) engine to actually "see" the temporal and spatial behavior of the injected fuel spray has proven fruitful, it requires more study for better understanding. Firstly, the exciplex fluorescence performance deteriorates at high temperatures. As temperature increases, fluorescence intensity decreases and its peak emission intensity wavelength is blue-shifted. Therefore, the cross-talk between the monomer and exciplex emission increases, and the monomer fluorescence emission contains unavoidable contributions from the liquid phase fluorescence, and vice versa. More importantly, fluorescence emission from most organic molecules, such as DMA, are quenched by oxygen; therefore, a nitrogen environment was necessary in most of our engine experiments. This means that it was not possible to see the vapor and liquid characteristics of fuel in a real combustion environment that requires oxygen. In the DMA•1,4,6-TMN exciplex systems, the normal boiling point of the fuel solvent, isooctane, is 100° C and the vapor phase marker, DMA, is 194° C. The different volatilities cause different evaporation rates, so that early in the engine cycle, the use of DMA may cause an underestimate of fuel vapor concentration. Also, any fuel distribution studies should be accompanied by an in-cylinder air flow study, using e.g., MTV, PIV or LDV, for better understanding of fuel-air mixing processes: droplet atomization, vaporization, and diffusion of the vapor phase. Some means to address these problems are required for the better understanding of the air fuel mixing process, its distribution, and eventually real combustion behavior in an engine.

APPENDIX

The appendix contains two major parts. One is the technical information (A.1 & A.2) to assist the user in the operation of the equipment in this setup and is meant as a supplement to the equipment manuals. The other is the detailed information about how quantitative images were calculated in a motored engine condition (A.3).

A.1 Equipment Connection for Laser Induced Fluorescence Imaging

The connections for the ICCD detector system and excimer laser for the laser induced fluorescence portion of the experiment are shown in Fig. 84. The Connections shown in Fig. 84 are a combination of Case 1 and Case 2 in section 6.3.1, ICCD Gating Experiments Examples, of the Princeton Instruments manuals.[127] The timing diagram for this configuration is shown in Fig. 85. The excimer laser triggers the pulse generator which sends a high voltage gate pulse to the intensifier in the ICCD detector. The delay between the laser trigger and gate pulse is adjustable so that the detector can be gated after the laser emission occurs. The 'enable in' to 'not scan' connection prevents the array from being exposed during readout by blocking the gate pulses. The 'trigger out' to 'ext. sync.' connection initiates readout when the system is being externally triggered and the controller is being operated in the external synchronization mode. The time during which data is acquired is determined by the 'exposure time' set in the software. The number of exposures accumulated by the detector array per readout is determined by the exposure time and the laser repetition rate. For one exposure per readout, the exposure time can be set to zero or the laser repetition rate can be adjusted accordingly.

A.2 Operational Information for the Laser Induced Fluorescence Imaging System

The gain of the ICCD detector and the pulse width of the gate pulse generator are controlled by ten-turn potentiometers, but are not linear with the potentiometer setting. Experiments were done to determine the gain and pulse width versus potentiometer setting. The ICCD detector gain is variable from 1 to 100 times. Table 8 summarizes the average intensity gain versus potentiometer setting for the detector. Potentiometer settings are read from 0 to 1000. The gain versus potentiometer setting for the ICCD detector is shown in Fig. 86.

The pulse width of the FG-100 pulse generator is variable from 18 to 650 ns in range 1 of the variable width mode. A Tektronix 11302 oscilloscope was used to measure the pulse width. Table 9 summarizes the pulse width versus potentiometer setting. The potentiometer collar with the setting indicator mark on it must be turned clockwise when setting the position. There is a small amount of play in the collar which will affect the pulse width by as much as 50 ns. If the potentiometer is turned gently to 1,000, the pulse width will be 600 ns. If light torque is applied to the knob, the pulse width will increase to 650 ns. All other positions were repeatable. The pulse width versus potentiometer setting for the FG-100 pulse generator is shown in Fig. 87.

Another experiment was conducted to determine the gate pulse delay setting required to initiate detector gating immediately after the laser laser emission pulse, yet avoid gating before laser emission had decayed. This was necessary to ensure that the image intensities in the calibration were due only to fluorescence emission and not direct laser emission. It was carried out by focusing the detector on a piece of aluminum which scattered the laser pulse while emitting negligible fluorescence that would obscure the decay of the laser emission pulse. The laser pulse width is approximately 18 ns. The shortest detector gate pulse width, also of approximately 18 ns, was used. The maximum intensity of the images was then monitored while varying the delay setting. The peak image intensities occurred at a delay potentiometer setting of 624. Increasing or decreasing the delay from 624 resulted in a decrease in the intensities. Therefore, the laser emission pulse and the detector gate pulse were completely overlapped at 624.

The absolute delay time could not be measured. However, the change in delay time for a given change in potentiometer setting could be measured with the oscilloscope. From this it was determined that the delay time increases 1.6 ns per unit change of the potentiometer setting. Delaying the gate pulse an additional 20 ns should place the leading edge of the gate pulse 2 ns after the trailing edge of the laser emission pulse. This translated into a delay setting of 637. At this setting, the image intensities indicated that the trailing edge of some of the laser pulses was being caught by the gate pulse. This was probably due to trigger jitter in the excimer laser. A delay setting of 640 cleared this up and was used for the calibration. Changing the gate pulse width does not affect the delay setting required. The trailing edge of the gate pulse moves when the pulse width is changed. The leading edge remains fixed relative to the trigger. Table 10 summarizes the gate pulse delay time versus potentiometer setting and the Figure 88 shows their relationship.

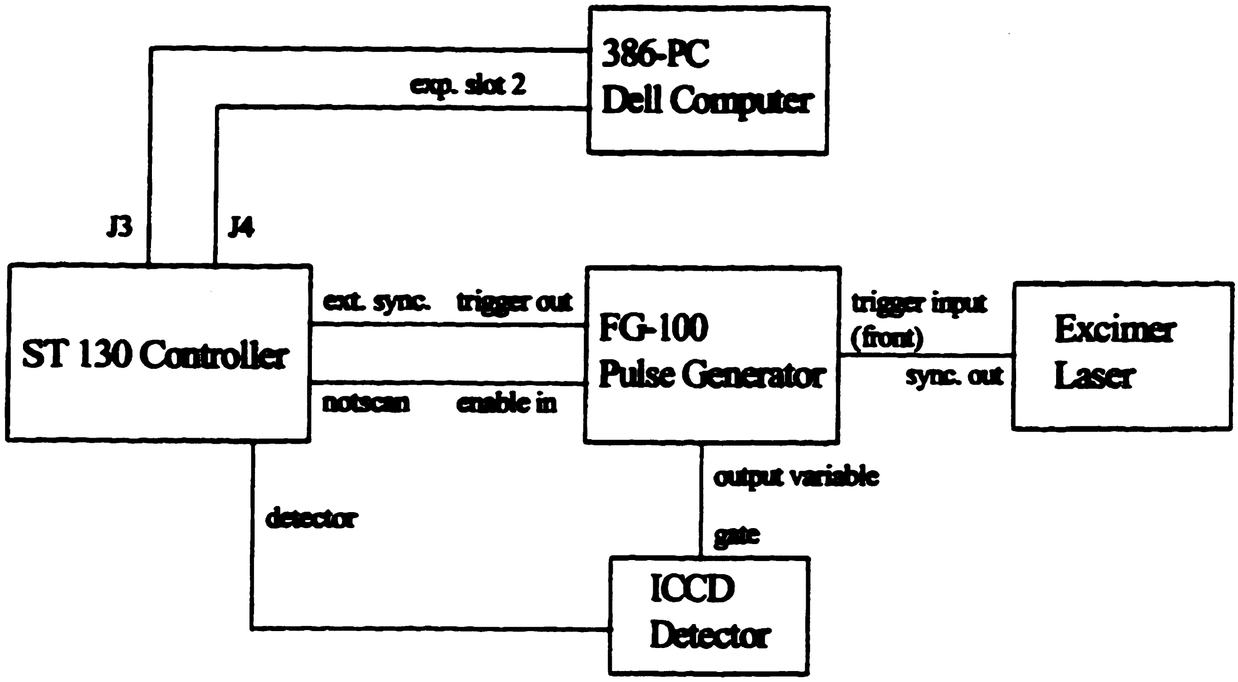

Figure 84. Connections for laser induced exciplex fluorescence experiment.[127]

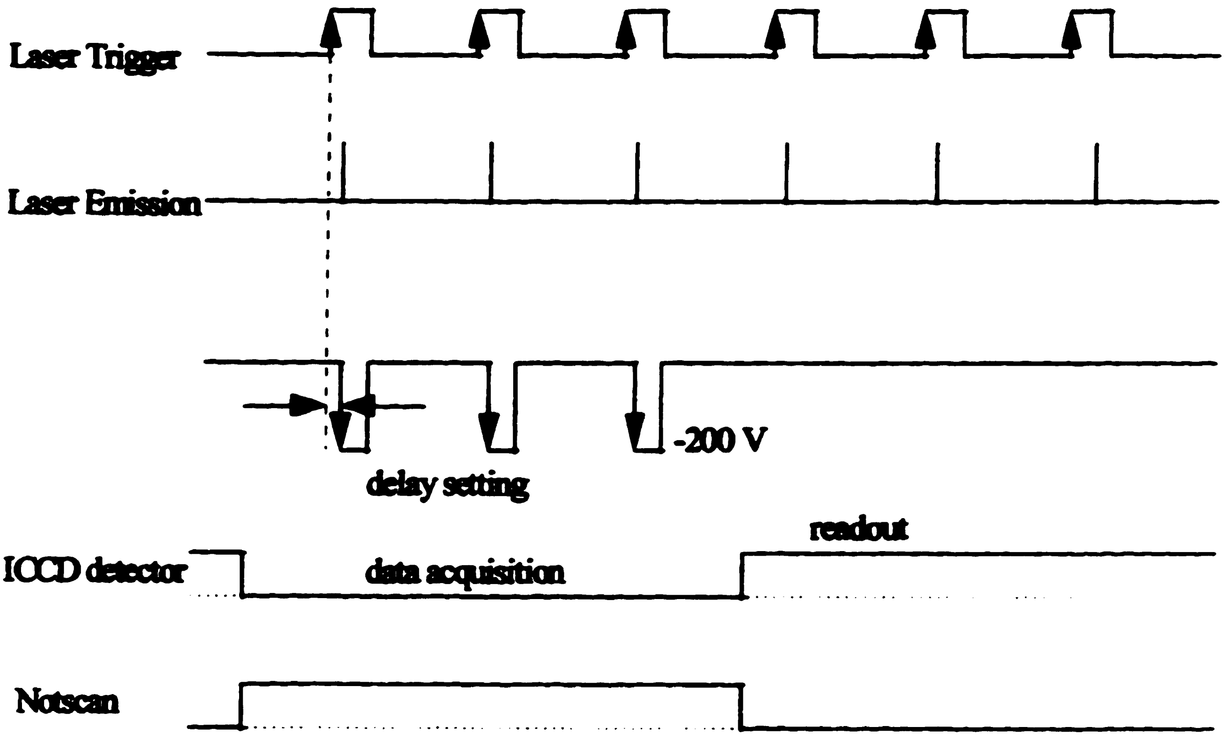

Figure 85. Timing diagram for ICCD detector system configuration.[127]

TABLE 8: Average Intensity Gain versus Potentiometer Setting

Potentiometer Setting	Intensity Gain
1000	100.0
990	86.86
980	76.35
970	66.84
960	55.91
950	47.22
940	40.82
930	34.83
920	29.61
910	25.47
900	20.97
850	8.864
800	3.577
750	1.683
700	1.039
650	0.860
600	0.816
550	0.810

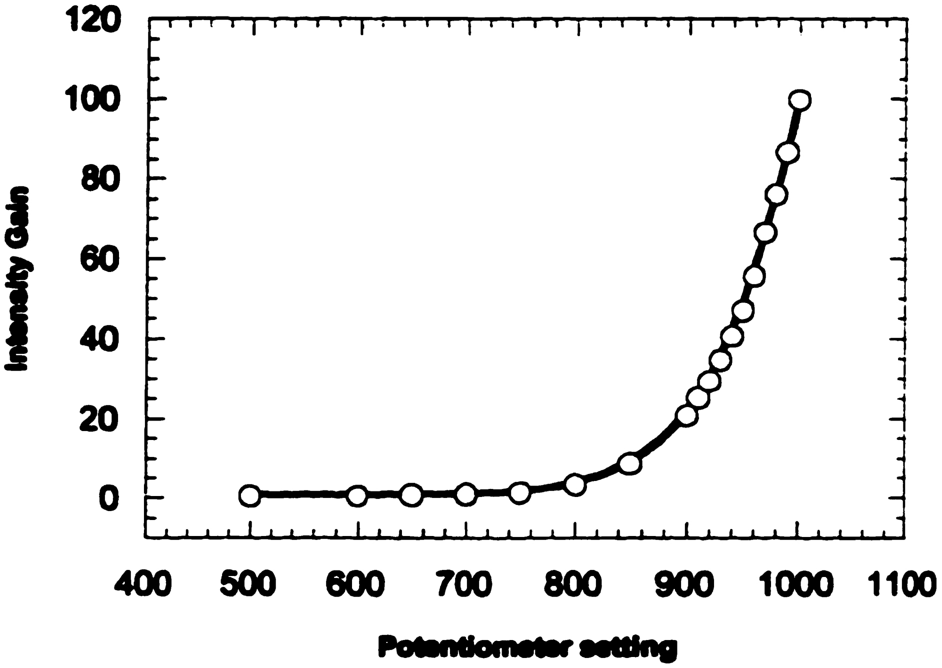

Figure 86. A plot of gain versus potentiometer setting for the ICCD detector.

TABLE 9: Gate Pulse width versus Potentiometer Setting

Potentiometer Setting	Pulse width (ns)
1000	600-660
998	522
997	450
996	421
995	392
993	355
990	305
986	254
980	203
970	149
945	92
900	61.3
0	18.7

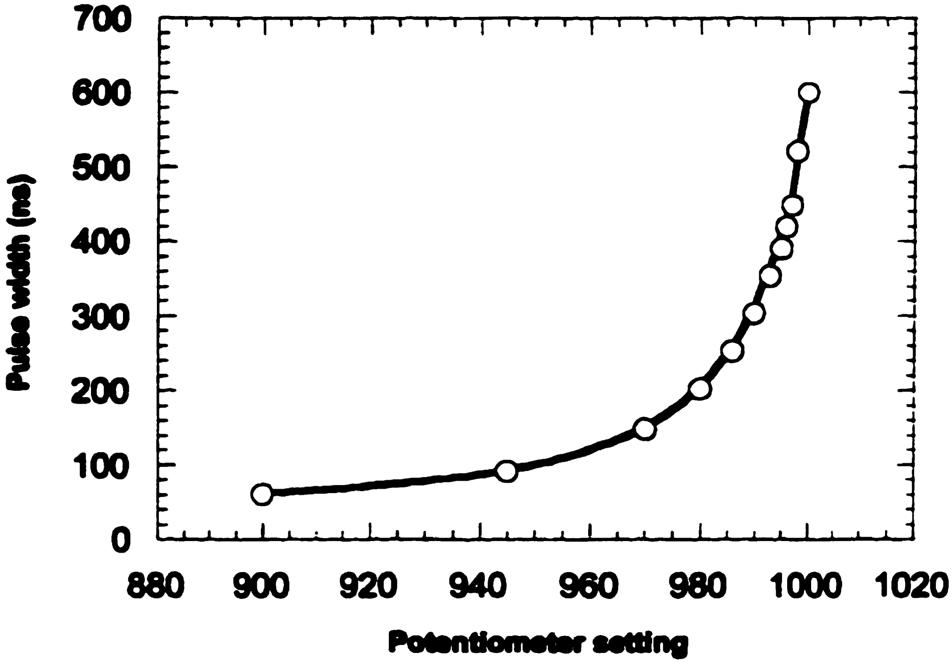

Figure 87. A plot of pulse width versus potentiometer setting for the FG-100 pulse generator.

TABLE 10: Delay Time Versus Potentiometer Setting

Potentiometer Setting	Delay Time (ns)
0	76.1
50	164
100	237
150	329
200	402
250	493
300	566
350	657
400	730
450	821
500	894
550	986
600	1059
650	1150
700	1223
750	1314
800	1387

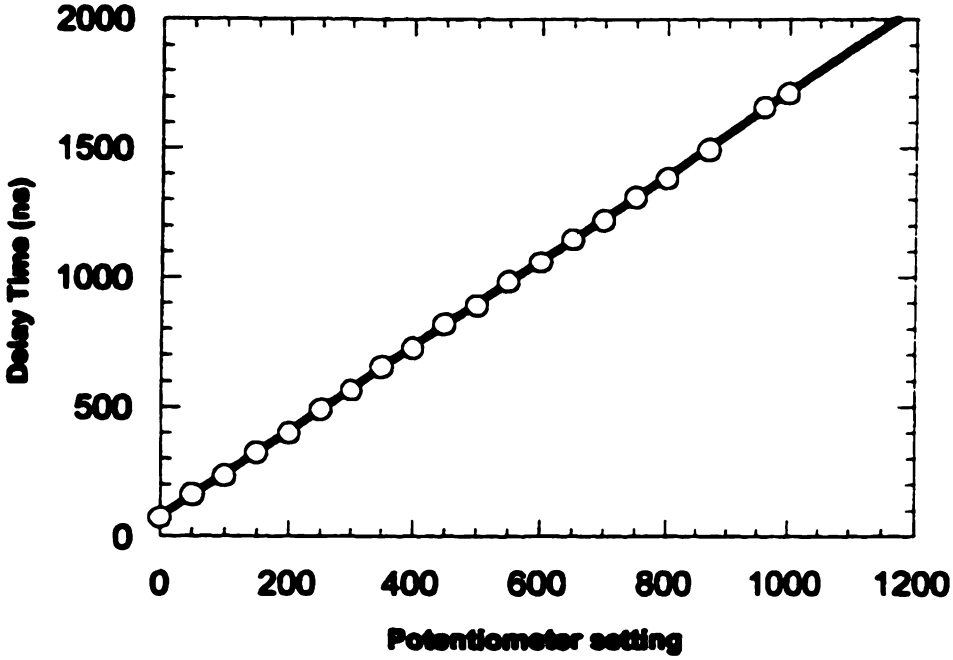

Figure 88. A plot of gate pulse delay time versus potentiometer setting.

A.3. Calibration Procedures in In-Cylinder Measurements

This appendix describes the detailed information about how quantitative images were calculated, i.e., equivalence ratio vs. fluorescence intensity for the vapor phase and mass of the liquid droplet vs. fluorescence intensity for the liquid phase in a motored engine condition.

(A) Liquid Phase Fuel Distributions

Assumptions used in the liquid phase quantification in a motored engine

(1) Identical geometry is assumed between the droplet calibration experiment and the in-cylinder fuel spray measurements, and neglected the presence of the quartz cylinder.

(2) Fluorescing volume is given by the thickness of the laser beam (800 μm) multiplied by the intersected area of the inside cylinder.

(3) The fluorescence area is assumed to be the sum of the individual horizontal line that is assumed to have the same efficiency.

(4) Droplet size is different and independent.

(5) The number density of the fluorescing molecules in the liquid droplet is assumed to be small within the intersected area with the laser beam.

Then the in-cylinder liquid phase fuel distribution as a function of crank-angle degree (CAD) was quantified using the droplet mass (M) vs. fluorescence intensity (I) relation obtained in Chap. 4 as shown below.

$$\text{I (counts)} = 656\ \text{(counts/}\mu\text{g)} \times \text{M } (\mu\text{g}) \qquad (56)$$

Where I (counts) is the liquid droplet fluorescence intensity and M (μg) is the droplet mass used in the calibration.

The quantification procedures as follow:

(a) In-cylinder liquid phase fuel distribution as a function of crank-angle degree (CAD) was obtained in Fig. 80(a).

(b) Figure 80(a) was converted to an iso-intensity contour map.

(c) The iso-intensity contour map was then converted to a mass contour map using Eq. 56 and the result was shown in Fig. 81 as a function of CAD.

(B) Vapor Phase Fuel Distributions

The in-cylinder vapor phase fuel distribution as a function of crank-angle degree (CAD) was quantified using the equivalence ratio (ϕ) vs. fluorescence intensity (I) relation obtained in Chap. 5 as shown below.

$$I \propto \alpha(\theta)(1-\exp[-\beta(\theta)\phi]) \qquad (55)$$

Where I is the fluorescence intensity, ϕ is the equivalence ratio, and $\alpha(\theta)$ or $\beta(\theta)$ are the fitting constant at given CAD (θ)

The quantification procedures as follow:

(a) The in-cylinder vapor phase fuel distribution as a function of crank-angle degree (CAD) was obtained in Fig. 82(a).

(b) Figure 82(a) was converted to an iso-intensity contour map.

(c) The iso-intensity contour map was then converted to an iso-equivalence ratio contour map using the Eq. (55) (with the known values of intensity (I) and those $\alpha(\theta)$ and $\beta(\theta)$ in Table 6 obtained as a function of CAD).

(d) The quantitative result of the iso-equivalence ratio contour map of vapor phase fuel distribution is shown in Fig. 83.

REFERENCES

1. T. Johnen, M. Haug, "Spray Formation Observation and Fuel Film Development Measurements in the Intake of a Spark Ignition Engine," SAE Paper 950511, 1995.
2. M. Tabata, M. Kataoka, M. Fujimoto, Y. Noh, "In-Cylinder Fuel Distribution, Flow Field, and Combustion Characteristics of a Mixture Injected SI Engine," SAE Paper 950104, 1995.
3. J. U. Kim, B. Golding, H. J. Schock, D. G. Nocera, P. Keller, "Exciplex Fluorescence Visualization Systems for Pre-Combustion Diagnosis of an Automotive Gasoline Engine," SAE Paper 960826, 1996.
4. J. U. Kim, W. K. Hartmann, H. J. Schock, B. Golding, D. G. Nocera, "The Electron Donor-Acceptor Exciplex of N,N-dimethylaniline and 1,4,6-trimethylnaphthalene," Chemical Physics Letters, 267, 323 (1997).
5. L. A. Melton, "Use of Fluorescence Methods for Measurement of Droplet and Vapor Temperatures," unpublished paper, Chemistry Dep., University of Texas-Dallas, 1993.
6. M. R. Wells, L. A. Melton, ASME Journal of Heat Transfer, 112, 1008 (1990).
7. T. R. Hanlon, L. A. Melton, "Exciplex Fluorescence Thermometry of Falling Hexadecane Droplets," ASME Journal of Heat Transfer, 114, 450 (1992).
8. J. Zhang, L. A. Melton, "Potential Systematic Errors in Droplet Temperatures Obtained by Fluorescence Methods," ASME Journal of Heat Transfer, 115, 325 (1993).
9. M. Winter, "Measurement of the temperature Field Inside a Falling Droplet," ILASS-AMERICAS, 4th annual Conference, Extended Abstracts, Hartford, CT., (1990).
10. J. Zhang, L. A. Melton, "Numerical Simulations and Restorations of Laser Droplet-Slicing Images," Appl. Opt., 33, 192 (1994).
11. T. Kadota, Y. Taniguchi, K. Kadowski, "Exciplex Method for Remote Probing of Fuel Droplet Temperature," JSME Int. J., Ser. II, 34, 242 (1991).
12. T. Kadota, K. Miyoshi, M. Tsue, "Exciplex Method for Remote Probing of Fuel Droplet Temperature. Effects of Ambient Conditions on Fluorescence," JSME Int. J., Ser. B., 36, 371 (1993).
13. G. O. Rubel, M. Seaver, "The Temperature of an Evaporating Water Droplet with a Monolayer: A comparison of Experiment and Theory," Atmos. Res., 31, 59 (1994).
14. T. Yoshizaki, T. Funahashi, K. Nishida, H. Hiroyasu, "2-D Measurements of the Liquid Phase Temperature in Fuel Sprays," SAE Paper 950461, 1995.
15. T. Q. Ni, L. A. Melton, "Temperature Impinging of Liquid Alkanes on Hot Steel Surface," unpublished data (1993).
16. K. Chihara, H. Baba, "Quenching of dual Fluorescences of Pyrene Vapor by High- Pressure Oxygen or Nitric Oxide," Chem. Phys., 25, pp. 299-306, 1977.
17. R. A. Coveleskie, D. A. Dolson, C. S. Paramenter, "A Direct View of Intramolecular Vibrational Redistribution in S1p-difluorobenzene," J. Chem. Phys., 72, pp. 5774-5, 1980.
18. S. Hirayama, D. Phillips, "Vapor-Phase Exciplex Formed between 9,10-Dicyanoanthracene and Nonamine Additives," J. Phys. Chem., 85, pp. 643-7, 1982.
19. T. J. Whitaker, B. A. Bushaw, "Laser-Induced Fluorescence Analysis of Vapor-Phase Pyrene," J. Phys. Chem., 85, pp. 2180-2, 1981.
20. F. Zhao et al., "Temporal and Cyclic Fluctuation of Fuel Vapor Concentration in a Spark Ignition Engine," SAE Paper 912346, 1991.
21. M. E. A. Bardsley et al., "2-D Visualization of Liquid and Vapor Fuel in an I.C. Engine," SAE Paper 880521, 1988.
22. F. V. Bracco, "Modeling of Engine Sprays," SAE Paper 850394, 1985.
23. S. C. Johnston, C. W. Robinson, W. S. Rorke, J. R. Smith, P. O. Witze, "Application of Laser Diagnostics to an Injected Engine," SAE Paper 790092, 1979.
24. T. M. Dyer, "New Experimental Techniques for In-cylinder Engine Studies," SAE Paper 850396, 1985.
25. W. T. Lyn, E. Valdmanis, "The Application of High Speed Photography to Diesel Engine Research," J. Photographic Science, 10, 1962.

26. J. F. Alcock, W. M. Scott, "Some More Light on Diesel Combustion," I. Mech. E. (Automobile Div.), pp. 179-191, 1962.
27. M. Parks, C. Polonski, R. Toye, "Penetration of Diesel Fuel Sprays in Gases," SAE Paper 660747, 1966.
28. R. D. Reitz, F. V. Bracco, "Ultra High Speed Filming of Atomizing Round Jets," Phys. Fluids, 22, pp. 1054-1064, 1979.
29. K. -J. Wu, C. C. Su, R. L. Steinberger, D. A. Santavicca, F. V. Bracco, "Measurement of the Spray Angle of Atomizing Jets," J. of Fluids Engineering, 105, pp. 406-413, 1983.
30. H. Hiroyasu, T. Kadota, M. Arai, "Fuel Spray Characterization in Diesel Engines," Symp. on Combustion Modeling in Reciprocating Engines, General Motors, Detroit, MI, 1978.
31. T. Shiozaki, T. Suzuki, M. Shimoda, "Observation of Combustion Process in D.I. Engines via High Speed Direct and Schlieren Photography," SAE Paper 800025, Diesel Combustion and Emissions, Proc-eedings, P-86, 1980.
32. M. M. Elkotb, A. M. Iskander, "Fuel Spray Modeling for Swirl Chamber Diesel Engines," Paper IB/2, ICLASS-85, Imperial College, London, U.K., July 1985.
33. M. J. Tindal, T. J. Williams, A. T. Harcombe, "Fuel Spray Formation in an Experimental Swirl Chamber," SAE Paper 870451, 1987.
34. P. Werlberger, W. P. Cartellieri, "Fuel Injection and Combustion Phenomena in a High Speed D.I. Diesel Engine Observed by Means of Endoscopic High Speed Photography," SAE Paper 870097, 1987.
35. K. -J. Wu, A. Coghe, D. A. Santavicca, F. V. Bracco, "LDV Measurements of Drop Velocity in Diesel-type Sprays," AIAA J., 22, 1263-1270, 1984.
36. K. Wandres, H. Weigand, J. Muller, H. Steinbichler, "High Speed Photography and Pulsed Laser Holography for Diagnostic Investigation of Mixture Formations and Vibration in Reciprocating Engines," International Conference on Combustion in Engineering, 1, I. Mech., paper C79/83, 1983.
37. A. O. zur Loye, D. A. Santavicca, F. V. Bracco, "Preliminary Study of Flame Structure in an IC Engine Using 2-D Flow Visualization," Intnl. Symp. on Diagnostics and Modeling of Combustion in Reciprocating Engines (COMODIA 85), Tokyo, Japan, 1985.
38. T. A. Baritaud, R. M. Green, "A 2-D Flame Visualization Technique Applied to the I.C. Engine," SAE Paper 860025, 1986.
39. A. O. zur Loye, F. V. Bracco, "Two Dimensional Visualization of Premixed-Charge Flame Structure in a I.C. Engine," SAE Paper 870454, 1987.
40. P. G. Felton, J. Mantzaras, M. E. A. Bardsley, F. V. Bracco, "2-D Visualization of Liquid Fuel Injection in an Internal Combustion Engine," SAE Paper 872074, 1987.
41. G. M. Brown, J. C. Kent, "Fluorescent Light Section Technique for Fuel Spray Characterization," 'Flow Visualization III', Yang, W.J. (ed.), Proceedings of the Third International Symposium on Flow Visualization, 1983.
42. X. Li, R. S. Tankin, "A study of Cold and Combustion Flow Around Bluff Body Combustors," Combustion Science and Technology, 52, pp. 173-206, 1987.
43. S. C. Johnston, "An Experimental Investigation Into the Application of Spontaneous Raman Scattering to Spray Measurements in an Engine," Proc. ASME, Fluids Engineering Conf., Boulder, CO., ASME, NY, pp. 10077-118, June 1981.
44. S. C. Johnston, "Precombustion Fuel/Air Distribution in a Stratified-Charge Engine Using Laser Raman Spectroscopy," SAE Paper 790433, 1979.
45. A. R. Chraplyvy, "Nonintrusive Measurements of Vapor Concentrations Inside Sprays," Appl. Optics, 20, pp. 2620-4, 1981.
46. J. M. Tishkoff, D. C. Jr. Hammond, A. R. Chraplyvy, "Diagnostic Measurements of Fuel Spray Dispersions," J. of Fluids Eng., pp. 313-7, 1982.
47. D. A. Hansen, E.K.C. Lee, "Radiative and Nonradiative Transitions in the First Excited Singlet State of Simple Linear Aldehydes," J. Chem. Phys. 63, 3272, 1975.
48. F. Beretta, V. Cincotti, A. D'Alessio, P. Menna, "Ultraviolet and Visible Fluorescence in the Fuel Pyrolsis Regions of Gaseous Diffusion Flames," Combust. Flame 61, 211, 1985.
49. A. Lozano, B. Yip, R.K. Hanson, "Acetone: a tracer for concentration measurements in gaseous flows by planar laser-induced fluorescence," Experiments in Fluids 13, 369, 1992.

50. P. H. Paul, I. Van Cruyningen, R.K. Hanson, G. Kychakoff, "High Resolution Digital Flow field Imaging of Jets," Experiments in Fluids 9, 241, 1990.
51. P. Andresen, G. Meier, H. Schluter, H. Voges, A. Koch, W. Hentschel, W. Opperman, E. Rothe, "Fluorescence Imaging Inside an Internal Combustion Engine Using Tunable Excimer Laser," Applied Optics 29, 2392, 1990.
52. A. Arnold, H. Becker, R. Suntz, P. Monkhouse, J. Wolfrum, R. Maly, W. Pfister, "Flame front imaging in an internal-combustion engine by laser-induced fluorescence of acetaldehyde," Optics Letters 15, 831, 1990.
53. W. Lawrenz, J. Kohler, F. Meier, W. Stolz, R. Wirth, W.H. Bloss, R.R. Maly, E. Wagner, M. Zahn, "Quantitative 2D LIF Measurements of Air/Fuel Ratios During the Intake Stroke in a Transparent SI Engine," SAE Paper 922320, 1992.
54. T.A. Baritaud, T.A. Heinze, "Gasoline Distribution Measurements with PLIF in a SI Engine," SAE Paper 922355, 1992.
55. A. Arnold, A. Buschmann, B. Cousyn, M. Decker, F. Vannobel, V. Sick, J. Wolfrum, "Simultaneous Imaging of Fuel and Hydroxyl Radicals in an In-line Four-Cylinder SI Engine," SAE Paper 932696, 1993.
56. H. Neij, B. Johansson, M. Alden, "Development and Demonstration of 2D-LIF for Studies of Mixture Preparation in SI Engines," Combust. Flame 99, 449, 1994.
57. J. Reboux, D. Puechberty, F. Dionnet, "A New Approach of Planar Laser Induced Fluorescence Applied to Fuel/Air Ratio Measurement in the Compression Stroke of an Optical S.I. Engine," SAE Paper 941988, 1994.
58. E. Winklhofer, H. Phillipp, G. Fraidl, H. Fuchs, "Fuel and Flame Imaging in SI Engine," SAE Paper 930871, 1993.
59. L. A. Melton, "Spectrally Separated Fluorescence Emissions for Diesel Fuel Droplets and Vapor," Appl. Optics, 22, pp. 2224-6, 1983.
60. L. A. Melton, J. F. Verdieck, "Vapor/Liquid Visualization in Fuel Sprays," Twentieth Symp. (International) on Combustion, The Combustion Institute, pp. 1283-1290, 1984.
61. L. A. Melton, J. F. Verdieck, "Vapor/Liquid Visualization for Fuel Sprays," Combust. Sci. and Tech., 42, pp. 217-222, 1985.
62. A. A. Rotunno, L. A. Melton et al., "Direct Calibration procedures for Exciplex-based Vapor/Liquid Visualization of Fuel Spray," Combust. Sci. and Tech., 71, 247, 1990.
63. M. E. A. Bardsley, P. G. Felton, F. V. Bracco, "2-D Visualization of a Hollow-Cone Spray in a Cup-in-Head, Ported, I.C. Engine," SAE Paper 890315, 1989.
64. P. G. Felton, F. V. Bracco, M. E. A. Bardsley, "On the Quantitative Application of Exciplex Fluorescence to Engine Sprays," SAE Paper 930870, 1993.
65. L. A. Melton, "Quantitative Use of Exciplex-based Vapor/Liquid Visualization Systems (A Users Manual)," Final Report, Army Research Office Contract DAAL03-86-K-0082, 1988, (NTIS order # ADA191649).
66. I. B. Berlman, "Fluorescence Spectra of Aromatic Molecules," 2nd edition, Academic Press, New York, 1971.
67. L. A. Melton, "Exciplex-Based Vapor/Liquid Visualization Systems Appropriate for Automotive Gasolines (A Users Manual)," Final Report, Texas Higher Education Coordinating Board Energy Research Applications Program, Contract #27, 1993.
68. R. Shimizu et al., "Measurement of Air-Fuel Mixture Distribution in a Gasoline Engine Using LIEF Technique," SAE Paper 922356, 1992.
69. D. H. Shack, W. C. Reynolds, "Application of Particle Tracking Velocimetry to the Cyclic Variability of the Pre-Combustion Flow Field in a Motored Axisymmetric Engine," SAE Paper 910475, 1991.
70. D. L. Reuss, R. J. Adrian, C. C. Landreth, D. T. French, T. D. Fansler, "Instantaneous Planar Measurements of Velocity and Large-Scale Vorticity and Strain Rate in an Engine Using Particle Image Velocimetry," SAE Paper 890618, 1989.
71. "Molecular Tagging Velocimetry (MTV)," in the www site, 1997.
72. M.M. Koochesfahani, D.G. Nocera, "Molecular Tagging Velocimetry: A review of Techniques, Chemical Concepts, and Application," Experiment in Fluids, 1997, invited paper.

73. M.M. Koochesfahani, R.K. Cohn, C.P. Gendrich, D.G. Nocera, "Molecular Tagging Diagnostics for the Study of Kinematics and Mixing in Liquid Phase Flows," Developments in Laser Techniques in Fluid Mechanics, Springer-Verlag: Berlin, 1997, in press.

74. R.E. Falco, D.G. Nocera, "Quantitative Multipoint Measurement and Visualization of Dense Solid-Liquid Flows by Using Laser Induced Photochemical Anemometry (LIPA)," Butterworth-Heinemann: Boston, 1992; Chapter 3, p 59.

75. C.P. Gendrich, M.M. Koochesfahani, D.G. Nocera, "Molecular Tagging Velocimetry and other Novel Applications of a New Phosphorescent Supramolecules," Experiment in Fluids, 1997, in press.

76. C.P. Gendrich, M.M. Koochesfahani, D.G. Nocera, "Analysis of Molecular Tagging Velocimetry Images for Obtaining Simultaneous Multipoint Velocity Vectors," Bull. Am. Phys. Soc. 1994, 39, 1980.

77. B. Stier, M.M. Koochesfahani, D.G. Nocera, H.J. Schock, "Molecular Tagging Velocimetry in Gas Phase Flow," Bull. Am. Phys. Soc. 1995, 40, 2000.

78. B. Stier, M.M. Koochesfahani, D.G. Nocera, H.J. Schock, "Velocity Measurements in a Steady Flow Model of an IC Model using Molecular Tagging Velocimetry," Bull. Am. Phys. Soc. 1997, 41, 1804.

79. Robert A. Alberty., "Physical Chemistry," 6th edition, John Wiley & Sons, pp. 695-696, 1983.

80. Lakowicz, J.R., "Principles of Fluorescence Spectroscopy," Plenum: New York, 1983; Chapter 9.

81. W. M. Vaughan, G. Weber, Biochem. 9, p464-473, 1970.

82 C. N. Banwell, "Fundamentals of Molecular Spectroscopy," Berkshire, England: McGraw-Hill., 1966.

83 R. J. Cattolica, S. R. Vosen, "Two-Dimensional Measurements of the [OH] in a Constant Volume Combustion Chamber," Twentieth Symposium (International) on Combustion. Pittsburgh: The Combustion Institute, pp. 1273-1282, 1984.

84 K. P. Gross, R. L. McKenzie, P. Logan, "Measurements of Temperature, Density, Pressure, and Their Fluctuations in Supersonic Turbulence Using Laser Induced Fluorescence," Exp. Fluids, Volume 5, pp. 372-380, 1987.

85 B. E. Battles, J. M. Seitzman, R. K. Hanson, "Quantitative Planar Laser-Induced Fluorescence Imaging of Radical Species in High Pressure Flames," AIAA Paper 94-0229, 32nd Aerospace Sciences Meeting, Reno, NV., 1994.

86 Kobayashi et al., "Application of UV and VUV Excimer Lasers in Combustion Measurements Using Enhanced Raman Scattering," Laser Diagnostics and Modeling of Combustion, Stringer-Verlag, pp. 133-140, 1987.

87 Katharina Kohse-Ho inghaus, "Quantitative Laser-Induced Fluorescence: Some Recent Developments in Combustion Diagnostics," Appl. Phys. B 50, 455-461, 1990.

88 P. Andresen, A. Bath, W. Gröger et al., "Laser-Induced Fluorescence with tunable excimer lasers as a possible method for instantaneous temperature field measurements at high pressure: Checks with an atmospheric flame," Applied Optics, Vol. 27, No. 2, 1988.

89 P. Andresen, Gerard Meijer, Harald Schlüter et al., "Fluorescence Imaging Inside an Internal Combustion Engine Using Tunable Excimer Lasers," Applied Optics, Vol. 29, No. 16, 1990.

90 A.C. Eckbreth., "Laser Diagnostics for Combustion Temperature and Species," Abacus Press, Tunbridge Wells, UK, 1988.

91 R.K. Hanson., "Twenty-First Intl's Symposium on Combustion," The Combustion Institute, pp. 1677, 1986.

92. C. K. Law, "Recent advances in droplet vaporization and combustion," Prog. Energy Combust. Sci. 8, 171, 1982.

93. W. A. Sirignano, "Fuel droplet vaporization and spray combustion theory," Prog. Energy Combust. Sci. 9, 291, 1983.

94. G. M. Faeth, "Evaporation and combustion of sprays," Prog. Energy Combust. Sci. 9, 1, 1983.

95. G. J. Bastiaans, G. M. Hieftje, "Investigation into the Vaporization of Individual Solute Particles in Flame Spectrometry," Analytical Chemistry, Vol. 46, No. 7, 901, 1974.

96. C. Th. J. Alkemade, "Flame Emission and Atomic Absorption Spectrometry, Vol. I-Theory," J. A. Dean, T. C. Rains, Ed., Marcel Dekker, New York, N. Y., p 101, 1969.

97. F. A. Williams, "Combustion Theory," Addison-Wesley, Reading, MA., 1965.

98. R. B. Bird, W. E. Stewart, E. M. Lightfoot, "Transport Phenomena," Part III. John Wiley, New York, 1960.

99. L. Lee, "Third Combustion and Propulsion Colloquium," AGARD, Pergamon Press, New York, p 451-497, 1958.

100.F. T. Garner, Trans. Instr. Chem. Engr. Lond. 28, 88-96, 1950.

101.E. L. Wakil, M. M. Priem, R. J. Brikowski, H. J. Meyers, O. A. Uyehara, "Experimental and calculated temperature and mass histories of vaporizing fuel drop," NACA TN 3490, Washington, DC. 1956.

102.G. M. Faeth, "Combustion characteristics of blended monopropellant droplets," AIAA Paper 70-77, 1970.

103.G. M. Faeth, R. S. Lazar, AIAA J. 9, 2165-2171, 1971.

104 J.N. Demas., "Excited State Lifetime Measurement," Academic Press, pp. 62, 1983.

105 A.M. Murray, L.A. Melton, "Fluorescence Methods for Determination of Temperature in Fuel Sprays," Applied Optics, Vol. 24, No. 17, pp. 2783-2786, 1985.

106 M. Gordon, W.R. Ware., "The Exciplex," pp. 1-21, Academic Press, New York, 1975.

107.S.J. Hale, L.A. Melton., "Absolute Quantum Yields for Exciplex Fluorescence," Appl. Spectr., 44, 101, 1990.

108.L. A. Melton, "Exciplex-Based Vapor/Liquid Visualization Systems Appropriate for Automotive Gasolines," Appl. Spect., 47, 782, 1993.

109."Handbook of Data on Organic Compounds," 3rd edition, Boca Raton, Fl: CRC press, c1994.

110.Y. -g. K. Shin, V. M. Miskowski, D .G. Nocera, Inorg. Chem., 29, 2308, 1990.

111.N. J. Turro, Modern molecular photochemistry (Benjamin Cummings), Menlo Park, CA, 1978.

112.S. L. Murov, I. Carmichael, G. L. Hug, eds. Handbook of photochemistry (Marcel Dekker, New York, 1993) p. 176.

113.V. Balzani, L. Moggi, M. F. Manfrin, F. Bolletta, Coord. Chem. Rev., 15, 321, 1975.

114.S. L. Murov, I. Carmichael, G. L. Hug, Handbook of photochemistry, 2nd edition, Marcel Dekker, New York, 1993, Ch.1.

115.L. E. Bowman, K. A. Berglund, D. G. Nocera, Rev. Sci. Instrum. 64 (1993) 338.

116.P. A. Martic, R. C. Daly, J. L. R. Williams, S. Farid, "Effect of Polymeric Matrices and Temperatures on Exciplex Formation," Polymer Sci. (Polymer Lett.) 15, 295 (1977).

117.A. Weller, Z. Phys. Chem. 133 (1982) 93.

118.B. Stevens, Adv. Photochem. 8 (1971) 161.

119.N. Helsen, L. Viaene, M. Van Der Auweraer, F. C. Deschryver, J. Phys. Chem. 98 (1994) 1532.

120.G. S. Bahn, "Role of Vaporization Rate in Combustion of Liquid Fuels," p. 104, in the Literature of The Combustion of Petroleum ACS, American Chemical Society, 1958.

121.W. D. Bachalo, M. J. Houser, "Phase Doppler Spray Analyzer for Simultaneous Measurements of Drop Size and Velocity Distributions," Opt. Eng., 23, 583 (1984).

122.P. Massoli, F. Beretta, A. D'Alessio, M. Lazzaro, "Temperature and Size of Single Transparent Droplets by Light Scattering the Forward and Rainbow Regions," Appl. Opt. 32, 3295 (1993).

123.Zhang, "Fluorescence Methods for Determination of Temperature in Aerosol Particles," Ph.D dissertation, Mech. Eng. Dept., University of Nebraska-Lincoln, 1991.

124.J. H. Stufflebeam , "Exciplex Fluorescence Thermometry of Liquid Fuel," Appl. Spectrosc., 43. 274 (1989).

125.O. Arce, "Temperature and Size Measurements of Free Falling Decane Droplets," M. S. thesis, University of Texas at Dallas. (1993)

126.K. F. Schrum, A. F. Williams, S. A. Haether, D. Amotz, "Molecular Fluorescence Thermometry," Anal. Chem., 66, 2788, (1994).

127."Manuals," Princeton Instrument, Inc. 1991.

128."User's manual," CSMA software version 2.4., Princeton Instruments, Inc. 1994.

129.V. Wylen, R. Sonntag, C. Borgnakke, "Fundamentals of Classical Thermodynamics" 4th ed., pp 49, 1993.

130.R. C. Weast, "CRC Handbook of Chemistry and Physics", 64th ed., CRC press, 1983.

131.M. E. A. Bardsley, "Two Dimensional Visualization of Fuel Sprays in an Internal Combustion Engine," M. S. Thesis, Mech. Eng. Dept, Princeton University, 1990.

132."Catalog Handbook of Fine Chemical," Aldrich Chemical Company, Inc. 1994-1995.

133.J.D. Ingle, S.R. Crouch, "Spectrochemical Analysis," Prentice-Hall, Englewood Cliffs, New Jersey, 1988.

134.T. D. Fansler, D. T. French, M. C. Drake, "Fuel Distributions in a Firing Direct-Injection Spark-Ignition Engine Using Laser-Induced Fluorescence Imaging," SAE Paper 950110, 1995.

135.Private discussion with T. D. Fansler and D. T. French

136.R. M. Frank, J. B. Heywood, "The Importance of Injection System Characteristics on Hydrocarbon Emissions from a Direct-Injection Stratified-Charge Engine," SAE Paper 900609, 1990.

137.N. Miyamoto, H. Ogawa, T. Shudo, F. Takeyama, "Combustion and Emissions in a New Concept DI Stratified Charge Engine with Two-Stage Fuel Injection," SAE Paper 940675, 1994.

138.P. H. Campbell, K. M. Sinko, B. Chehroudi, "Liquid and Vapor Phase Distributions in a Piloted Diesel Fuel Spray," SAE Paper 950445, 1995.